

INFORMATION TO USERS

This manuscript has been reproduced from the microfilm master. UMI films the text directly from the original or copy submitted. Thus, some thesis and dissertation copies are in typewriter face, while others may be from any type of computer printer.

The quality of this reproduction is dependent upon the quality of the copy submitted. Broken or indistinct print, colored or poor quality illustrations and photographs, print bleedthrough, substandard margins, and improper alignment can adversely affect reproduction.

In the unlikely event that the author did not send UMI a complete manuscript and there are missing pages, these will be noted. Also, if unauthorized copyright material had to be removed, a note will indicate the deletion.

Oversize materials (e.g., maps, drawings, charts) are reproduced by sectioning the original, beginning at the upper left-hand corner and continuing from left to right in equal sections with small overlaps. Each original is also photographed in one exposure and is included in reduced form at the back of the book.

Photographs included in the original manuscript have been reproduced xerographically in this copy. Higher quality 6" x 9" black and white photographic prints are available for any photographs or illustrations appearing in this copy for an additional charge. Contact UMI directly to order.

U·M·I

University Microfilms International
A Bell & Howell Information Company
300 North Zeeb Road, Ann Arbor, MI 48106-1346 USA
313/761-4700 800/521-0600

Order Number 9416070

**Measuring aerosol optical depths from satellite: Aerosol
measurements and models**

Porter, John Nolan, Ph.D.

University of Hawaii, 1993

U·M·I
300 N. Zeeb Rd.
Ann Arbor, MI 48106

MEASURING AEROSOL OPTICAL DEPTHS FROM SATELLITE:
AEROSOL MEASUREMENTS AND MODELS

A DISSERTATION SUBMITTED TO THE GRADUATE DIVISION OF THE
UNIVERSITY OF HAWAII IN PARTIAL FULFILLMENT OF THE
REQUIREMENTS FOR THE DEGREE OF

DOCTOR OF PHILOSOPHY

IN

METEOROLOGY

DECEMBER 1993

By

John Nolan Porter

Dissertation Committee:

Antony Clarke, Chairman
Pierre Flament
Anders Daniels
Thomas Schroeder
Barry Huebert

ACKNOWLEDGEMENTS

I would like to acknowledge several people whose help has been instrumental in the completion of this dissertation. Dr. Antony D. Clarke has been my advisor during both my Masters and PhD research. He has always been generous with his time to discuss (or even argue) any matter. Being associated with him has allowed me to participate in numerous experiments. Many of the measurements taken during those experiments appear in this dissertation. Dr. Pierre Flament collected AVHRR images of the Hawaiian island region and made them available for public use. Without access to these images as well as their display software, this dissertation would have been substantially more difficult to carry out. I would like to thank Dr. Anders Daniels, Dr. Thomas Schroeder and Dr. Barry Huebert for their time and effort in both reading and discussing this dissertation. I would also like to thank Dr. Terujuki Nakajima for the use of his discrete ordinates model and Dr. Phill Durkee and Craig Motell for valuable comments. Finally I would like to thank my wife Fee for her patience and support during this long process.

ABSTRACT

One of the primary uncertainties in measuring aerosol optical depths from satellite is in the choice of the aerosol phase function. Various investigators have suggested the ratio of AVHRR channels 1 and 2 could be used to derive a variable phase function suitable for many different aerosol cases. In order to investigate this possibility, a new aerosol model was developed from a large data set of in-situ aerosol size distribution measurements and used to model the satellite response. The model results suggest the ratio of AVHRR channels 1 to 2 can be used to roughly derive the aerosol phase function value. In order to test the modeling results, aerosol optical depths were obtained from satellite images and were compared with ground based sun photometer measurements. Both methods were in reasonable agreement for this study although clouds made exact comparisons difficult.

Error analysis of the aerosol optical depth derived from AVHRR satellites was also performed. The error was found to be dependent on the scattering angle with largest errors occurring near 120 degrees corresponding to the minimum in the aerosol phase function. Sources of error studied here include sun glint, sensor noise, sensor calibration, water vapor absorption for channel 2 and ozone absorption for channel 1. For the scattering angles with the largest errors, near 120 degrees, the one standard deviation errors in the aerosol

optical depth were approximately ± 0.03 . Either spatial or temporal averaging can reduce the sensor noise resulting in one standard deviation errors of ± 0.02 . Similar errors exist for channel 2. Errors in the AVHRR ch1/ch2 ratio range from 75%, 35%, 18% and 12% for respective aerosol optical depths of 0.05, 0.1, 0.2, 0.3. Spatial or temporal averaging can reduce this error to 13%, 6%, 4% and 3% for similar optical depths. In addition, the systematic error caused by the AVHRR's coarse digitization was studied and an example of its effect is given as well as a possible way to minimize this problem.

TABLE OF CONTENTS

ACKNOWLEDGEMENTS	iii
ABSTRACT	iv
LIST OF TABLES	viii
LIST OF FIGURES	ix
CHAPTER 1 INTRODUCTION	1
CHAPTER 2 RADIATIVE THEORY AND SATELLITE MODEL	9
SATELLITE RADIATIVE TRANSFER EQUATION	9
WATER LEAVING RADIANCE	12
MOLECULAR SCATTER AND ABSORPTION	18
AEROSOL SCATTER	20
CHAPTER 3 AEROSOL MODEL	25
INSTRUMENTATION	26
ACCUMULATION MODE MARINE AEROSOL	27
COARSE MODE MARINE AEROSOL	31
CHAPTER 4 SATELLITE RESPONSE AEROSOL CASES	35
SINGLE SCATTER VERSUS MULTIPLE SCATTER	35
AVHRR CHANNEL CH1/CH2 RATIO	41
AEROSOL LAYERS	44
CHAPTER 5 SATELLITE AND INSITU COMPARISONS	49
HAWAIIAN AVHRR IMAGE: MARCH 27, 1993	49
COMPARISON OF GROUND AND SATELLITE MEASUREMENTS	54
CHAPTER 6 ERROR ANALYSIS	58
SENSOR PRECISION EFFECTS	58
ERROR ANALYSIS OF VARIOUS TERMS INFLUENCING SATELLITE DERIVED OPTICAL DEPTH	61
CHAPTER 7 CONCLUSION	72

REFERENCES 120

LIST OF TABLES

Table		page
1	Aerosol parameters for the lognormal curves used to model the dry sulfate accumulation mode number distribution. Shown in the first column is the aerosol case and the number of measured aerosol distributions used in developing the model for that aerosol volume range. Each measured aerosol distribution was averaged over a time period ranging from 15 minutes up to 3 hours.	76
2	Same as table 1 for the coarse mode salt aerosol.	77

LIST OF FIGURES

Figure	page
1.1. Examples of two aerosol phase functions as well as the molecular phase function. For the marine aerosol case the distribution had salt and sulfate concentrations of 3.13 and 0.55 $\mu\text{g}/\text{m}^3$ and the distribution was shifted to larger diameters by a factor of 1.9 and 1.6 to account for the uptake of water at high relative humidities. The free troposphere/stratosphere case had a concentration of 0.55 $\mu\text{g}/\text{m}^3$ and was shifted to larger diameters by a factor of 1.15 to account for the uptake of water at lower relative humidities.	78
1.2. Aerosol distributions measured with a laser optical counter in various regions of the remote marine atmosphere. These cases illustrate the range of variability (note the scale changes). Also shown are several log normal fits to the measured size distributions.	79
1.3. Wavelength response for the various channels of the AVHRR satellite. The channels used in the present study include, channel 1 in the visible, channel 2 in the near IR and channels 4 and 5 in the IR.	80
2.1. Shown here are various forms of scattering including aerosol and Rayleigh single scattering, scattering from the ocean surface (either glint or foam), sea light and various types of multiple scattering. The notation used in the text for the aerosol scattering angle is also shown here.	81
2.2. Ocean surface scattering geometry. Shown here is the face of a wavelet which is tilted with respect to the zenith.	82
2.3. Fresnel reflection coefficients for various scattering angles. In this figure the scattering angle is taken from the incident light to the scattered light. This is different from the aerosol scattering angle (shown in figure 2.1) where the scattering angle is taken from the forward direction to the scattered light.	83

2.4.	Fractional ocean whitecap coverage based on O'Muircheartaigh and Monahan (1986) and Koepke (1985). The O'Muircheartaigh and Monahan values are presented with the prefix M. The C and S refer to two different data sets and the numbers 1, 2 and 3 refer to different statistical methods applied to the data sets. For the present study the M1-C case was employed.	84
2.5.	Ocean surface scattering coefficient as a function of θ_n where θ_n is the angle from the zenith to the direction normal to the face of ocean surface wave which is tilted so that it produced sun glint for the satellite (see figure 2.2.). At larger θ_n angles the glint term drops off and the ocean reflection becomes isotropic and depends only on whitecap coverage assumed.	85
2.6.	AVHRR channel 2 water vapor absorption optical depth as a function of total atmospheric water vapor. Values are based on the work of Sanders and Edwards (1989) with Lowtrans7 model.	86
2.7.	Example of: aerosol volume distribution (top panel), aerosol number distribution (next panel), aerosol scattering coefficient (next panel) and differential scattering coefficient (bottom panel). Calculations were done for a wavelength of 0.63 μm	87
3.1.	Map showing the location of various aerosol measurement experiments. Ship experiments are shown as lines. Aircraft experiments are shown as circles.	88
3.2.	Equilibrium aerosol diameters as a function of relative humidity for various aerosol compositions. The values for NaCl, H ₂ SO ₄ and (NH ₄)SO ₄ are based on the work of Tang et al. The line shown for the mixture is based on laboratory experiments with various molar ratios of (NH ₄)/(SO ₄) ranging from 0 to 1. Aerosol volatility tests performed during the various experiments suggest remote marine aerosol molar ratios are typically in this range.	89

3.3a.	Average dry aerosol size distributions measured with the differential mobility analyzer during the SAGA3 ship experiment. These various cases came from grouping each aerosol distribution according to its dry aerosol volume (ie. mass) and then averaging each group of distributions. The aerosol group is shown next to each distribution.	90
3.3b.	Average dry aerosol size distributions measured during the Kaiyoumaru ship experiment. The method of grouping and averaging each measured aerosol size distribution is similar to figure 3.3a.	90
3.4a.	Average dry aerosol size distributions measured during the Astex experiment. The method of grouping and averaging is the same as was used in figures 3.3a and 3.3b.	91
3.4b.	Same dry aerosol averages as shown in figure 3.4a but now shown as the aerosol area distributions.	91
3.5.	The dry sulfate aerosol model developed from insitu aerosol measurements. The top panel displays average 1 through 6. The bottom panel displays average 4 through 9. The lognormal parameters for these curves are given in table 1..	92
3.6.	The estimated aerosol transmission losses in the sampling system. The aircraft losses (ELECTRA) are shown for low and high relative humidity cases such as is found above and below the trade wind inversion. Also shown are the transmission losses for the SAGA 2&3 ship experiment.	93
3.7.	Salt aerosol comparison for the optical particle counter and the Woodcock glass slide impactor. The Woodcock measurements range from approximately 0.9 to 20.0 μm while the OPC measurements range from 0.17 to 7.5 μm diameter. Also shown is a curve fit for the OPC distribution at the smaller sizes and the impactor distribution at the larger sizes.	94
3.8.	The dry salt aerosol model developed from the combination of OPC and Woodcock distributions. The curves in the upper figure correspond to wind beaufort scales of 1 to 6 while the bottom figure curves correspond to scales of 7 to 12.	95

4.1.	A comparison between aerosol single scatter (solid boxes), aerosol linearized single scatter (line) and aerosol multiple scatter (crosses) plotted versus the aerosol linearized single scatter value. Calculations are for a large range of satellite and sun geometries and aerosol optical depths ranging from 0.03 to 0.8. .	96
4.2.	The linear single scatter from figure 4.1 plotted versus the aerosol optical depth. This figure allows for the interpretation of figure 4.1 in terms of aerosol optical depth. ...	96
4.3.	The aerosol phase functions calculated for the AVHRR satellite channel 1 from 338 different aerosol distributions. The aerosol cases were developed from various combinations of the accumulation and coarse mode and different relative humidity combinations. The phase functions were weighted for the satellite wavelength response at 5 nm intervals.	97
4.4.	The error in equation 24, as compared to equation 23, for the 338 aerosol cases and some 700 different satellite and sun viewing geometries. Shown in the left panel is the error for AVHRR channel 1 and in right panel is the error for channel 2.	98
4.5.	Calculated channel ch1/ch2 ratio plotted versus the channel 1 phase function value for scattering angles of 40 and 60 degrees. The various points correspond to 338 different aerosol cases. The line is from a third order fit.	99
4.6.	Calculated channel ch1/ch2 ratio plotted versus the channel 1 phase function value for scattering angles of 80 and 100 degrees.	100
4.7.	Calculated channel ch1/ch2 ratio plotted versus the channel 1 phase function value for scattering angles of 120 and 140 degrees. ...	101
4.8.	Calculated channel ch1/ch2 ratio plotted versus the channel 1 phase function value for scattering angles of 160 and 180 degrees. ...	102
4.9.	The error in the weighted average of two ratios plotted versus the magnitude of the ratio difference.	103

5.1.	An AVHRR (channel 1, 0.63 μm) image of the Hawaiian islands collected on March 26, 1993. In this image the color enhancement has been set so that the brighter clouds are colored and the less bright clouds are white.	104
5.2.	The processed aerosol optical depth from the AVHRR image shown in figure 5.1. In addition a color histogram is provided to determine the value of each color.	105
5.3.	The aerosol ratio for figure 5.1 and a histogram to determine the color values.	106
5.4.	The column water vapor (kg/m^2) for figure 5.1 and the color histogram.	107
5.5.	Langley plots of optical depth collected at Bellows Beach, Oahu on April 26, 1992 during the morning. The top panel is the original measurements and includes several cloudy periods. The bottom panel is the same data after cloudy periods were removed. The slope of the line is the total optical depth (ie. aerosol and molecular).	108
5.6.	Aerosol optical depths derived from: 1) sun photometer measurements at a surface site on the island of Oahu (Bellows beach), 2) sun photometer measurements taken at NOAA Mauna Loa observatory on the island of Hawaii and 3) satellite derived aerosol optical depths. The surface optical depths were obtained by the Langley plot method for daytime AM and PM measurements from a shadowband radiometer (550 nm). The satellite optical depths were taken from cloud free pixels found in a 200 by 200 km box around the island of Oahu (630 nm). The Mauna Loa optical depths were provided by Dutton Elsworth and were taken with a sun tracking sun photometer (500 nm).	109
6.1a.	An example to show how subtracting high resolution data (left panel) from coarse resolution data (middle panel) can produce striped results (right panel).	110
6.1b.	This is the same image of aerosol optical depth as figure 5.6 except a different color enhancement has been used. The striped feature shown in figure 6.1a is evident here.	110

- 6.2. The range of scattering angles over which the satellite image must be averaged is shown here for each scattering angle. Averaging the satellite radiance over this range of scattering angles serves to smooth out the digitized nature of the AVHRR image and avoid stripes in the derived aerosol optical depth. Going from left to right and top to bottom each panel corresponds to optical depths of 0.03, 0.06, 0.1 and 0.2. Going from the top curve to the bottom curve, each curve corresponds to the cosine of the satellite zenith angle with values of 1, 0.94, 0.87, 0.77, 0.5 and 0.34. 111
- 6.3. Percentage error for AVHRR channel 1 plotted as a function of the aerosol scattering angle. For this figure one standard deviation errors were used for the sensor drift, sensor noise, ozone error, water vapor error, Rayleigh error and sun glint error. Going from left to right and top to bottom, each panel correspond to aerosol optical depths of 0.05, 0.1, 0.2 and 0.3. 112
- 6.4. Percentage error for AVHRR channel 1 plotted as a function of the aerosol scattering angle. For this figure the sensor noise error was set to zero and one standard deviation errors were used for the sensor drift, ozone error, water vapor error, Rayleigh error and sun glint error. Going from left to right and top to bottom, each panel correspond to aerosol optical depths of 0.05, 0.1, 0.2 and 0.3. 113
- 6.5. Percentage error for AVHRR channel 1 plotted as a function of the aerosol scattering angle. For this figure all errors were set to zero with the exception of the sensor drift error which was set to one standard deviation value. The top through bottom curves correspond to aerosol optical depths of 0.05, 0.1, 0.2 and 0.3. 114
- 6.6. Percentage error for AVHRR channel 2 plotted as a function of the aerosol scattering angle. For this figure one standard deviation errors were used for the sensor drift, sensor noise, ozone error, water vapor error, Rayleigh error and sun glint error. Going from left to right and top to bottom, each panel correspond to aerosol optical depths of 0.05, 0.1, 0.2 and 0.3. 115

- 6.7. Percentage error for AVHRR channel 2 plotted as a function of the aerosol scattering angle. For this figure the sensor noise error was set to zero and one standard deviation errors were used for the sensor drift, ozone error, water vapor error, Rayleigh error and sun glint error. Going from left to right and top to bottom, each panel correspond to aerosol optical depths of 0.05, 0.1, 0.2 and 0.3. 116
- 6.8. Percentage error for AVHRR channel 2 plotted as a function of the aerosol scattering angle. For this figure all errors were set to zero with the exception of the sensor drift error which was set to one standard deviation value. The top through bottom curves correspond to aerosol optical depths of 0.05, 0.1, 0.2 and 0.3. 117
- 6.9. Percentage error for AVHRR channel ch1/ch2 ratio plotted as a function of the aerosol scattering angle. For this figure one standard deviation errors were used for the sensor drift, sensor noise, ozone error, water vapor error, Rayleigh error and sun glint error. Going from left to right and top to bottom, each panel correspond to aerosol optical depths of 0.05, 0.1, 0.2 and 0.3. 118
- 6.10. Percentage error for AVHRR channel ch1/ch2 ratio plotted as a function of the aerosol scattering angle. For this figure the sensor noise error was set to zero and one standard deviation errors were used for the sensor drift, ozone error, water vapor error, Rayleigh error and sun glint error. The top through bottom curves correspond to aerosol optical depths of 0.05, 0.1, 0.2 and 0.3. 119
- 6.11. Percentage error for AVHRR channel ch1/ch2 ratio plotted as a function of the aerosol scattering angle. For this figure all errors were set to zero with the exception of the sensor drift error which was set to one standard deviation value. The top through bottom curves correspond to aerosol optical depths of 0.05, 0.1, 0.2 and 0.3. 119

CHAPTER ONE

INTRODUCTION

Atmospheric aerosol play a central role in a variety of climatic processes through their ability to directly and indirectly modify the earth's radiative balance. Their direct influence on the earth's radiative balance comes from their ability to scatter solar radiation back out to space thereby increasing the planetary albedo. Their indirect effect comes from their ability to modify cloud properties which are the dominant source of planetary albedo.

Estimations of the direct effect have been calculated by Charlson et. al. (1991) who suggest that backscatter of solar radiation by aerosol increase the planetary albedo by an amount which is equal to 32 times the aerosol optical depth. This is equivalent to saying that approximately 2.4% of the light scattered by aerosol is scattered in the backward hemisphere. If current global average aerosol optical depths are 0.1 (due to the Pinatubo eruption) then this would correspond to a cooling of 3.2 W/m^2 which is significant when compared to estimates of warming of $2\text{-}2.5 \text{ W/m}^2$ caused by anthropogenic CO_2 to date (Hansen and Lacis, 1990). Of course the most dominant radiative effects are caused by clouds which observational studies suggest have a net cooling effect of 44.5 W/m^2 and the warming effect of 31.3 W/m^2 resulting in a net cooling effect of 13.2 W/m^2 (Ramanathan et. al., 1989a, 1989b). Therefore, although clouds play the dominant role, the

magnitude of the direct influence of aerosol on the radiative balance is significant and should not be ignored.

Several investigators have also hypothesized that changes in aerosol concentrations can affect the earth's radiative balance indirectly by modifying cloud properties (ie. changes in the 13.2 W/m² cloud cooling discussed above). First Twomey (1977) and later Charlson et al. (1987) proposed that for a cloud of fixed liquid water content, an increase in the number of cloud condensation nuclei (CCN) aerosol will cause the available liquid water to be spread over a larger number of drops resulting in more but smaller cloud droplets. This increase in droplet number concentration then causes the cloud albedo to increase with little or no change in the infra-red properties of the cloud.

In addition to cloud albedo modification, increases in CCN concentrations can retard the condensational growth rate of cloud drops because more drops are competing for the available water vapor. This slowing of the drop growth can then delay and sometimes prevent the onset of the collision-coalescence process which is necessary for the production of rainfall (Takahashi, 1976) (Porter, 1988). Based on the influence of CCN on rainfall production, Albrecht (1989) has proposed that CCN induced changes in rainfall will also modify the decay (evaporation) time of marine clouds and therefore affect regional cloud cover. While these indirect influences of aerosol on cloud properties may be significant for

radiative calculations, their magnitude has been difficult to assess.

As discussed above, the direct influence of aerosol on the radiative balance is related to the aerosol optical depth which is dependant on the aerosol area distribution while the indirect effect (effect on cloud properties) is related to the aerosol number distribution. Due to the climatic importance of both the direct and indirect effects it would be beneficial to measure these aerosol properties on global scales from satellites. Unfortunately, the properties of the aerosol number distribution are not easily measured from satellite because their diameters extend to smaller sizes which scatter less light at visible wavelengths. On the other hand the aerosol area distribution, which is responsible for the aerosol optical depth, has been derived from satellite for some time.

Some of the first favorable comparisons between satellite optical depth measurements and insitu sun photometer measurements were obtained by Griggs (1975, 1983). He reported an approximate linear relationship between the aerosol component of the satellite measured radiance and the aerosol optical depth measurements from surface based sun photometers. More recently aerosol optical depth measurements have routinely been carried out on global scales at NOAA NESDIS following the Griggs method (Rao et al., 1989; Stowe et al., 1992).

While Griggs early results were encouraging, concerns remained over certain aspects of satellite optical depth measurements (Griggs, 1986). One concern raised by Durkee et al. (1991) was over the variability in the aerosol phase function. The aerosol phase function is important because it describes what fraction of light is scattered in each direction and the satellite measured radiance is directly proportional to its value under the single scattering approximation. Figure 1.1 is an example of various marine aerosol phase functions and the molecular (Rayleigh) phase function. There it can be seen that larger particles scatter more light in the forward direction while small particles scatter more in the side directions. Satellite measurements typically range over scattering angles from 80 through 180 and from figure 1.1 it can be seen that significant variability can exist in the correct phase function value for these range of scattering angles. Prior to the Durkee et al. paper, almost all of the aerosol optical depth measurements have been carried out with a fixed aerosol phase function which assumes a constant aerosol size distribution.

Variability in the aerosol size distribution and therefore the phase function can be caused by a variety of sources. Volcanic eruptions are notorious for injecting large amounts of SO_2 into the stratosphere which get converted to sulfuric acid aerosol forming the so called Junge aerosol layer. In the middle to upper troposphere, aerosol concentrations can vary

from extremely clean ($\sim 0.01 \mu\text{g}/\text{m}^3$) to enhanced desert dust or pollution layers which can be carried large distances before being removed by subsidence or cloud nucleation. Perhaps most important, the aerosol in the marine boundary layer can range from very clean background conditions ($\sim 0.05 \mu\text{g}/\text{m}^3$) to large aerosol concentrations in advected polluted air masses ($>10 \mu\text{g}/\text{m}^3$).

Aerosol in the marine boundary layer play a particularly important role due to fact that they tend to be hygroscopic and pick up large amounts of water at relative humidities lower than 100%. Due to the water associated with each aerosol they can have equilibrium sizes nearly twice their dry diameters (Tang and Munkelwitz, 1977a; Tang, 1977b) for typical marine boundary layer conditions. This increase in aerosol size results in increased scattering so that frequently a large portion of the satellite measured radiance will come from the boundary layer aerosol.

In order to illustrate the large range of variability which is possible, several aerosol size distributions measured during ship and aircraft experiments are shown in figure 1.2. From these figures we see that the accumulation mode aerosol (less than $0.5 \mu\text{m}$ diameter) can vary more than two orders of magnitude (notice scale changes from top left panel and bottom panel). The coarse mode sea salt (greater than $0.5 \mu\text{m}$ diameter) can also vary substantially depending on wind state and cloud removal rates (see top right and bottom panels).

Shown next to each aerosol mode is the aerosol composition, which was inferred by heating tests. A description of the experiments and details of the instrumentation used to obtain the measurements shown in figure 1.2 are given in chapter 3.

In light of this aerosol variability, it is expected that the aerosol phase function should also vary significantly and a method to obtain its values for each satellite pixel is required. This topic was recently investigated by Durkee et al. (1991) who employed satellite measured radiances for channels 1 and 2 from climatological satellite observation of marine and rural aerosol cases. These channel 1 and 2 satellite radiances were then combined as a ratio (channel 1 /channel 2) which were called the S12 ratio. Next the shape of the aerosol phase function was modeled with a two term Henyey-Greenstein equation which requires 3 parameters (a weighting factor and two asymmetry parameters). The value of these 3 parameters were obtained from the Shettle and Fenn aerosol model (1979) for marine and rural aerosol. In this way the satellite S12 ratio and the Henyey-Greenstein parameters were obtained for two types of aerosol conditions but from different sources. Then the 3 different Henyey-Greenstein parameters were plotted versus the S12 ratios for the marine and rural aerosol cases. Next a straight line was fit from the marine to rural case for each of the three parameters. Therefore in order to apply their method, the S12 ratio is obtained from satellite and the 3 line fits allow one to

obtain the 3 parameters required to describe the aerosol phase function with the Henyey-Greenstein equation.

The Durkee et al. method of deriving the aerosol phase function was one of the first operational methods of its kind and therefore was an important step forward but it clearly has several strengths and weaknesses. One of the strong points of the method is that it derived the S12 ratios from climatological values. Two weak points in the method are that 1) a Henyey-Greenstein equation (which was used) is not always a perfect fit to the actual phase function value and 2) the aerosol phase function values and the S12 ratios came from different sources. If the aerosol size distributions of the Shettle and Fenn model were not representative of the aerosol in the images from which the S12 ratio values came, then some error would be introduced.

In light of the importance of obtaining the correct aerosol phase function, the goal of this paper is to develop a new method of deriving the aerosol phase function from satellite. In order to do this, a large data set of marine aerosol measurements were employed to develop a marine aerosol model from which optical calculations were carried out. The new method developed here was then used to obtain aerosol optical depths from satellite and comparisons were made with ground based photometers. Error analysis was also carried out to study the effects of various uncertainties in the method.

Images from the NOAA 11 AVHRR satellite were used for this

study because they offer reasonable spatial resolution (~1km), have frequent coverage of the earth, have 5 wavelength bands which offer a broad range of observing wavelengths and they are readily accessible to a large number of investigators. The 5 observing channels of the AVHRR satellite series include a visible channel, a near infra-red (IR) channel, a channel midway between the visible and terrestrial IR and two channels near the peak of the terrestrial IR. The wavelength response for these 5 channels is shown in figure 1.3.

CHAPTER TWO

RADIATIVE THEORY AND SATELLITE MODEL

As mentioned above, measurements of aerosol optical depths from satellite have been carried out by a variety of investigators. Due to the complexity of the atmospheric scattering problem, each investigator has employed a variety of assumptions about the aerosol properties and the atmospheric scattering and absorption processes. In the following section the assumptions used here will be discussed. The radiative transfer equation as applied here for satellite work is described in the first section of this chapter. Information on the method employed to calculate sun glint is provided in the second section. The molecular and aerosol scattering and absorption is described in the third and fourth sections.

Satellite Radiative Transfer Equation

Following Liou (1980), the radiative transfer equation in a scattering atmosphere is given by:

$$1) \quad \mu \frac{dI(\tau, \Omega)}{d\tau} = I_w(\tau, \Omega) - \frac{\tilde{\omega}}{4\pi} \int_{4\pi} I(\tau, \Omega') P(\Omega, \Omega') d\Omega' - \frac{\tilde{\omega} F_o}{4\pi} P(\Omega, -\Omega_o) e^{-\frac{\tau}{\mu_o}}$$

where
 F_o = solar irradiance
 $I(\tau, \Omega)$ = radiance
 I_w = water leaving radiance
 $P(\Omega, \Omega_o)$ = scattering phase function
 μ = $\cos\theta$
 μ_o = $\cos\theta_o$
 Ω = satellite solid angle(θ, ϕ)
 Ω_o = sun solid angle(θ_o, ϕ_o)
 τ = optical depth
 $\tilde{\omega}$ = single scattering albedo.
 θ = satellite zenith angle
 θ_o = sun zenith angle
 ϕ = satellite azimuth angle
 ϕ_o = sun azimuth angle.

The first term on the right hand side accounts for the extinction of light originating at or below the surface (water leaving radiance) as it passes through the atmosphere. The second and third terms correspond to the increase in satellite measured light due to multiple scattering of diffuse light and single scattering of direct solar light. For the present study it will be beneficial to separate the light sources coming from single scattering events and those from multiple scattering events. Therefore after integration (Liou, 1980), equation 1 can be written as

$$2) I_s(0; \mu, \phi) = I_w(\tau; \mu, \phi) e^{-\frac{\tau}{\mu}} + I_m(0; \mu, \phi) + \frac{\tilde{\omega} \mu_o F_o}{4\pi(\mu + \mu_o)} P(\Theta) \left\{ 1 - e^{-\tau \left(\frac{1}{\mu} + \frac{1}{\mu_o} \right)} \right\}$$

where
 $I_s(0; \mu, \phi)$ = satellite measured radiance
 $I_w(0; \mu, \phi)$ = water leaving radiance
 I_m = various types of multiple scattered radiance
 $P(\Theta)$ = phase function
 Θ = scattering angle
 $\cos\Theta$ = $\cos\theta \cos\theta' + \sin\theta \sin\theta' \cos(\phi - \phi')$.

The last term in equation 2 describes the single scatter of light by both molecules and aerosol particles. If the scattering optical depth is small (ie. $\tau(1/\mu+1/\mu_0) \ll 1$) then this term can be linearized resulting in

$$3) \quad I_s(0; \mu, \phi) = I_w(0; \mu, \phi) e^{-\frac{\tau}{\mu}} + I_m(0; \mu, \phi) + \frac{\tilde{\omega} F_o}{\mu 4\pi} \tau P(\Theta).$$

The various light sources in equation 3 are illustrated in figure 2.1.

Since we have employed a single scattering approximation, the multiple scattering term I_m will be dropped for now and will be considered again in chapter 4. In addition the single scattering term can be modeled separately by an aerosol and a molecular term. Molecular absorption by ozone and water vapor can also be considered. This molecular absorption is assumed to take place for both the incoming solar light and the upwelling scattered light. After these modifications we obtain

$$4) \quad I_s(0; \mu, \phi) = \left\{ I_w(0, \mu, \phi) e^{-\frac{\tau}{\mu} + \frac{\tilde{\omega}_a F_o}{\mu 4\pi} \tau_a P_a(\Theta) + \frac{\tilde{\omega}_m F_o}{\mu 4\pi} \tau_m P_m(\Theta)} \right\} e^{-\tau_{abs}(\frac{1}{\mu} + \frac{1}{\mu_0})}$$

where

- $\tilde{\omega}_a$ = aerosol single scattering albedo
- $\tilde{\omega}_m$ = molecular single scattering albedo
- τ_a = aerosol optical depth
- τ_m = molecular scattering optical depth
- $P_a(\Theta)$ = aerosol phase function
- $P_m(\Theta)$ = molecular phase function
- τ_{abs} = optical depth of absorbing gases.

Water Leaving Radiance

The source of water leaving radiance in equation 4, (I_w), is caused by either subsurface scattering (sea light), surface specular reflection of the direct sun light (sun glint) or surface specular reflection of diffuse sky light (sky glint). Therefore,

$$5) \quad I_w = I_{sea\ light} + I_{sun\ glint} + I_{sky\ glint}$$

OR

$$I_w = I_{sealight} + F_o R(\alpha, W) + \int (I_{diffuse\ light} R(\alpha, W)) d\Omega_{ocn\ surf}$$

where

$R(\alpha, W)$ = ocean surface scattering coefficient (sr^{-1})

α = reflection angle

W = wind speed (m/s)

$\int d\Omega_{ocn\ surf}$ = solid angle integral over ocean surface.

The sea light portion of the water leaving radiance in equation 5 is caused by scatter from 1) the ocean bottom, 2) suspended particles or 3) ocean chlorophyll. Light scattered from the ocean bottom topography is usually only visible from satellite for ocean depths less than 10 meters depending on the wavelength and turbidity of the water. Suspended particles in the surface waters can also scatter light in coastal regions where elevated concentrations occur due to river runoff. Away from the coastlines in the open oceans the contribution from bottom topography and suspended particles is negligible.

Towards the blue end of the visible spectrum light can also be scattered by ocean chlorophyll. This feature has in

the past been used to detect ocean productivity after atmospheric corrections have been applied (Gordon and Morel, 1980). At larger wavelengths (above $0.6 \mu\text{m}$) subsurface sea light can be assumed to be negligible (Ramsey, 1968). Therefore, for the AVHRR satellite whose wavelengths are greater than $0.6 \mu\text{m}$ and for open ocean regions the subsurface scatter can be assumed to be zero.

The second source of water leaving radiance in equation 5 comes from specular reflection from the ocean surface (sun glint). If the oceans were perfectly flat then this scattered light would occur in only a small region when viewed from satellite. However, due to wind roughening and ocean swells, the ocean surface has many scattering surfaces oriented differently which causes the sea glint to spread as a function of wind speed. In the past, measurements of aerosol optical depths have typically been carried out in portions of satellite images which are away from the sun glint where the ocean albedo is quite small (ca. 0.015) (Rao et. al., 1989).

According to the Cox and Munk model (1955) the ratio of the reflected sun surface radiance to the incident flux density is proportional to the probability of finding parts of the sea surface tilted so as to reflect sun light to the observer. Following Wald and Monget (1983) this is expressed by the following expression

$$6) \quad p(\Theta, \Phi, \Theta_0, \Phi_0, V) = \frac{1}{\pi\sigma^2} \exp\left\{-\frac{\tan^2\Theta_n}{\sigma^2}\right\}$$

where

Θ_n = angle between local zenith and scattering wavelet zenith

V = wind velocity (m/s)

σ^2 = sun glint variance.

The geometry for equation 6 is illustrated in figure 2.2. The Θ_n angle used in equation 6 depends on the satellite and sun position and is be obtained by

$$7) \quad \cos 2\omega = \cos\Theta \cos\Theta_0 + \sin\Theta \sin\Theta_0 \cos(\phi-\phi_0)$$

$$\Theta_n = \arccos\left\{\frac{\cos\Theta + \cos\Theta_0}{2\cos\omega}\right\}.$$

Based on observed glitter patterns Cox and Munk found the variance of the sun glint pattern followed

$$8) \quad \sigma^2 = 0.003 + 0.00512V \pm 0.004.$$

Once the scattering probability is obtained, the sun glint scattering coefficient (Koepeke, 1985) can be calculated from

$$9) \quad R \equiv \frac{I_{sg}}{F_o \mu_o} = \left\{ \frac{\rho(\omega) p(\Theta_n, V)}{4\mu\mu_o\mu_n^4} \right\} (1 - W_f) + W_f R_f$$

where

R = sun glint scattering coefficient (sterad^{-1})

I_{sg} = upwelling sun glint (radiance)

πF_o = solar flux density (irradiance)

ω = angle of incidence and reflection

μ = $\cos(\theta)$, θ = satellite zenith angle

μ_o = $\cos(\theta_o)$, θ_o = solar zenith angle

μ_n = $\cos(\Theta_n)$, Θ_n = angle between local zenith and scattering wave zenith

$\rho_\lambda(\omega)$ = Fresnel reflection coefficient of sea water at angle ω

$p(\Theta_n, V)$ = probability of finding sea surface slope with angle Θ_n for wind velocity V

W_f = fraction of sea covered by foam

R_f = effective foam reflectance.

Following Koepke (1985), the Fresnel reflectance factor is

$$10) \quad \rho(\omega) = \frac{1}{2} \left\{ \frac{\cos\omega - \sqrt{n^2 - \sin^2\omega}}{\cos\omega + \sqrt{n^2 - \sin^2\omega}} \right\}^2 + \frac{1}{2} \left\{ \frac{n^2 \cos\omega - \sqrt{n^2 - \sin^2\omega}}{n^2 \cos\omega + \sqrt{n^2 - \sin^2\omega}} \right\}^2$$

where

n = refractive index of ocean water.

The effective wavelength of the AVHRR channels can be determined by weighting each wavelength by the solar irradiance and the channel response (see equation 24 for phase function and optical depth cases). By doing this for the AVHRR satellite it is found that the channel 1 and channel 2 average wavelengths are 0.63 and 0.83 μm . Irvine and Pollack (1968) report the index of refraction for pure water is 1.331 and 1.327 at 0.65 and 0.85 μm . Kennish (1989) reports the index of refraction for visible light of pure water is 1.333 and that of 3.5 % salinity water is 1.3398 (a 0.5 % difference). Assuming the same percentage difference for channel 2 we get an index of refraction of 1.334 for AVHRR channel 2. Figure 2.3 shows the fresnel reflection coefficients calculated from

equation 10 based on these index of refraction values. As we can see there is no discernable difference between channels 1 and 2.

The first term in equation 9 is multiplied by $(1-W_f)$ so that it describes the fraction of water which is not covered by foam. The second term accounts for the reflectance due to foam. Following Koepke (1985), the effective reflectance of foam is 0.22 which accounts for new as well as aged foam patches whose reflectance is lower. The fraction of water which is covered by foam is given by

$$11) \quad W_f = \alpha U^\epsilon$$

where

W_f = fraction of sea covered by foam .

α, ϵ = constants

U = wind speed (m/s) .

A variety of values for the constants in equation 11 have been presented in the literature. Figure 2.4 presents values of foam coverage (W_f) calculated from the constants reported in O'Muircheartaigh and Monahan (1986) and Koepke (1985). From this figure we see a large variability exists at the larger wind speeds. This variability is not surprising considering that whitecap coverage can be affected by fetch length, temperature and ocean slicks (Koepke, 1985). In the present study, the constants labeled M1-C were used ($\alpha = 2.2 \times 10^{-5}$, $\epsilon = 2.71$) since this curve was near the center of the range of possible values shown in figure 2.4.

With the above assumptions, calculations from equation 9

are shown in figure 2.5 for different wind speeds as a function of θ_n . Here we can see that as the wind decreases, the reflectance increases at the spectral point. More importantly the inclusion of foam creates an isotropic scattering surface at larger θ_n which is independent of scattering angle. For the present study only satellite pixels with θ_n values larger than 30 degrees will be employed and a constant wind speed of 7 m/s will be assumed. The errors caused by different wind speeds will need to be addressed in the error study discussed in chapter 6.

The final term in equation 5 is the diffuse sky glint term which must be determined by considering multiple scattering interactions between the ocean surface, aerosol and molecules. Correctly modeling this term is quite difficult and has been attempted by relatively few investigators (Nakajima, 1983). For the present study the diffuse sky glint term has been neglected. This assumption is not expected to create large errors for several reasons. First, the diffuse light appearing at various angles off the sun is more than four orders of magnitude lower than the direct beam. In addition the majority of the light which is scattered in the atmosphere will be scattered in the forward direction. For this forward scattered light, the ocean reflection coefficient is quite small for the sun-satellite geometries employed here for aerosol retrieval.

Molecular Scatter and Absorption

For the model developed here, the Rayleigh scattering optical depths used in equation 4 were calculated from

$$12) \quad \tau_m = 0.008569\lambda^{-4} (1 + 0.0113\lambda^{-2} - 0.00013\lambda^{-4})$$

where
 λ = wavelength (μm).

The use of this equation follows the work of Tiellet (1990) who has compared a variety of equations addressing this problem. The Rayleigh optical depth is also directly proportional to the ground pressure so that the ratio of the actual Rayleigh optical depth to the average Rayleigh optical depth equals the ratio of the actual pressure to the average pressure (Andre and Morel, 1989). This variation in the Rayleigh optical depth due to pressure fluctuations was not included in the model but was considered in the error study (chapter 6). The Rayleigh scattering phase function was calculated from

$$13) \quad P_m(\theta) = \frac{3}{4} (1 + \cos^2(\theta)).$$

In this equation the weak depolarization factor has been ignored (Liou, 1980).

Molecular absorption for AVHRR satellites is primarily caused by ozone absorption lines occurring in channel 1 and water vapor lines for channel 2. This molecular absorption is represented by the (τ_{abs}) term occurring at the end of equation 4. For both ozone and water vapor, the molecular

concentrations were converted to absorption optical depths by the radiative calculations of Sanders and Edwards (1989). Figure 2.6 illustrates how changes in water vapor affect the channel 2 water vapor absorption optical depth. In this figure the 5 points represent tropical, midlatitude summer, US Standard, midlatitude winter and subarctic winter soundings (Sanders and Edwards, 1989). The line was obtained by a curve fit and is given by

$$14) \tau_{abs} = 0.004023 + 3.49897 \times 10^{-3} w - 4.73751 \times 10^{-5} w^2 + 3.39102 \times 10^{-7} w^3$$

where

τ_{abs} = molecular absorption optical depth
(here for water vapor)

w = total water vapor content ($\frac{kg}{m^2}$).

As can be seen from figure 2.6 the water vapor absorption optical depths can vary substantially. Therefore, in order to derive the total water vapor from AVHRR satellites, the method devised by Dalu (1986) was employed. In the Dalu method the integrated water vapor is obtained by

$$15) \quad w = A(T_4 - T_5) \cos(\theta)$$

where

w = water vapor content $\left\{ \frac{kg}{m^2} \right\}$

$A = 19.6 \left\{ \frac{kg}{K m^2} \right\}$

T_4 = channel 4 radiometric temperature

T_5 = channel 5 radiometric temperature.

Dalu obtained this equation by performing radiative transfer calculations for 18 different representative moisture and

temperature profiles. His model calculations suggested errors in equation 15 would be below $\pm 1.5 \text{ kg/m}^2$ but comparisons of satellite derived water, from equation 15, and insitu soundings gave errors up to $\pm 5.0 \text{ kg/m}^2$, possibly due to temporal and spatial differences.

While the Dalu method allows the AVHRR satellite to perform measurements of the atmospheric water vapor, there is no method to derive the ozone concentration from the AVHRR satellite. Therefore, for the present study the geographic and time of year variations in ozone concentrations were obtained from the Van Heuklon (1979) model which is based on the archive of surface column measurements.

Aerosol Scatter

The second term on the right of equation 4 accounts for the scattering of light by aerosol towards the satellite. Unlike molecules which either absorb or scatter at a certain wavelength, the aerosol can exhibit a range of absorbing characteristics depending on the imaginary part of the index of refraction of the particle. The aerosol single scattering albedo describes the amount of light scattering versus absorption and is calculated by

$$16) \quad \omega_a = \frac{\beta_s}{\beta_e} = \frac{\beta_s}{\beta_s + \beta_a}$$

where

β_s = aerosol scattering coefficient
 β_a = aerosol absorption coefficient
 β_e = aerosol extinction coefficient.

The aerosol absorption coefficient is calculated by

$$17) \quad \beta_a = \int_0^\infty k_\lambda \frac{dN}{d \log D} d \log D$$

where

k_λ = single aerosol absorption coefficient = $\frac{4\pi m_i}{\lambda}$
 m_i = imaginary part of refractive index.

The aerosol scattering coefficient is calculated from

$$18) \quad \beta_s = \int_0^\infty (\pi r^2) Q_s \frac{dN}{d \log D} d \log D$$

where

Q_s = aerosol scattering efficiency
 r, D = the aerosol radius, diameter
 $dN/d \log D$ = aerosol number distribution
with
 $(\pi r^2) Q_s = \sigma_s$ (aerosol scattering cross section).

The aerosol scattering efficiency in equation 18 is calculated from

$$19) \quad Q_s = \frac{1}{x^2} \int_0^\pi [i_1(\theta) + i_2(\theta)] \sin \theta d\theta$$

where

$i_{1,2}(\theta)$ = intensity parameters MIE theory
 $x = \frac{2\pi r}{\lambda}$ (size parameter)
 λ = light wavelength.

The aerosol phase function also appears in equation 4 and for unpolarized light is given by

$$20) \quad P_a(\theta) = \frac{(i_1(\theta) + i_2(\theta))}{2k^2\sigma_s}$$

where

$$k = \frac{2\pi}{\lambda} = (\text{wavenumber})$$

$$\sigma_s = Q_s(\pi r^2) = (\text{scattering cross section}).$$

Both the molecular phase function, equation 7, and the aerosol phase function, equation 20, are normalized so that

$$21) \quad \int_0^{2\pi} \int_0^\pi P(\theta) \sin\theta \, d\theta \, d\phi = 4\pi.$$

The aerosol optical depth appearing in equation 4 can be calculated from

$$22) \quad \tau_a = \int_0^\infty \beta_a(z) \, dz$$

where

$$\beta_e = \beta_a + \beta_s.$$

Typically for remote marine regions, the scattering coefficient is more than an order of magnitude larger than the absorption coefficient so that the majority of the optical depth in equation 22 comes from aerosol scatter. In order to get a better understanding of what makes up the scattering component of the optical depth, the terms involved in the calculation of equation 18 are shown in figure 2.7. The top panel shows a typical marine aerosol as a volume distribution where the sulfate accumulation mode has a mass of $0.46 \mu\text{g}/\text{m}^3$ and sea salt coarse mode has a mass of $3 \mu\text{g}/\text{m}^3$. In this figure each diameter has been shifted to larger diameters by a factor of 1.6 to account for water uptake in the marine atmosphere.

The second panel is the same aerosol distribution shown as a number distribution which is used in equation 18. The next panel shows the aerosol scattering cross section $Q_s(\pi r^2)$. For this panel a mixture of sulfuric acid and water was assumed for the accumulation mode and the index of refraction came from Palmer and Williams (1975). For the coarse mode, a mixture of sea salt and water aerosol was assumed and the index of refraction of Shettle and Fenn (1976) was used. From panels 2 and 3 it can be seen that while the number distribution drops at larger diameters, the scattering cross section increases. The bottom panel shows the differential scattering coefficient which was obtained by multiplying panel 2 with panel 3 for each diameter. The total scattering coefficient (equation 18) can be found by integrating the area under the curve in the bottom panel of figure 2.7.

After the aerosol optical depths are calculated from the aerosol size distribution then the satellite measured radiance can be calculated from equation 4. For this calculation the spectral solar irradiance was obtained from Iqbal (1983). The AVHRR channel 1 and 2 spectral response functions were obtained from Kidwell (1991) at wavelength intervals of 0.01 μm . In order to calculate the aerosol scattered radiance for each AVHRR channel, the radiance at each wavelength was added together so that

$$23) \quad I_s = \sum_{\lambda=1}^N \left\{ \frac{F_\lambda R_\lambda \bar{\omega} \tau_\lambda P_\lambda(\Theta)}{4\pi\mu} \right\}$$

where

R_λ = channel response function.

A disadvantage of this equation is that the phase function cannot be separated from the optical depth. Therefore, a different form was also employed so that the phase function and the aerosol optical depth can be brought out of the summation. Here

$$24) \quad I_{ss} = \bar{P}(\Theta) \bar{\tau} \sum_{\lambda=1}^N \left\{ \frac{\bar{\omega} F_\lambda R_\lambda}{4\pi\mu} \right\}$$

where

$$\bar{\tau} \equiv \frac{\sum_{\lambda=1}^N \tau_\lambda F_\lambda R_\lambda}{\sum_{\lambda=1}^N F_\lambda R_\lambda}$$

$$\bar{P}(\Theta) \equiv \frac{\sum_{\lambda=1}^N P_\lambda(\Theta) F_\lambda R_\lambda}{\sum_{\lambda=1}^N F_\lambda R_\lambda}.$$

If the phase function and optical depth were totally uncorrelated then the two methods would equal. As it is, they are slightly correlated and there is a difference between the scattered radiance calculated from equations 23 and 24. Further discussion of these equations is given in chapter 4.

CHAPTER THREE

AEROSOL MODEL

In the single scattering approximation (eq. 4) the satellite measured radiance is directly proportional to the aerosol phase function. It is therefore important to study the range of possible aerosol phase functions. In order to carry out these tests, realistic marine aerosol size distributions are required.

In the past, several people have developed models to describe the size dependence of marine aerosol. Shettle and Fenn in an Air Force report (1979) developed standard aerosol size distributions for rural, urban and maritime aerosol and studied the optical properties of the aerosol as a function of the ambient relative humidity. The Navy also developed an aerosol model which predicted the aerosol size distribution as a function of wind speed, fetch and the parcel travel time from any land mass (Garthman, 1982,1984).

More recently D'Almeida et. al (1991) have developed a global climatology of aerosols and their radiative characteristics. Here a study of a large data set of insitu marine aerosol measurements has been carried out to develop a new marine aerosol model. This new model is believed to provide a better representation of the marine aerosol distribution than previous aerosol models.

Instrumentation

The aerosol measurements described here took place in a variety of experiments and in different locations (figure 3.1). The measurements include three ship experiments, 1) the Second Soviet American Gas and Aerosol Experiment (1987) (SAGA2) across the Pacific and Indian Oceans, 2) the Third Soviet American Gas and Aerosol Experiment (1989) (SAGA3) in the Central Pacific and 3) a trip of opportunity aboard the Japanese Research vessel Kaiyoumaru (1991) also in the Central Pacific. Aerosol measurements were also performed on two aircraft experiments and include, 1) the Central Pacific Atmospheric Chemistry Experiment (1989) (CPACE) and the Atlantic Stratus Transition Experiment (1992) (ASTEX). In addition aerosol measurements were also taken at Mauna Loa during January-March 1988 (MABIE) (Clarke and Porter, 1991a).

During these experiments, aerosol size distributions were measured with two instruments, 1) a custom optical particle counter (OPC) and 2) a differential mobility analyzer (DMA) (sometimes called an electrostatic aerosol classifier). The customized OPC sized particles into 256 diameters ranging from 0.16 up to 7.5 μm . Calibrations for the OPC were performed using latex spheres of various sizes and ammonium sulfate aerosol generated by the DMA. Further details are contained in Clarke (1990). The DMA (TSI model 3071) was used in conjunction with a condensation nuclei counter (TSI model 3760) to measure the aerosol size distribution from 0.02-0.5

μm diameter following the method of Covert (personal communication). For both systems, thermal volatility of the aerosol size distributions was used to infer the aerosol composition as being either sulfuric acid (volatile at 150 C), ammonium sulfate/bisulfate (volatile at 300 C) or sea salt, soot or dust which are not volatile at 300 C. (Clarke, 1990). During aircraft experiments, aerosol were sampled under isokinetic conditions to minimize large particle loss. System losses were calculated and included in the aerosol distributions discussed here. Further information on the aircraft isokinetic sampling design and intercomparisons are given in Porter et. al. (1992).

Accumulation Mode Marine Aerosol

In order to develop an accumulation mode aerosol distribution model the measurements taken by the DMA were utilized since they extended to smaller sizes than the OPC and also covered the majority of the accumulation mode at the larger diameters. The first step in analyzing the collected aerosol size distributions was to convert the measured accumulation mode distributions into dry distributions by shifting each diameter downward based on measured sample relative humidities and assumed aerosol compositions. This diameter shift was typically fairly small since relative humidities in the DMA were typically below 15%. In order to carry out this process, it was assumed that the common marine

aerosol accumulation mode consists primarily of a mixture of sulfuric acid and ammonium bisulfate (ie. a molar ratio of NH_4/SO_4 somewhere between 0 and 1). This molar ratio assumption was based on a large number of marine aerosol volatility tests performed during the various experiments shown in figure 3.1. In light of this frequently observed molar ratio fraction, laboratory studies were performed (using the OPC and DMA systems) with various NH_4/SO_4 molar ratio solutions from 0 to 1. These results are shown in figure 3.2 and are labeled mixture. In the same figure, the equilibrium drop sizes for sulfuric acid, ammonium bisulfate and salt have been shown (Tang et. al, 1977a; 1977b; 1980). As expected the laboratory results fall between the Tang et al. curves for sulfuric acid and ammonium sulfate. While it is expected that these results are reasonably correct, it is believed that these studies could be better carried with two tandem DMAs which were not available at the time of the study. In any case the laboratory results were used to convert the measured accumulation mode aerosol to dry diameters. The use of these same laboratory results has produced good agreement when comparing OPC size distributions with filter measurements in the past (see figure 11 of Porter et. al., 1992).

Once all the aerosol distributions measured by the DMA were converted to dry distributions, then each one was sorted based on its dry aerosol volume and put into different averages. Therefore, for example, all the low mass cases were

averaged together to develop one size distribution and the same for the high aerosol mass cases to develop a different size distribution. For the present study, 9 aerosol volume ranges were chosen and are (< 0.05), (0.05-0.1), (0.1-0.2), (0.2-0.4), (0.4-0.8), (0.8-1.6), (1.6-3.2), (3.2-6.4) and (6.4-12.8) $\mu\text{m}^3/\text{cm}^3$. Assuming the accumulation mode density is the average of sulfuric acid and ammonium bisulfate then the aerosol density is approximately 1.81 and the aerosol mass ranges employed here are (< 0.09), (0.09-0.2), (0.2-0.36), (0.36-0.72), (0.72-1.45), (1.45-2.9), (2.9-5.8), (5.8-11.6), (11.6-23.2) $\mu\text{g}/\text{m}^3$.

The results of this process for aerosol measurements during the SAGA3, Kaiyoumaru and ASTEX experiments (see figure 3.1) are shown as number distributions in figures 3.3 and 3.4. During the SAGA3 experiment the impactor which removed aerosol larger than 0.5 μm diameter was not working correctly and this caused a slight aerosol enhancement at the larger sizes (near 0.4 μm). Despite this small effect, the SAGA3 measurements are considered to be mostly correct below 0.2 μm and therefore can be used along with the measurements from the other experiments to study the behavior of the accumulation mode aerosol. By looking at the averages from all three experiments we can see two predominant aerosol peaks typically exist. A relatively steady peak occurring near 0.18 μm diameter which is commonly known as the accumulation mode and a second peak appearing below 0.1 μm . The second peak at smaller diameters

is too large to be called a nucleation mode and therefore will be referred to here as a transitory accumulation mode since aerosol are passing through it as they coagulate to larger sizes. By comparing the various cases we can also see the position of this transitory accumulation mode peak is quite variable (0.02 to 0.09 μm) which means developing a aerosol model for this transitory mode will be difficult. In fact during the ASTEX experiment the peak diameter of this mode shifted so much that averaging all the cases together would have produced a broad and unrealistic aerosol distribution. Therefore, the aerosol averages shown in figure 3.4 include the majority but not all of the cases from that experiment and were chosen from cases with the transitory accumulation mode near the lower limits of the DMA scans (0.02 μm).

While the position of the transitory accumulation mode is important for determining the number of aerosol which will become activated in clouds, for satellite purposes we are interested in the aerosol scattering coefficient which depends on the aerosol area distribution (see eq. 18). In the bottom panel of figure 3.4 the aerosol averages from the ASTEX experiment are plotted as area distributions. Here we can see that the transitory accumulation mode includes little of the total area. It also demonstrates that as the aerosol area concentration increases the peak of the accumulation mode tends to shift to larger sizes. In order to develop a combined aerosol model, similar plots from the SAGA3 and Kaiyoumaru

experiments were combined and each resulting aerosol average was fit as the sum of 2 log normal curves. The resulting size distributions are shown in figure 3.5 and the parameters for the each curve are given in table 1.

The most prominent feature of the average size distributions shown in figure 3.5 is the shift of the peak diameter to larger diameters as the concentration increases. In fact, the shift from the smallest aerosol distribution ($\sim 0.08 \mu\text{m}$) to the largest aerosol distribution ($\sim 0.27 \mu\text{m}$) is larger than the aerosol diameter shift caused by the hygroscopic nature of the sulfate aerosol for the normal range relative humidities occurring in the cloud free marine atmosphere (50-80%) (see figure 3.2).

Coarse Mode Marine Aerosol

In order to develop an aerosol model for the coarse mode, OPC measurements from the SAGA2 and SAGA3 experiments were used and grouped by dry aerosol volume in the same way as the accumulation mode model which was discussed above. For the coarse mode, the aerosol were first heated to 300 C which volatilized the sulfate accumulation mode. After this heating process, the only remaining aerosol were refractory and were composed of either sea salt, dust or soot. In order to detect the presence of either dust or soot, filter measurements were collected and analyzed for light absorption (Clarke, 1989). Based on the filter light absorption and radon measurements

(Porter, 1988), only the size distributions collected during the clean time periods were used for this study.

As discussed earlier, in order to determine the dry diameter of the accumulation mode, each diameter of the measured distribution had to be shifted to smaller sizes based on the measured instrument relative humidity and figure 3.2. This process was not necessary for the coarse mode salt aerosol because they were heated to 300 C and remain dry in the system. The reason for this is the hysteresis effect of sea salt which dries out at 40% but does not pick up water until approximately 70% relative humidity (Tang, 1977A, 1977B, 1980). For all cases, the measured relative humidity following the heater in the aerosol sampling system was less than 70% (typically 30%) due to either dilution with dry air or system heating of the air stream. Therefore, no correction for water uptake was applied to the measured coarse mode sea salt aerosol.

In taking aerosol measurements for the coarse mode, care must be taken to correct for aerosol transmission losses which occur in the sampling system. For the present system, gravitational losses in horizontal lines have been modeled according to the formulation of Schwendiman as reported by Okasaki and Willeke [1987], impaction losses in tube bends from the empirical studies of Piu et al. [1987] and tube inlet losses from the empirical studies of Okasaki and Willeke [1987]. While the Okasaki and Willeke (1987) inlet studies are

suitable for ship measurements, they are less suitable for aircraft studies since they only studied straight nozzles at wind speeds up to 10 m/s. Unfortunately no other studies are available to address aerosol losses of diffusing nozzles at typical aircraft speeds. Figure 3.6 shows the cumulative estimated losses for both our ship and aircraft measurements. For the aircraft measurements, the transmission losses have been shown for NaCl for both dry and wet conditions.

In Porter et. al. (1992) the OPC coarse mode aerosol was corrected for transmission losses and comparisons were made with an external FSSP probe and good agreement was found under dry conditions. On the other hand, for marine boundary layer cases with high relative humidities, comparisons with predicted and modeled subisokinetic coarse mode aerosol concentrations were not in good agreement suggesting unmodeled coarse mode aerosol losses were occurring in the sampling inlet. Therefore, in order to test the validity of the transmission loss correction, the OPC aerosol distributions were plotted alongside the aerosol measurements performed by Woodcock (1953) with glass slides exposed to ambient air conditions from flying aircraft. In order to do this comparison, OPC aerosol averages were chosen so that they had equal concentrations at the smaller sizes of the Woodcock aerosol distribution (0.9 to 2 μm diameter). Figure 3.7 is an example for one case and suggests the OPC size distribution is undercounting dramatically above 2 μm diameters. Other OPC

averages had similar results. Therefore, in order to develop a model for sea salt, the OPC size distributions were used for the lower portion of the distribution and the Woodcock aerosol model for the larger diameters and two log normal curves were combined to fit the total salt distribution.

The resulting salt aerosol size distributions are shown in figures 3.8 where each distribution is shown as a function of wind force (Beaufort scale) based on the Woodcock paper (1953). The lognormal parameters for each curve are given in table 2. In developing these cases some interpolation was required because Woodcock only measured aerosol distributions for wind forces of 1, 3, 4, 5, 7 and 12. The resulting aerosol model for the coarse mode (figure 3.8) is similar to the accumulation mode model (figure 3.5) in that as the concentration increases the peak diameters shift to larger sizes.

CHAPTER FOUR

SATELLITE RESPONSE TO AEROSOL CASES

As aerosol optical depths increase, the multiple scattering component becomes increasingly important. The multiple and singly scattered satellite radiation are studied in the first section of this chapter and based on these studies a simple method is obtained to derive the single scattered component from the total satellite measured radiance for nonabsorbing aerosol cases.

The next section of this chapter studies the satellite response for many different aerosol distributions and different satellite and sun viewing geometries. Based on the modeled satellite response, a method is developed to derive the aerosol phase function value from the ratio of channels 1 and 2. Finally the influence of several different types of aerosol layers on the present method is discussed.

Single Scatter Versus Multiple Scatter

In any effort to determine the aerosol properties from aerosol scattered radiance, particular attention must be given to the single scatter component since it is the portion that will give information about the aerosol size distribution and not the multiple scatter component. Therefore, for measurements of scattered radiance it would be beneficial to subtract off the multiple scattered component and obtain the

single scattered component. In order to study the possibility of obtaining an equivalent single scattered component from the measured total scattered radiance, the satellite measured radiance will now be modeled by 1) the Nakajima and Tanaka (1988) discrete ordinates model, 2) the single scatter assumption (SS) (equation 2) and 3) the linearized single scatter assumption (LSS) based on equation 4. For the present study, the discrete ordinates model results are assumed to be more correct and will serve to test the SS and LSS models. The exact forms used for single scattering (SS) and linearized single scattering (LSS) are given by

$$25) \quad LSS = \left(\frac{F_0 \tau_a P(\theta)}{\mu 4 \pi} + \frac{F_0 \tau_m P(\theta)}{\mu 4 \pi} \right) e^{-\tau_{abs} \left(\frac{1}{\mu} + \frac{1}{\mu_0} \right)}$$

$$SS = \left[\left(\frac{F_0 \mu}{4 \pi (\mu + \mu_0)} \right) \left(1 - e^{-\tau_a \left(\frac{1}{\mu} + \frac{1}{\mu_0} \right)} \right) + \left(\frac{F_0 \mu}{4 \pi (\mu + \mu_0)} \right) \left(1 - e^{-\tau_m \left(\frac{1}{\mu} + \frac{1}{\mu_0} \right)} \right) \right] e^{-\tau_{abs} \left(\frac{1}{\mu} + \frac{1}{\mu_0} \right)}$$

The aerosol phase function values used in equation 25 and all the calculations discussed below were calculated from a modified Bohren and Huffman Mie code, BHMIE, (Bohren and Huffman, 1983). Results from the BHMIE code were compared with the Diermendjian (1969) calculations and found to be in excellent agreement. Typical gaseous absorption optical depth were used in equation 25 (0.03 for channel 1 and 0.041 for channel 2) (Sanders and Edwards, 1989).

Several parameters employed by the Nakajima and Tanaka (1988) discrete ordinates program are now discussed. The

single scatter albedo and the effective phase function required by the discrete ordinates method were calculated by

$$26) \quad \omega = \left(\frac{\tau_a + \tau_m}{\tau_a + \tau_m + \tau_{abs}} \right)$$

$$P(\theta) = \frac{\tau_a P_a(\theta) + \tau_m P_m(\theta)}{\tau_a + \tau_m}.$$

The surface albedo was set to zero for these studies in order to not introduce any error caused by a lambertian surface assumption and in addition to allow for the direct comparison between single and multiple scatter. This surface albedo assumption is not far from correct for regions far from the sun glint. In employing the discrete ordinates method, the accuracy of the calculations depends on the number of discrete ordinates employed. The number of required quadrature points increases as the effective phase function becomes more peaked. On the other hand, as the number of quadrature points increases the computational time also increases dramatically. In light of this problem, several investigators have developed truncation methods which serve to reduce the number of quadrature points required to obtain accurate results. Nakajima and Tanaka (1988) have compared computations from several truncation methods with computations carried out with a large number of quadrature points. Their results show that their IMS truncation method can give errors less than 1% with the number of discrete ordinates as small as 10. For the calculations discussed here the Nakajima model was used and

the number of discrete ordinates was set to 20 so that any error caused by insufficient number of quadrature points will be less than 1%.

The results of the comparison of the three radiative methods is shown in figure 4.1. For these calculations the aerosol phase function was held constant and the aerosol optical depths were varied from 0.03 to 0.9 which covers a wide range of realistic values. The satellite and solar zenith angles were varied from 0 to 70 degrees (steps of 10 degrees), and the azimuth angle difference between the sun and the satellite was varied from 0 to 180 degrees in steps of 20 degrees resulting in a total of 920 different comparisons. In figure 4.1 the LSS, the SS and the MS satellite measured radiance have been plotted versus the LSS satellite radiance, therefore the LSS curve is a straight line since it is plotted versus itself. From this figure it can be seen that at small radiance values the difference between all three methods is quite small. In addition, at larger values the LSS method overestimates the satellite measured radiance while the SS method underestimates it.

The effective phase function used in figure 4.1 came from equation 26 and is a combination of the molecular phase function (eq. 13) and the aerosol phase function. The aerosol size distribution came from the aerosol shown in figure 2.7 which is a common marine aerosol distribution. In addition the aerosol were shifted to larger diameters by 1.6 to account for

the uptake of water in the moist marine boundary layer (see figure 3.2). This shift in diameters is correct for the accumulation mode but is too small for the coarse mode sea salt. As will be shown below, this small error will not change the conclusions drawn here. The index of refraction of both the accumulation mode and the coarse mode took into account the uptake of water (Palmer and Williams, 1975; Shettle and Fenn, 1979).

Since the natural aerosol distributions can vary substantially, it is natural to ask how the results shown in figure 4.1 would change for different aerosol size distributions. Therefore the calculations done for figure 4.1 were repeated for an aerosol distribution characteristic of the free troposphere instead of the marine boundary layer. This aerosol case included only a sulfate accumulation mode with a mass of $0.13 \mu\text{g}/\text{m}^3$ and no coarse mode. To account for the uptake of water in the free troposphere, with an assumed relative humidity of 35%, each diameter was shifted to larger diameters by 1.29. Next the aerosol and molecular scatter as well as ozone absorption were included in the model (eq. 26). The results were almost indistinguishable from figure 4.1 and suggest that after considering significant (but not extreme) changes in the aerosol distributions the multiple to single scattering relationship remains similar. The calculations done in figure 4.1 included all viewing geometries, some of which would have produced sun glint contamination. Therefore

additional calculations were carried out for non-sun glint conditions only and the results were very similar to figure 4.1 with the only difference being that fewer points were plotted.

Since a single aerosol optical depth can produce several satellite measured radiances depending on the viewing geometry it is difficult to interpret figure 4.1 in terms of the aerosol optical depth. In order to help in this regard, the LSS satellite radiance for figures 4.1 was plotted versus the model aerosol optical depth in figure 4.2. Here the 12 different aerosol optical depths used in figure 4.1 can be seen and can be used to interpret figure 4.1 in terms of aerosol optical depth.

The relationship between the various methods shown in figure 4.1 suggest the linearized single scattering (LSS) values can be obtained from the satellite radiance even for large optical depths. With these results it becomes possible to investigate aerosol scattering as a single scattering process which has the advantage that the aerosol and molecular scatter as well as absorption can be separated and calculated individually as was done in equation 25. It should be emphasized here that these results apply to nonabsorbing aerosol cases only. Therefore, these calculations are appropriate for remote marine regions (possibly half of the world) which are not dramatically affected by continental aerosol.

AVHRR Channel Ch1/Ch2 Ratio

In the following section, the satellite optical response is studied for a large number of aerosol cases with the linear single scatter assumption. For these tests the aerosol single scattering component was calculated from equation 24 for an aerosol layer of only 1 km with no Rayleigh scatter or absorption applied. Each aerosol case consisted of a combination of coarse and accumulation mode aerosol and in no cases were two different aerosol layers considered. The reason for calculating the satellite response for a single aerosol type and not various layers of different types of aerosol will be discussed below after the modeling results are presented.

The aerosol cases studied here were developed from 6 coarse mode and 7 accumulation mode aerosol distributions which were chosen from the aerosol model developed in chapter 3. The various accumulation/coarse mode combinations resulted in 42 aerosol cases. In addition, the 42 different cases were repeated for relative humidities of 75%, 35%, and 15% with the accumulation and/or coarse mode diameters shifted to larger diameters based on their hygroscopic nature (see figure 3.2). This process resulted in 338 different aerosol cases. The index of refraction used for the accumulation and coarse were based on Shettle and Fenn (1979) for the hygroscopic salt aerosol and on Palmer and Williams (1975) for the sulfate accumulation mode.

The aerosol phase functions were calculated from equation

24 for all aerosol cases and are shown in figure 4.3. Here we can see that in the region between 80 to 130 degrees the value of the phase function can vary over more than an order of magnitude but that the largest concentration of cases fall within factors of 2 to 3 from each other. It is this variability in the phase function that is of concern for measuring the aerosol optical depth from satellite.

As discussed in section 2d, the correct way to calculate the satellite radiance is from equation 23 which sums up the satellite measured radiance for each wavelength contribution over the channel interval. This formulation has the disadvantage that a different aerosol phase function value is required for each wavelength. The advantage of calculating the satellite measured radiance from equation 24 is that only a single weighted phase function value is required. The disadvantage of this form is that, as discussed previously, error can occur due to correlation between the phase function and the aerosol optical depth. The error in equation 24 is illustrated in figure 4.4a and 4.4b for AVHRR channels 1 and 2 where the error in equation 24 is presented as the percentage difference between the satellite radiance calculated from equations 23 and 24. For this figure the various scattering angles resulted from satellite and sun zenith angles which varied from zero to 70 degrees and the sun-satellite azimuth angle differences which varied from 0 to 180 degrees. These various viewing geometries resulted in 710

scattering angles being calculated for each aerosol case. In light of this error, a correction factor $K=I_s/I_{ss}$ (I_s and I_{ss} come from equations 23 and 24) has been applied to the phase function values derived from equation 24 for all the results discussed below. In this way the satellite measured radiance calculated from equation 24 is corrected for the error shown in figures 4.4a and 4.4b.

Shown in figures 4.5 through 4.8 are the phase function values (calculated from eq. 24 with correction applied) plotted versus the satellite channel ch1/ch2 radiance ratios for fixed scattering angles. For these figures the channel ratios were calculated from equation 23 and therefore are the correct ratios. Also plotted is the 3rd order line fit to the data points.

From these figures we can see several features. For scattering angles less than about 60 degrees the data points and the curve fit curves downward near ratio values of 3.5. This curve means that a certain phase function value corresponds to two different ratio values. Once scattering angles of 80 through 100 degrees are reached then the data points become lined up so that each ratio value corresponds to a single phase function values on the line fit.

For the back scattering angle of 180 degrees (figure 4.8), we can see that for ratio values less than 2, the phase function value is unpredictable but as the ratio shifts to larger values (corresponding to smaller aerosol) then some

information becomes available in the backscattered ratio. This same feature can be seen for all the backscattering angles from 170 through approximately 120 although not as extreme as at 180.

The larger ratio values which show up in each of the figures 4.5-4.8 correspond to model aerosol distributions with small diameters and little associated water. These aerosol conditions are only present in the free troposphere or the stratosphere where relative humidities are low and water uptake by the aerosol is small. In addition the aerosol modeling done in chapter 3 suggest that the presence of predominantly small aerosol diameters such as those discussed here, will only occur during low aerosol mass concentrations.

Aerosol Layers

Both aircraft and balloon measurements have shown that the atmosphere is composed of several types of aerosol layers which vary with height. When several aerosol types occur in the atmospheric column then the resulting effective column size distribution must be broader than any of the individual distributions. In modeling the satellite response for different aerosol conditions, two choices are possible, one can either try to include many different aerosol layers in the calculation or one can study the satellite response for a single aerosol size distribution and try to combine the various aerosol layers later. The results shown in figures

4.5-4.8 were based upon the second approach and illustrate the satellite response for each individual aerosol distribution. The broad aerosol distribution which would occur for several aerosol layers in the column were not modeled there. The effect of the presence of a layered atmosphere upon the phase function retrieved from the above mentioned figures will now be discussed.

Referring back to figure 4.6, consider the case where one aerosol layer had ratio values of 2 while another at a different altitude had a value of 3. Upon viewing this layered atmosphere from satellite, the effective phase function will be the average phase function of the two layers weighted by their optical depths. The reason the resulting phase function can be claimed to be a weighted average phase function is that the single scattering assumption has been applied. From figure 4.6 it can be seen that the weighted average of two phase functions from two aerosol layers will also fall near the line since it is approximately straight. On the other hand for the scattering angles shown in figure 4.5 the curved response creates the possibility that the average phase function for two aerosol layers will not fall near the line and some error in the derived phase function value will occur.

In addition to mixing two aerosol cases with different ratio values it is also possible to mix two aerosol with similar ratio values but different phase function values. This can be illustrated in figures 4.7 or 4.8 where the scatter

about the line fit is rather large for small ratio values. For these cases it is likely that if various aerosol layers are present then the mix of aerosol layers would draw the effective phase to the center of the cluster and therefore closer to the line.

As discussed above, the effective phase function for two aerosol layers is given by the weighted average of the two individual phase functions. The channel ch1/ch2 ratio on the other hand is not simply the "sum of the ratios" from two aerosol layers but is given by the "ratios of the sums" so that the

$$27) \quad \text{Correct Ratio} = \frac{L_{A,1} + L_{B,1}}{L_{A,2} + L_{B,2}}$$

and the

$$28) \quad \text{Incorrect Ratio} = \frac{L_{A,1}}{L_{A,2}} + \frac{L_{B,1}}{L_{B,2}}.$$

The use of figures 4.5-4.8 implies the use of the "sum of ratios" method which is not correct. Therefore, in order to use these figures properly the ratio for each layer would have to be known. Since there is no way to obtain the radiance for each individual aerosol layer from satellite, this is not possible and some error will occur in using figures 4.5-4.8. In order to estimate the magnitude of this error, various combinations of channel 1 and channel 2 radiance values were

assigned for two different hypothetical aerosol layers. Next, the ratios were calculated correctly and incorrectly from equations 27 and 28. The percentage difference between the two methods is shown in figure 4.9 where it can be seen that if the difference in ratios between the two layers is less than 2, then the error in the weighted average ratio (eq. 28) will be less than 10%. Considering the scatter around the line shown in figures 4.5-4.8, this error is small and therefore the weighted average of the ratio can be considered as being approximately correct and various different aerosol layers will not significantly detract from the method developed here.

In conclusion, the results presented in this chapter have described several aspects of the problem of measuring aerosol optical depths from satellites. Results from the first section of this chapter demonstrated a relationship between linear single scatter radiance values and multiple scatter radiance values for nonabsorbing aerosol. This relationship between the single and multiple scatter radiance allows one to obtain the single scattered component from the total radiance and subsequently the Rayleigh and water leaving radiance can be modeled separately under the single scattering assumption.

Model calculations of the aerosol phase function for numerous realistic aerosol cases suggested that radiance coming from aerosol scatter can be used to derive the aerosol phase function with an accuracy which depends on the viewing geometry and the ratio value. For the common backscattering

angles of 120 through 180, small ratio values (less than 2) had more uncertainty in the derived phase function value while larger ratio values had less scatter in the derived phase function value. The presence of several different aerosol layers should not present a serious problem and in fact may serve to improve the method.

CHAPTER FIVE
SATELLITE AND INSITU COMPARISONS

Based on the discussion presented in chapters 2 and 4, a model was developed to analyze AVHRR satellite images and obtain the aerosol optical depths. All of the satellite images used for this study were NOAA 11 satellite images of the Hawaii island region and were taken from the anonymous ftp service provided by Dr. Pierre Flament at aurelie.soest.hawaii.edu. One particular image collected on March 27, 1993 is plotted below and is used to illustrate various aspects of measuring aerosol properties from satellite. In order to calibrate the channel 1 and channel 2 radiances, the method presented by Tiellet and Holben (1993) and Kidwell (1991) was used here.

The next section of this chapter discusses surface based sun photometer measurements carried out on Oahu during the spring of 1992. Comparisons between surface and satellite derived optical depths are then shown.

Hawaiian AVHRR Image: March 27, 1993

Various aspects of processing AVHRR images to obtain the aerosol optical depths have been discussed throughout this paper. These will be briefly summarized now as they were applied in a computer model. The first step in processing the images was to flag as bad data all pixels which fell

within the sun glint region as discussed in chapter 2. Next the radiance for each sun glint-free pixel was converted from multiple scattering to an equivalent linear single scattering based on the relationship shown in figure 4.1. The next step was to subtract off the radiance coming from Rayleigh scatter and foam glint and to increase the radiance to account for either ozone absorption for channel 1 or water vapor for channel 2. The methods employed to derive the ozone and water vapor optical depths were discussed in chapter 2. Once the aerosol single scatter was obtained it was used to obtain the aerosol ratio for channels 1 and 2. Next this ratio was used to derive the aerosol phase function based on chapter 4 and figures 4.5 to 4.8. Once the aerosol phase function was obtained the aerosol optical depth was calculated for each pixel.

In order to flag for clouds, the channel $ch1/ch2$ ratio derived above was used. The value of the ratio at which the pixel was called a cloud or an aerosol was chosen as the smallest ratio values shown in figures 4.5 to 4.8. The logic behind this choice is that all the cases shown in figures 4.5 to 4.8 were derived from realistic aerosol cases and therefore should be cloud free (although some were rather extreme). If the ratio value is smaller then it corresponds to larger aerosol which at some point begins to describe cloud drops. From figures 4.5 to 4.8 it can be seen that the cloud threshold values depend on the scattering angle.

An example of the model results are given in figures 5.1 through 5.4. The original image shown in figure 5.1 was collected on March 27, 1993 and shows the Hawaiian Islands under relatively cloud free conditions. In this particular image it can be seen that the trade winds are slightly more easterly than usual and that the Big Island rain bands are forming slightly south of their normal position. Weather maps for this period indicated that a cold front was located 1000 km northwest of the islands and that the winds weakened on the western edge of the image where they switched from easterly to southeasterly as they passed through the surface ridge. The scattering angles for this image range from 135 to 165 degrees going from the lower left to the upper right of the image. The sun glint region is not present in this image and occurs off the lower left of the image.

Shown in figure 5.2 is the aerosol optical depth calculated from figure 5.1 with the model described above. A histogram of the image is also shown illustrating which optical depth corresponds to each color. Although there are various optical depths present in the image, the predominant background value is approximately 0.1.

Immediately obvious in this image is the volcano plume from the Big Island with aerosol optical depth values up to 0.3 and more. The Big Island volcano has been active for some 10 years and the volcanic plume has been measured as far as 1000 km away from ship observations (Clarke and Porter,

1991b). In other parts of the image it can be seen that the ratio method has captured the majority if not all of the clouds in figure 5.1. Surrounding many cloud regions are areas of larger aerosol optical depths. It is not certain if these higher aerosol optical depth areas are due to partial cloudiness in the pixel or simply larger aerosol due to higher relative humidities surrounding cloud regions. Spatial homogeneity could be employed to remove these areas but at this point it is not certain that these regions should be removed. Future comparisons with high spatial resolution imaging instruments such as the Landsat or the AVIRIS instrument could resolve these problems.

The aerosol channel $ch1/ch2$ ratio used in deriving the clouds and the aerosol phase function is shown in figure 5.3. Here several interesting features can be seen. Referring back to figure 5.1 it can be seen that cloud pixels appear as dark blue ratio values while cloud free areas range from light blue through red corresponding to larger through smaller aerosol. The land masses also show up clearly as very low ratio values. For this study all ratio values less than 1 were set to 1 and from the large peak in the histogram present at 1 it would appear many values were below 1.

Both AVHRR channels 1 and 2 are affected by molecular absorption. As discussed earlier in chapter 2, the ozone column concentrations which affects channel 1 was modeled by the seasonal dependant model of Van Heuklon (1979) and the

water vapor column concentrations were obtained from the Dalu method from AVHRR channels 4 and 5. The column water vapor concentrations for figure 5.1 are shown in figure 5.4. The dominant feature appearing in figure 5.4 is the high water vapor trails behind the islands of Hawaii, Maui, Oahu and possibly Kauai. This water vapor trail is possibly caused by surface wind convergence in the lee of each island. In addition a large area of high water vapor appears south of Kauai possibly due to the combined effect of the whole island chain and the weakening of the winds in that region causing low level convergence.

Besides the high vapor regions, very low water vapor regions can be seen on either side of the island of Hawaii. Although the cause of these low water vapor zones is difficult to determine without adequate measurements, several possible mechanisms can be mentioned. As the winds pass around the Island of Hawaii, they experience an acceleration which may cause a wind divergence resulting in a lowering of the trade wind inversion. A lowering of the trade wind inversion will decrease the total column water vapor amount. A different mechanism can be found in the fact that these dry regions are occurring downwind of rainy regions on the windward side of the Big Island (compare the dry regions in figure 5.4 with clouds seen in figure 5.1). This upwind rainout will remove liquid water thereby preventing subsequent evaporation during the downslope subsidence on the lee side of the Big Island.

Comparison of Ground and Satellite Measurements

In order to test the present method of deriving the aerosol optical depth, sun photometer measurements were carried out on the windward side of Oahu (Bellows Beach) during April through July 1992. The sun photometer employed here was a single wavelength (550 nm) shadowband radiometer developed by Batelle Laboratories.

For this instrument, the direct solar radiation is obtained from the difference between the total and diffuse radiation. Values were saved once every minute. In order to analyze the data and remove cloudy periods, the Langley method was employed for AM and PM data. In the Langley method, the logarithm of the sensor voltage is plotted versus the air mass, where the air mass is the reciprocal of the cosine of the solar zenith angle. For a cloud-free day, the slope of the data points plotted in this way is the optical depth. Further details of this method can be found in Shaw (1983). In order to develop the Langley plot, only the largest radiance values measured in a particular air mass range (ie. 0.1) were used. In addition, only values collected between air mass values of 1.5 and 5 were employed in order to obtain a significant aerosol signal and avoid multiple scattering effects (John Regan, personal communication). Large air mass values were calculated from Kasten (1965) in order to account for the fact that the atmosphere is not a plane parallel atmosphere. The next step in processing the data was to fit a straight line to

the data. All points falling 1% lower than the line were removed and a new line was fit with the remaining data. This process was continued until either all data points fell within 1% of the line or too few values remained to be useful. This process served to remove cloudy periods from the data set. The results of this process are illustrated in figure 5.5.

The Langley fit method described above was used to process daytime AM and PM optical depths. The aerosol optical depths derived from this process for the data collected with the shadow band radiometer at Bellows are shown in figure 5.6. Also shown in this figure are aerosol optical depths derived from the satellite method discussed earlier. In order to derive the satellite values, the average values of a box centered near the Island of Oahu were used. The box dimensions were approximately 200 by 200 km and extended further upwind than downwind. The reasons for using such a large box was to remove certain sampling errors which are discussed in chapter 6. The satellite passes used here typically occurred near 4 PM since earlier passes had sun glint contamination problems. Typically more than half of the images used here were cloudy and therefore only part of the box was useful. In fact only the comparisons carried out on day 112 and 113 were reasonably cloud free upwind of the sampling site at the time of the satellite overpass and even these were cloudy over the sampling site at the time of the satellite overpass.

In addition to the Bellows and the satellite optical depth

measurements, aerosol optical depths taken at NOAA Mauna Loa station during the same time period are shown in figure 5.6. The NOAA Mauna Loa station is located near 3 km altitude which is slightly above the marine boundary layer (approx. 2 km) so that differences between the Bellows and Mauna Loa optical depth values come from the marine boundary layer contribution. Figure 5.6 therefore suggests the marine boundary layer was contributing approximately 0.05 to the optical depth during this time period while the upper troposphere and stratosphere were contributing approximately 0.1. The large variability seen in all three optical depth values is largest in spring and become smaller into the summer which is consistent with a decay in the Asian dust transport during the spring to summer transition.

While there is reasonable agreement between the surface and satellite derived aerosol optical depths shown in figure 5.6, it is considered that the present study is not of sufficient duration to determine the accuracy of the satellite algorithm developed here. One of the main difficulties of the present comparison was caused by enhanced cloudiness during the sampling period. Comparisons during the spring of 1993 would have produced a much larger number of clear days.

Future aerosol optical depth measurements will needed to adequately test the satellite algorithm and should be carried out from both island and ship sites. It is considered that a large number of surface measurements from ship stations would

be preferable because they avoid several problems associated with island sites such as wave spray and island blocking effects such as enhanced cloudiness and increases in aerosol diameter due to changes in relative humidity as the air rises upwind of the island.

CHAPTER SIX

ERROR ANALYSIS

In developing the current AVHRR aerosol model several assumptions were employed. In this section the possible error associated with these assumptions will be studied.

Sensor Precision Effects

The images taken by the AVHRR satellite are 10 bit resolution and range from approximately zero to 90 % albedo. Because the aerosol signal can at times be quite small it can create strange results in the images which are processed for aerosol optical depth. This sensor-induced effect is now discussed.

If we begin with an AVHRR image which is cloud free, has no sun glint and has a constant aerosol optical depth, then the satellite measured radiance will depend on the scattering angle. This occurs because both the Rayleigh and the aerosol signal are angle dependant due to their respective phase functions. Therefore at some particular point in going through the range of scattering angles, the satellite sensor must pass from one particular count value to another. Since the resolution of the AVHRR is rather coarse (10 bits), these regions of similar count values may be rather large. In processing AVHRR images in order to derive the aerosol optical depth, the Rayleigh radiance is removed by calculating its

contribution for each scattering angle. The Rayleigh radiance calculated in this way is continuous and therefore one is subtracting different Rayleigh radiances from a broad region of the image which has a constant count value. In doing this one can produce artificial stripes of similar values in the resulting radiance images.

An example of the problem described above is illustrated in figure 6.1a where the right hand panel was obtained by subtracting the left panel (with high resolution) from the central panel (with coarse resolution). Striped lines of constant value are clearly seen in the right panel. In terms of AVHRR images, the central panel would correspond to the unprocessed satellite measured radiance while the left panel corresponds to the calculated Rayleigh radiance which is to be subtracted off.

An example of this striping effect in a real image is given in figure 6.1b. This is the same image shown in figure 5.2 except that a different enhancement has been applied (compare the histograms for each image). From the histogram provided in figure 6.1b, it can be seen that stripes in the image all fall within a range of aerosol optical depths of approximately 0.03. It should be mentioned that the stripes are aligned along lines of constant scattering angle as expected and that the scattering angles range from 135 to 165 from the lower left to the upper right of the image.

These illustrations raise the question of how to avoid

this problem. Near the center of a region of equal counts, the count value is the correct value and the subtraction of the Rayleigh radiance at this point leads to a correct aerosol radiance. Upon subtraction of the Rayleigh radiance, the values on the left and right of the center will be either too low or too high depending on which scattering angle is being considered.

In order to remove these stripes from the processed image it is necessary to smooth out the step features of the initial satellite image. Therefore it is desirable to determine the minimum amount of spatial averaging required to carry out this process. For this study the phase function for the aerosol distribution shown in figure 2.7 was used. The procedure used here was to vary (both up and down) the range of scattering angles from a central scattering angle until the difference between the satellite measured radiance at the central scattering angle and the edge scattering angle were more than or at least equal to the radiance which would come from a single AVHRR count. Then averaging the satellite radiance over that range of scattering angles would be sufficient to remove the step nature of the image and make slowly varying radiance values which will not produce stripes when the Rayleigh scatter is removed.

The results for this study are shown in figures 6.2. There it can be seen that the largest range of scattering angles which must be covered to remove this striping effect occurs

for scattering angles of 120 degrees. The reason for this is that at this scattering angle both the aerosol and the Rayleigh phase functions bottom out and are fairly flat so that one must go fairly far in either direction to encounter any substantial change in phase function values and therefore the satellite radiance. In addition it can be seen in these figures that the range of scattering angles required to smooth out the image drops as the aerosol optical depth increases. The reason for this is that as the aerosol optical depth increases, the range of phase function values takes the satellite measured radiance through a greater range of satellite counts.

Error Analysis of Various Terms Influencing Satellite Derived Optical Depth

In the present model (chapter 5), several models have been employed here to describe sun glint, molecular scatter and molecular absorption. It is now useful to perform a error analysis to estimate the impact of errors in the various terms.

Equation 4, which was described earlier can be written as

$$29) \quad I_S = (I_A + I_R + I_G) e^{-\tau_o \left\{ \frac{1}{\mu_o} + \frac{1}{\mu} \right\}}$$

or

$$I_A = I_S e^{\tau_o \left\{ \frac{1}{\mu_o} + \frac{1}{\mu} \right\}} - I_R - I_G.$$

where

I_A = Satellite Measured Aerosol Radiance

I_S = Total Satellite Measured Radiance

I_R = Satellite Measured Rayleigh Radiance

I_G = Satellite Measured Sun Glint Radiance

τ_G = Optical Depth Due To Gas Absorption.

The errors in equation 29 occur due to uncertainty in sensor calibration, sensor noise, ozone concentrations, water vapor concentrations, Rayleigh scattering optical depths and the sea surface scattering coefficients. For this study it will be assumed that the errors in each term will have random fluctuations which follow a normal distribution and that the absolute uncertainty of each term corresponds to a 3 standard deviation error which includes 97% of the possible error cases. The assumptions for the absolute error of each term are given now.

Following Sanders and Edwards (1989) the primary gaseous absorption for AVHRR channel 1 is due to ozone. In the present study the ozone concentrations are modeled from Van Heuklon's (1979) climatological model. Next the model converts the column ozone concentrations to ozone absorption optical depths based on Sanders and Edwards (1989). From Sanders and Edwards, the typical atmospheric transmittance due to ozone is 0.97 (ie. $\tau_{abs} = 0.03$). For the present error calculations it will

be assumed that this ozone concentration can vary from the modeled climatological value by an absolute value of $\pm 25\%$.

For channel 2, Sanders and Edwards report the primary absorbing gas is water vapor. Their relationship between precipitable water vapor concentration and channel 2 optical depth was illustrated earlier in figure 2.6 in chapter 2. As mentioned there, the Dalu method (equation 15) can be used to measure the atmospheric water vapor from the infrared AVHRR channels 4 and 5. Comparisons between soundings and this method had errors up to $\pm 5 \text{ kg/m}^2$ for a large range of water vapor contents. From Sanders and Edwards (1989) the tropical, mid-latitude summer, US-standard, mid-latitude winter and sub-arctic winter soundings have water contents of 41.7, 29.6, 14.3, 8.6 and 4.2 kg/m^2 of water vapor. Because we are concerned with open ocean regions it will be assumed that the atmospheric precipitable water content is 25 kg/m^2 which we will assume can be derived from satellite to within $\pm 5 \text{ kg/m}^2$ (an error of 20%). From figure 2.6, 25 kg/m^2 corresponds to a water vapor absorption optical depth of 0.068 and a 20% uncertainty in the water vapor causes the optical depth to range from approximately 0.057 to 0.075 (ie. average $\Delta\tau_{\text{abs}} = 0.009$). Therefore, for the current study the Dalu method will be employed and a absolute error in τ_{abs} of 13% will be assumed.

For regions away from the sun glint the sea surface reflection is isotropic and has a constant value (see figure 2.5). In the present model only this isotropic portion of the

satellite image is used and an average wind speed of 7 m/s is assumed. Due to the uncertainty in wind speed and the uncertainty in foam coverage as a function of wind speed an absolute error of 100% will be assumed for both the sea surface reflection coefficient R and the sun glint light measured by the satellite.

The next uncertainty to be addressed is Rayleigh scattering which depends on the Rayleigh optical depth given in equation 12. Uncertainties in this equation arise mainly from variations in surface pressure. In order to determine an absolute uncertainty, the surface pressure will be allowed to vary by ± 20 mb from the standard value of 1013 mb. These assumptions result in a $\pm 2\%$ absolute error in both the molecular optical depth and the Rayleigh scattered light seen by the satellite.

Also of concern is the sensor noise. Following Kidwell (1991) the signal to noise ratio of the AVHRR channels 1 and 2 is 3 to 1 for a 0.5% albedo signal. This corresponds to a noise level of $\pm 0.167\%$ albedo or radiances of approximately ± 0.10 W/m² sr for channel 1 and 0.127 W/m² sr for channel 2 and will be used here as the absolute error.

In addition to the sensor noise, channels 1 and 2 also tend to experience drift problems. Determining the extent of the drift has typically been ascertained by comparing aircraft measured radiances with satellite measured radiances over high albedo regions such as desert sands (Holben et al., 1990) or

optical calculations based on sun photometer measurements over regions of low albedo such as the ocean (Mitchell and O'Brien, 1992). In performing sensor calibrations of this type it is to be expected that the errors in a series of sensor calibrations will follow a normal distribution. The reason for this uncertainty in the calibration is primarily due to fluctuations in the surface albedo with time and space, variability in atmospheric constituents (aerosol, ozone etc.) and error in the calibration of the aircraft or surface sensor. Since fluctuations in the surface albedo and atmospheric aerosol will affect the calibration of both channels 1 and 2, it can be assumed that the errors in the sensor calibration for channels 1 and 2 will be correlated.

In order to provide a time series of sensor drift correction factors, Tiellet and Holben (1993) have fit a curve to numerous satellite corrections which have been published. Holben et al. (1990), which is one of the calibration efforts included in the Tiellet and Holben model, report an absolute error of $\pm 6.0\%$ in their calibrations. Therefore for the present study the absolute error of 6.0 % will be assumed.

The cumulative error from all the above sources will now be determined. Following Bevington (1969) the variance or the one standard deviation cumulative error of equation 29 is given by

$$30) \quad \sigma_{I_A}^2 = \sigma_{I_S}^2 \left\{ \frac{\partial I_A}{\partial I_S} \right\}^2 + \sigma_{\tau_g}^2 \left\{ \frac{\partial I_A}{\partial \tau_g} \right\}^2 + \sigma_{I_R}^2 \left\{ \frac{\partial I_A}{\partial I_R} \right\}^2 + \sigma_{I_G}^2 \left\{ \frac{\partial I_A}{\partial I_G} \right\}^2$$

where

σ_{I_A} = standard deviation error for the aerosol radiance

σ_{I_S} = standard deviation error for satellite measured
radiance

σ_{τ_g} = standard deviation error for absorption gas optical
depth

σ_{I_R} = standard deviation error for rayleigh radiance

σ_{I_G} = standard deviation error for surface reflected
radiance.

In order to evaluate equation 30 a model was developed in which the satellite and sun zenith angles were varied from 0 to 70 degrees and the satellite-sun azimuth angle difference was varied from 0 to 180 degrees. Each particular satellite-sun geometry resulted in a different aerosol scattering angle. The results from these calculations for channel 1 are shown in figure 6.3 where four aerosol optical depths are shown (ie. 0.05, 0.1, 0.2 and 0.3) and one standard deviation errors were employed for the error terms discussed above. In this figure, the one standard deviation cumulative error for the derived aerosol radiance has been shown as a percentage difference from the total aerosol radiance. In these figures it can be seen that the cumulative error becomes larger near 120 degrees scattering angle. The reason for this is that the aerosol phase function drops off at these angles causing the aerosol radiance to become weaker and therefore the cumulative error in the derived aerosol increases. In other words, if the aerosol signal is strong then uncertainties in the other terms will cause less error and visa-versa. In this figure the

smallest errors (lower line of points) occur when the satellite zenith angle is large (in this case 70 degrees) and the largest errors occur for small satellite zenith angles. In other words, when the satellite looks through a larger portion of the atmosphere (larger zenith angle) then it will get a stronger aerosol signal and less error.

Of all the errors included in figure 6.3, only the error in the calibration of the sensor drift is closest to being a systematic bias. All the others are truly random errors which presumably could be reduced or removed by performing either spatial or temporal averaging of sufficient magnitude. Of the various random errors it is expected that the error caused by sensor noise will be reduced most rapidly in performing spatial or temporal averaging. Therefore in order to test this possibility, the error for channel 1 was recalculated with the sensor noise set to zero (figure 6.4). Next all the random errors were set to zero in figure 6.5 so that the errors in this figure are only caused by the bias resulting from an incorrect calibration of the sensor drift. In figure 6.5 the different aerosol optical depth cases (0.05, 0.1, 0.2, 0.3) were plotted on the same figure. From figures 6.3 through 6.5 we can see that the error can decrease substantially if sufficient averaging is carried out. Since the water vapor is determined by satellite (chapter 2) it is also likely that error in its estimation will also rapidly approach zero with spatial averaging. On the other hand, in order to decrease

the error in the assumed ozone concentration, the Rayleigh scatter (which depends on the surface pressure) and the foam coverage (which depends primarily on wind speed) it is likely that temporal averages will be needed (ie. averaging over a week to a month of satellite images). In attempting to remove the random errors by performing image averages, the seasonal averages of ozone concentrations and wind speeds could be used for the region of interest.

Figures 6.6, 6.7 and 6.8 show similar calculations for channel 2. Several things should be mentioned here. For channel 2, smaller aerosol optical depths were employed (0.0425, 0.085, 0.17 and 0.255) due to the fact that the aerosol optical depth typically drops off with wavelength. This decrease in aerosol optical depth should increase the cumulative error. At the same time the Rayleigh scatter for channel 2 is smaller than channel 1 which causes the aerosol signal to become a larger portion of the total satellite measured radiance. The net effect of these two processes causes the channel 2 cumulative error to be similar to the channel 1 cumulative error. Again the cumulative error decreases significantly if the random errors can be removed by either spatial or temporal averaging.

As discussed earlier, the ratio of the aerosol signal for AVHRR channels 1 and 2 can be used to derive information about the shape of the aerosol size distribution and therefore the aerosol phase function. From equation 29 this is given by

$$31) \quad R = \frac{I_{S1} e^{\tau_{G1} \left(\frac{1}{\mu_0} + \frac{1}{\mu} \right)} - I_{R1} - I_{G1}}{I_{S2} e^{\tau_{G2} \left(\frac{1}{\mu_0} + \frac{1}{\mu} \right)} - I_{R2} - I_{G2}}$$

The cumulative error in equation 31 is found in a similar manner to equation 30 but now it is possible that error cancellation can occur for terms which are correlated. For example an error in the sun glint for channel 1 in the numerator will to some extent cancel with the error in the denominator. Following Bevington (1969), the variance or the one standard deviation error of the channel 1 and 2 aerosol ratio (S12 ratio) is given by

$$32) \quad \sigma_{S12}^2 = \sigma_{IS1}^2 \left\{ \frac{\partial R}{\partial I_{S1}} \right\}^2 + \sigma_{IS2}^2 \left\{ \frac{\partial R}{\partial I_{S2}} \right\}^2 + \sigma_{\tau_{G1}}^2 \left\{ \frac{\partial R}{\partial \tau_{G1}} \right\}^2 + \sigma_{\tau_{G2}}^2 \left\{ \frac{\partial R}{\partial \tau_{G2}} \right\}^2 \\ + \sigma_{R1}^2 \left\{ \frac{\partial R}{\partial I_{R1}} \right\}^2 + \sigma_{R2}^2 \left\{ \frac{\partial R}{\partial I_{R2}} \right\}^2 + \sigma_{G1}^2 \left\{ \frac{\partial R}{\partial I_{G1}} \right\}^2 + \sigma_{G2}^2 \left\{ \frac{\partial R}{\partial I_{G2}} \right\}^2 \\ + 2\sigma_{IS1}\sigma_{IS2} \left\{ \frac{\partial R}{\partial I_{S1}} \right\} \left\{ \frac{\partial R}{\partial I_{S2}} \right\} + 2\sigma_{IR1}\sigma_{IR2} \left\{ \frac{\partial R}{\partial I_{R1}} \right\} \left\{ \frac{\partial R}{\partial I_{R2}} \right\} \\ + 2\sigma_{IG1}\sigma_{IG2} \left\{ \frac{\partial R}{\partial I_{G1}} \right\} \left\{ \frac{\partial R}{\partial I_{R2}} \right\}$$

where

- σ_{I_A} = one standard deviation error for aerosol radiance
- σ_{I_s} = one standard deviation error for satellite measured radiance
- σ_{τ} = one standard deviation error for gas absorption optical depth
- σ_{I_r} = one standard deviation error for rayleigh radiance
- σ_{I_g} = one standard deviation error for surface reflected radiance.

In equation 32 the last three terms will be negative because one of the derivatives is negative and therefore error cancellation will occur. Next equation 32 was evaluated for many different satellite and sun viewing geometries in the

same manner as equation 30. Shown in figure 6.9 is the error in the ratio for aerosol optical depths of (0.05, 0.1, 0.2 and 0.3) and 1 standard deviation error values for all the random and bias errors. In this calculation the standard deviation values for the satellite sensor σ_{IS1}^2 and σ_{IS2}^2 included random sensor noise and the bias term while the covariance terms ($\sigma_{IS1}\sigma_{IS2}$) only included the bias term. This is because the sensor noise of the two channels is not correlated but the calibration bias is, as discussed above. From these figures we can see the error in the ratio can be quite large for low aerosol optical depths. As discussed above, if either spatial or temporal averaging is performed by averaging over some region or averaging together several images then the random noise error should rapidly decrease. Shown in figure 6.10 is the error in the ratio for aerosol optical depths of (0.05, 0.1, 0.2 and 0.3) where all the error terms were set to the one standard deviation value except that the sensor noise for channel 1 and 2 were set to zero. Here we can see a dramatic reduction in the cumulative error between figures 6.9 and 6.10 which can be obtained by performing either spatial or temporal averaging. If climatological wind speeds and ozone concentrations are used then it would be possible to reduce all the random errors by performing temporal averages. This possibility is investigated in figure 6.11 where all the random errors have been set to zero except the calibration bias. This results in only a slight improvement.

From the present study it can be seen that spatial or temporal averaging is very important in reducing the error and removing the stripes in the derived aerosol optical depth images. The current study has given a initial indication of the amount of averaging (figure 6.2) which is needed but further studies in this area are needed.

CHAPTER SEVEN

CONCLUSION

This paper has studied various aspects of the retrieval of aerosol optical depths from satellite. One of the main goals has been to develop a method to derive the aerosol phase function from AVHRR satellite images by employing both channels 1 and 2.

In order to study the satellite response to various aerosol size distributions, a new aerosol model was developed for the aerosol accumulation and coarse mode. This new model was based on a large data set of aerosol measurements taken over the North Pacific, South Pacific, North Atlantic and Indian oceans as well as coarse mode salt measurements of Woodcock (1953). The resulting aerosol model suggests that both the accumulation mode and the coarse mode gradually shift to larger diameters as their concentration increases. The parameters for the aerosol model are given in tables 1 and 2.

Based on the above aerosol model, the satellite response was modeled for 338 different aerosol size distributions with the single scattering assumption. Results from this process provided a relationship between the AVHRR ch1/ch2 ratio and the aerosol phase function. Several layers of different types of aerosol are not likely to significantly detract from the ability to obtain the aerosol phase function from satellite but may reduce the error of the derived phase function.

While the single scatter radiation is important as discussed above, under certain conditions multiple scattering can account for a significant portion of the total radiance. In order to compare single and multiple scattering, calculations were carried out for a variety of viewing geometries and aerosol optical depths. For the present study, two types of aerosol were used, one with an enhanced coarse mode and another with no coarse mode. Based on this study, a relationship was developed which allowed one to obtain the single scattering component from the total radiation.

Next AVHRR satellite images were analyzed to obtain aerosol optical depths. In order to flag clouds in the image, the ratio of channels ch1/ch2 was used and the ratio cutoff values were determined from the modeling study performed above with the various aerosol distributions. One NOAA 11 image of the Hawaiian Islands (March 27, 1993) was presented as an example of the procedure. Several interesting features show up in the processed image including a strong volcanic plume coming from the island of Hawaii with optical depths up to 0.35, background optical depths near 0.1 and strong gradients in the water vapor near the Hawaiian islands.

In order to test the current method, comparisons between optical depths obtained from satellite and surface based sun photometer measurements were carried out. Surface measurements were obtained from a shadowband radiometer and were processed using the Langley plot method. Optical depths from satellite

images were averaged over a 200 by 200 km region. Comparisons of the optical depths derived from the two methods were in good agreement although the present comparisons were not ideal due to enhanced cloud cover during the sampling period.

Several factors can cause error in measurements of aerosol optical depths from satellite. In the present study the error caused by the coarse digitization of the AVHRR satellite was studied. Both model examples and real images show how this problem produces artificial stripes in the derived aerosol optical depths. In order to smooth out the image radiance values and remove this problem, the image radiance values must be averaged over a range of scattering angles which varies depending on the aerosol optical depth and the scattering angle itself.

In addition to poor digitization, the retrieval of aerosol optical depth can suffer from sensor drift uncertainties, sensor noise, ozone error, water vapor error, rayleigh scatter error, and error in the sun glint or whitecap coverage estimation. Each of these errors were combined and found to produce large cumulative errors which depended on the aerosol optical depth, the satellite zenith angle and the scattering angle. Further studies found that a significant reduction in the error could be achieved through either spatial or temporal averaging which minimized random errors.

It is important to keep in mind that the work done here must be viewed as an important but limited step in developing

accurate optical models for the marine atmosphere. In particular, for the present calculations, the single scattering albedo was set to 1. This assumption is suitable for major portion of the remote marine atmosphere but over increasingly large regions of the marine atmosphere the influence of continental aerosol is observed in the form of anthropogenic soot aerosol or naturally occurring dust aerosol. These continental aerosols can drive the single scattering albedo down and cause the satellite measured radiance to underestimate the true aerosol optical depth. The present study has not focused on these continental aerosols but on marine aerosol. Further studies will be needed in order to estimate the extent to which continental aerosol affect major portions of the global marine atmosphere.

Table 1: Aerosol parameters for the two lognormal curves used to model the dry sulfate accumulation mode number distribution. Shown in the first column is the aerosol case and the number of measured aerosol distributions used in developing the model for that aerosol volume range. Each measured aerosol distribution was averaged over a time period varying from 15 minutes up to 3 hours.

Case	MASS $\mu\text{g}/\text{m}^3$	NUMBER $\#/\text{cm}^3$	GMD (1)	STD σ_1	CONSTANT (1)	GMD (2)	STD σ_2	CONSTANT (2)
1-0	0.059	164	0.0997	1.40	8.938	0.04239	1.65	10.72
2-3	0.134	193	0.1196	1.40	15.780	0.04724	1.65	12.95
3-11	0.263	261	0.1372	1.40	24.280	0.04960	1.65	17.95
4-81	0.552	289	0.1539	1.40	42.310	0.05570	1.65	18.62
5-40	1.097	367	0.1714	1.40	69.050	0.06056	1.65	22.59
6-18	2.208	464	0.1921	1.35	114.50	0.07870	1.65	31.09
7-7	4.380	666	0.2143	1.32	172.20	0.1162	1.52	74.67
8-20	8.670	1078	0.2350	1.25	218.40	0.1583	1.50	223.8
9-20	17.39	2196	0.2416	1.24	536.80	0.1310	1.49	337.4

Table 2: Same as table 1 but now for the coarse mode sea salt aerosol.

CASE	MASS $\mu\text{g}/\text{m}^3$	NUMBER $\#/\text{cm}^3$	GMD (1)	STD σ_1	CONSTANT (1)	GMD (2)	STD σ_2	CONSTANT (2)
1	0.69	4.10	1.366	1.70	0.2911	0.2750	2.00	2.010
2	1.47	4.80	1.407	1.85	0.5277	0.3033	2.05	2.470
3	3.13	5.90	1.339	2.00	1.104	0.3226	2.10	3.050
4	6.7	7.20	1.721	2.00	1.438	0.3690	2.20	4.210
5	12.96	9.00	1.523	2.30	2.484	0.3490	2.30	4.550
6	18.7	10.8	1.773	2.30	2.530	0.3970	2.45	6.070
7	26.5	11.5	2.050	2.30	2.607	0.4420	2.55	7.060
8	56.9	13.65	2.807	2.40	2.617	0.4935	2.70	9.080
9	136	16.6	3.380	2.55	3.743	0.4800	2.80	10.36
10	315	18.2	4.100	2.64	5.319	0.5070	2.88	11.60
11	711	21.3	4.720	2.74	7.960	0.5290	2.95	13.70
12	1654	24.9	5.570	2.85	11.40	0.6000	3.00	17.80

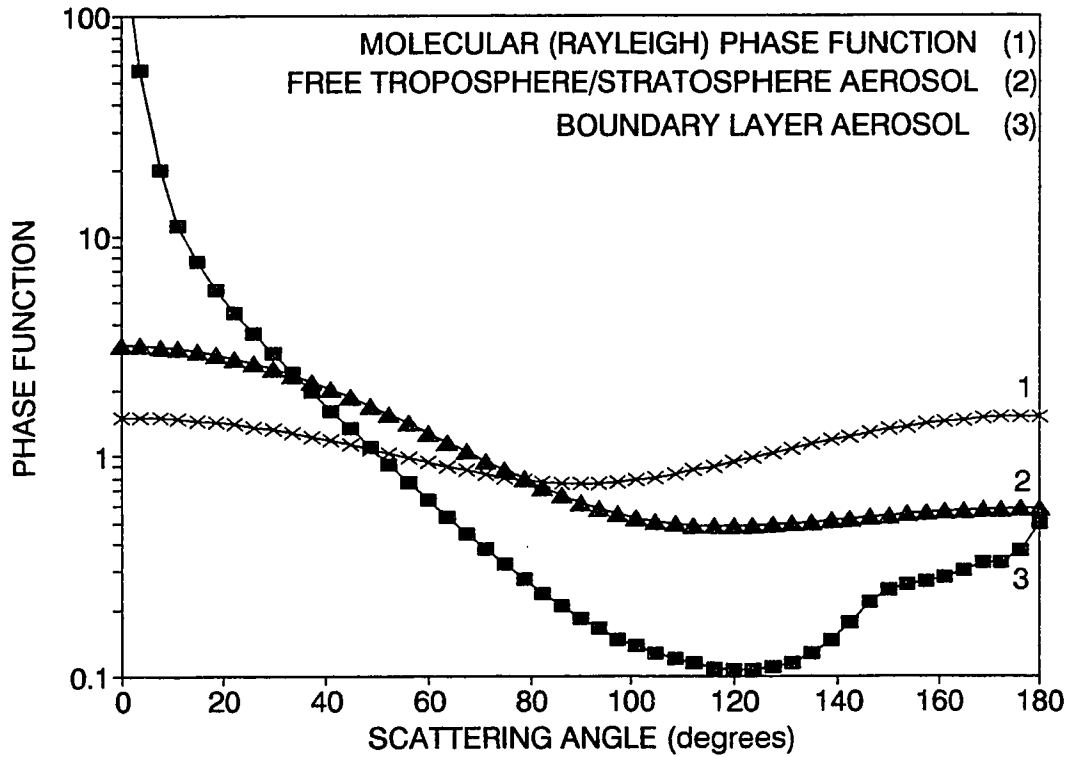


Figure 1.1. Examples of two aerosol phase functions as well as the molecular phase function. For the marine aerosol case the distribution had salt and sulfate concentrations of 3.13 and 0.55 $\mu\text{g}/\text{m}^3$ and the distribution was shifted to larger diameters by a factor of 1.9 and 1.6 to account for the uptake of water at high relative humidities. The free troposphere/stratosphere case had a concentration of 0.55 $\mu\text{g}/\text{m}^3$ and was shifted to larger diameters by a factor of 1.15 to account for the uptake of water at lower relative humidities.

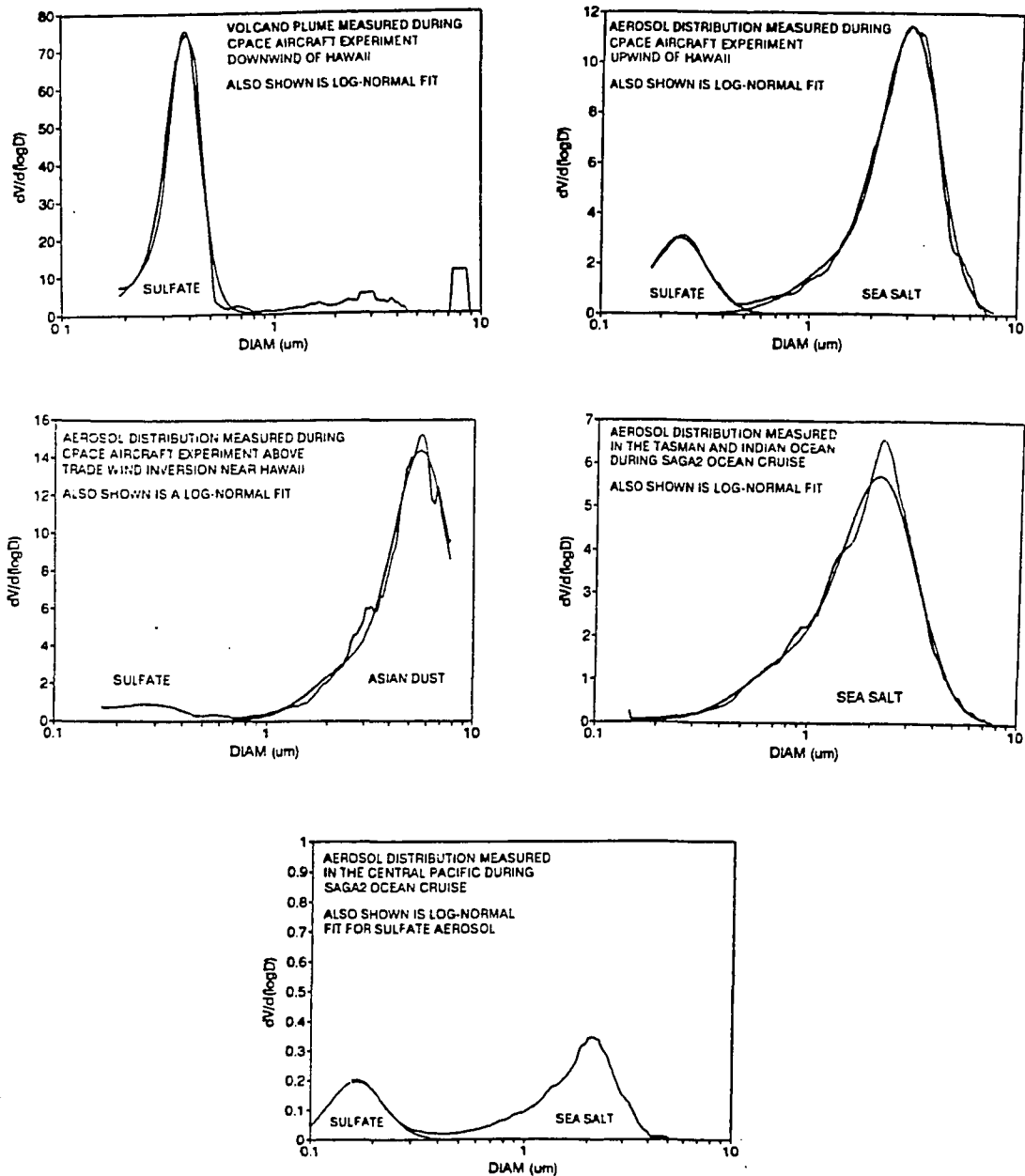


Figure 1.2. Aerosol distributions measured with a laser optical counter in various regions of the remote marine atmosphere. These cases illustrate the range of variability (note the scale changes). Also shown are several log normal fits to the measured size distributions.

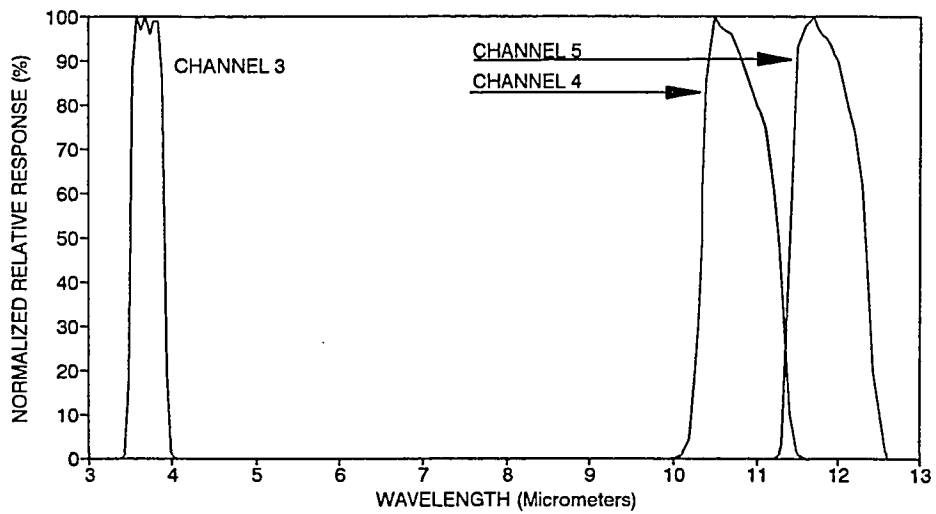
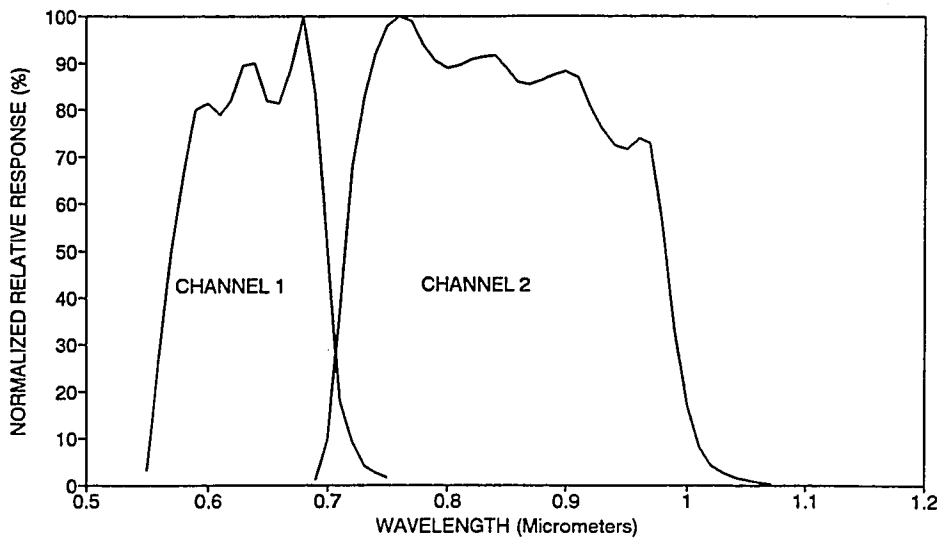


Figure 1.3. Wavelength response for the various channels of the AVHRR satellite. The channels used in the present study include, channel 1 in the visible, channel 2 in the near IR and channels 4 and 5 in the IR.

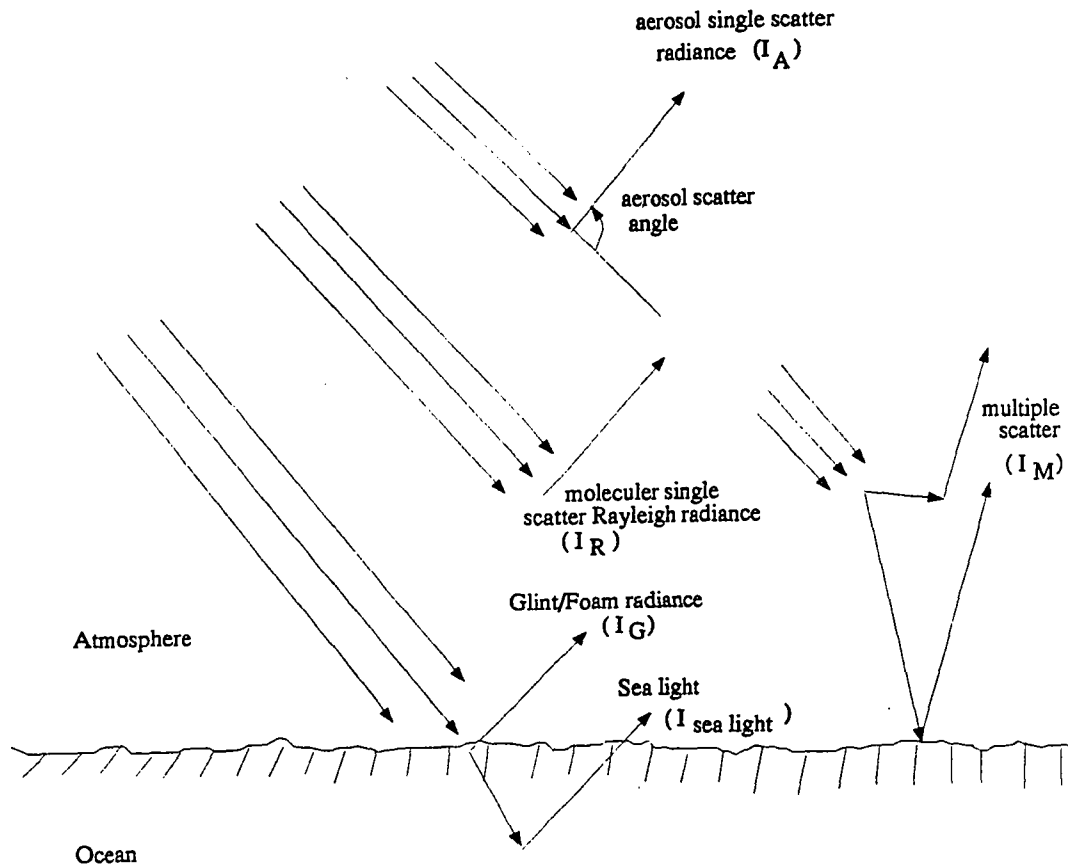


Figure 2.1. Shown here are various forms of scattering including aerosol and Rayleigh single scattering, scattering from the ocean surface (either glint or foam), sea light and various types of multiple scattering. The notation used in the text for the aerosol scattering angle is also shown here.

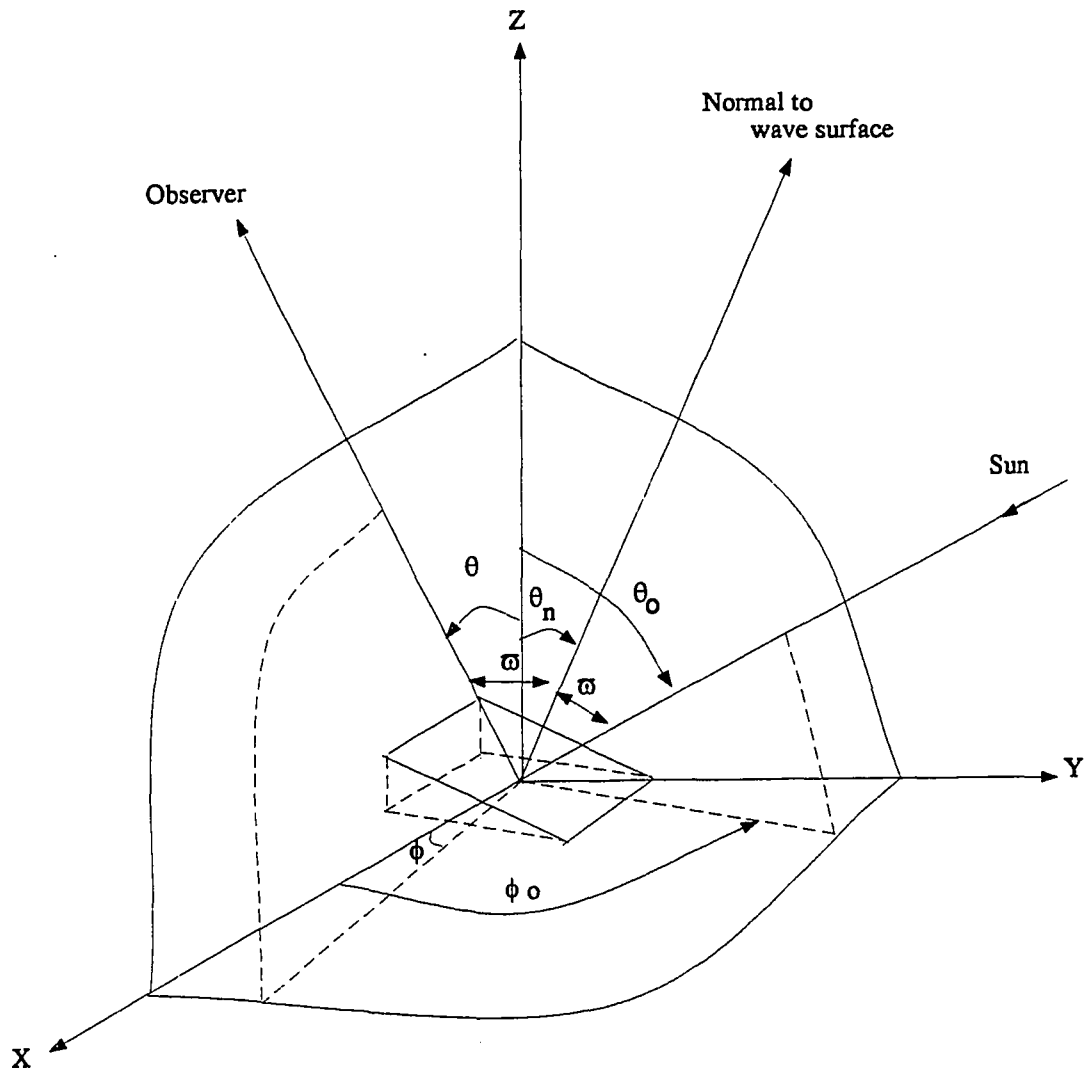


Figure 2.2. Ocean surface scattering geometry. Shown here is the face of a wavelet which is tilted with respect to the zenith.

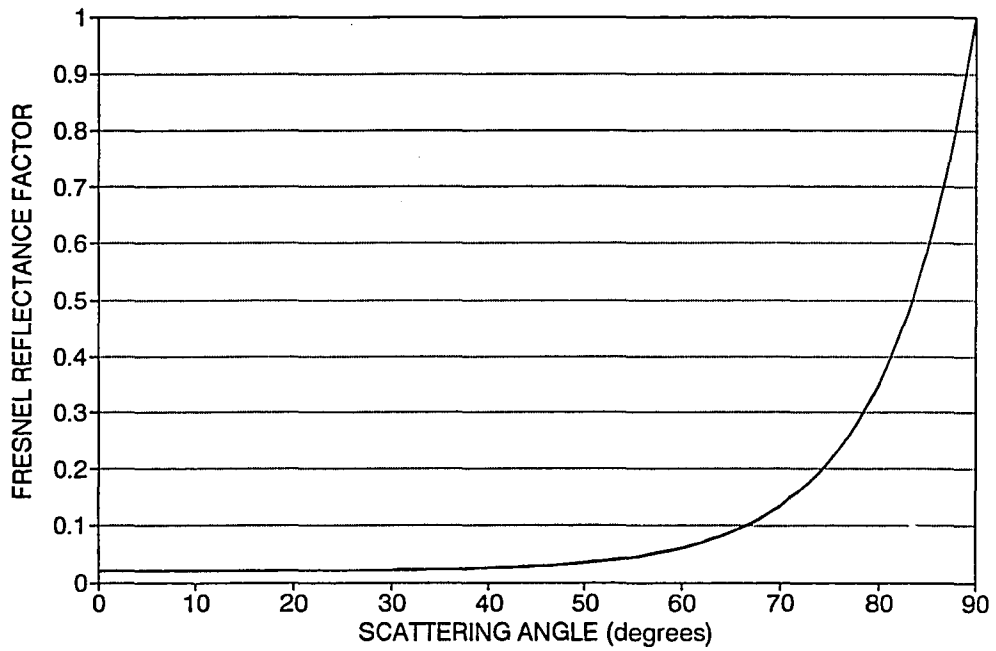


Figure 2.3. Fresnel reflection coefficients for various scattering angles. In this figure the scattering angle is taken from the incident light to the scattered light. This is different from the aerosol scattering angle (shown in figure 2.1) where the scattering angle is taken from the forward direction to the scattered light.

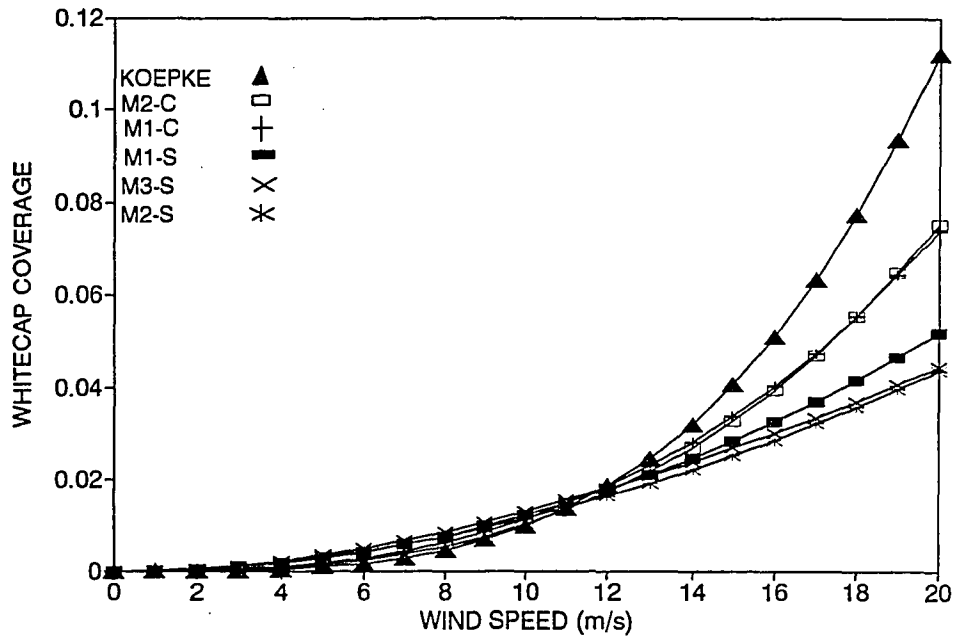


Figure 2.4. Fractional ocean whitecap coverage based on O'Muircheartaigh and Monahan (1986) and Koepke (1985). The O'Muircheartaigh and Monahan values are presented with the prefix M. The C and S refer to two different data sets and the numbers 1, 2 and 3 refer to different statistical methods applied to the data sets. For the present study the M1-C case was employed.

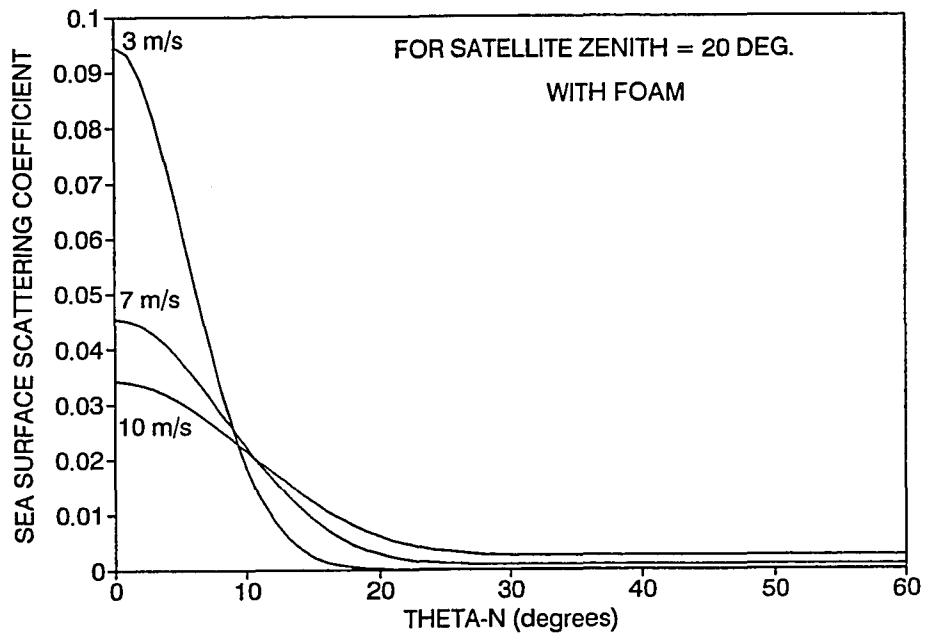


Figure 2.5. Ocean surface scattering coefficient as a function of θ_n where θ_n is the angle from the zenith to the direction normal to the face of ocean surface wave which is tilted so that it produced sun glint for the satellite (see figure 2.2.). At larger θ_n angles the glint term drops off and the ocean reflection becomes isotropic and depends only on whitecap coverage assumed.

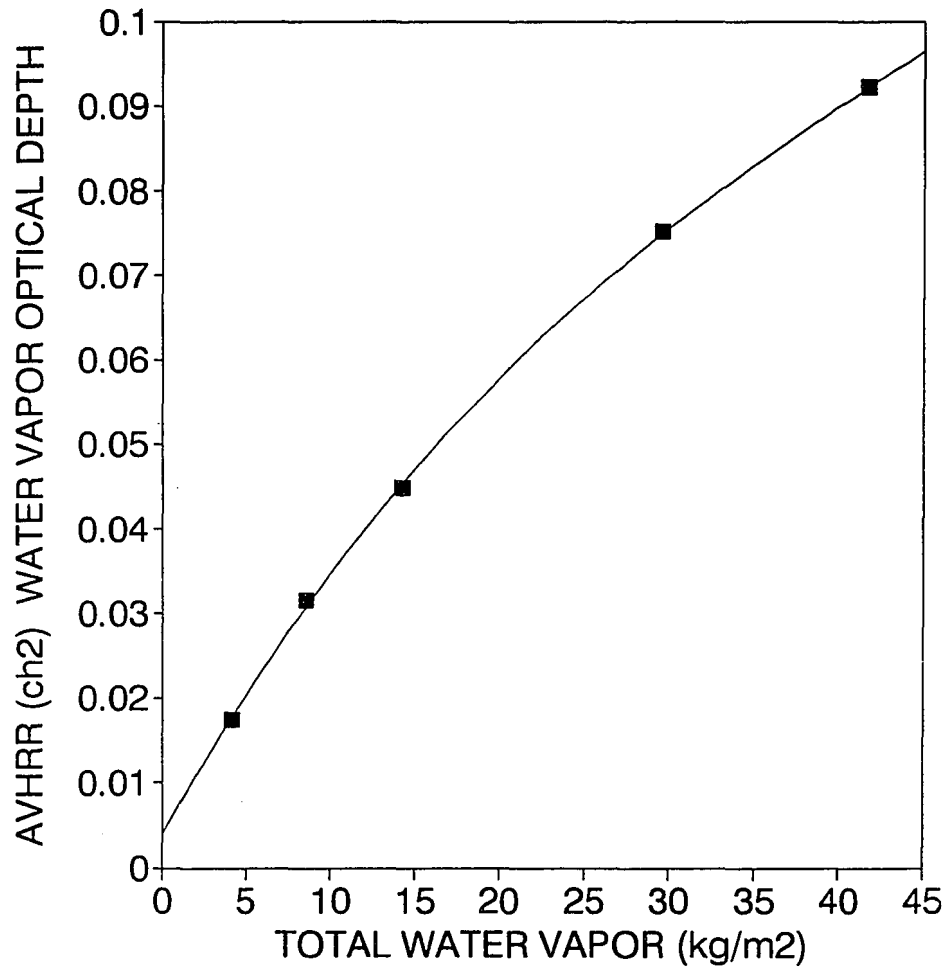


Figure 2.6. AVHRR channel 2 water vapor absorption optical depth as a function of total atmospheric water vapor. Values are based on the work of Sanders and Edwards (1989) with Lowtrans7 model.

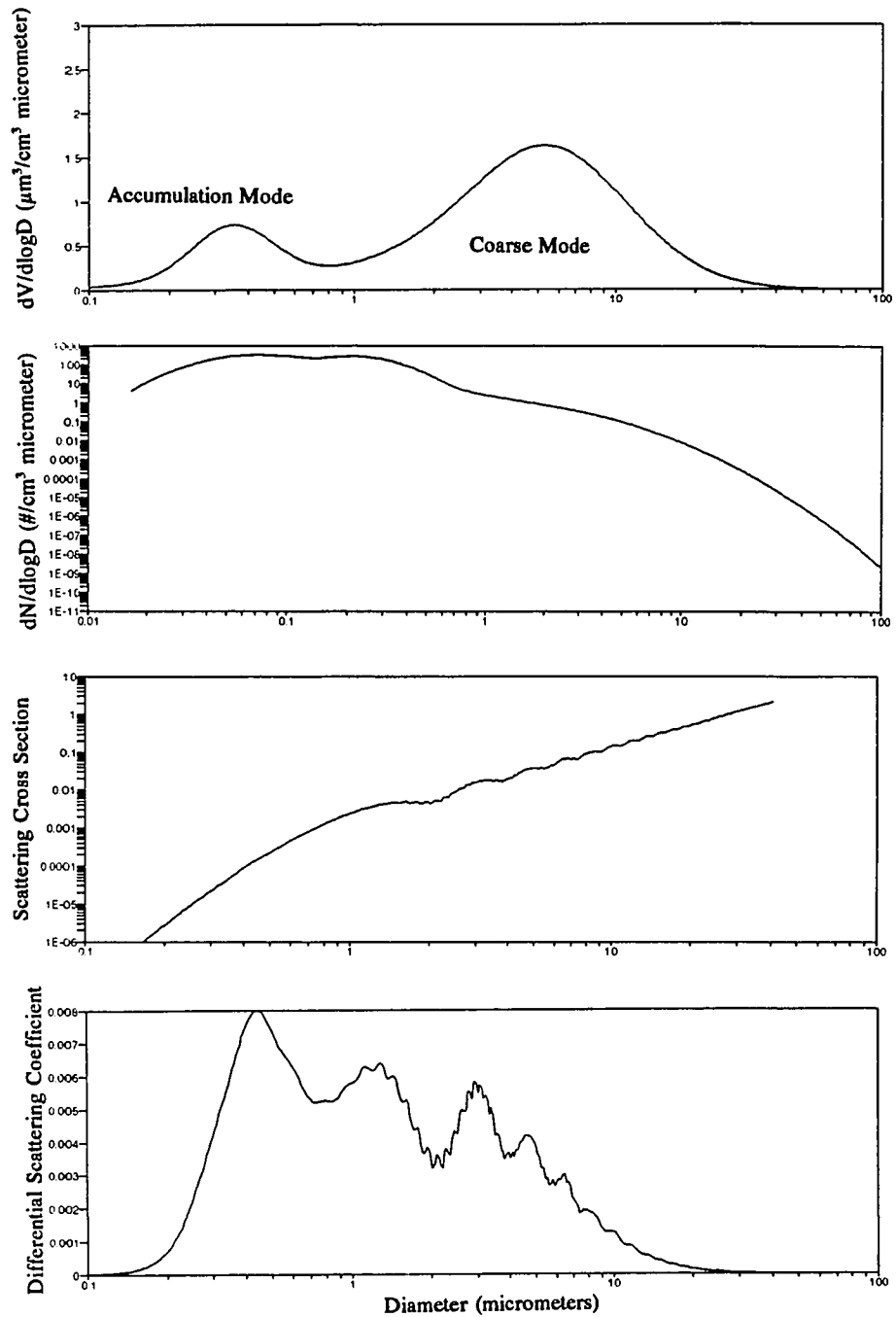


Figure 2.7. Example of: aerosol volume distribution (top panel), aerosol number distribution (next panel), aerosol scattering coefficient (next panel) and differential scattering coefficient (bottom panel). Calculations were done for a wavelength of 0.63 μm .

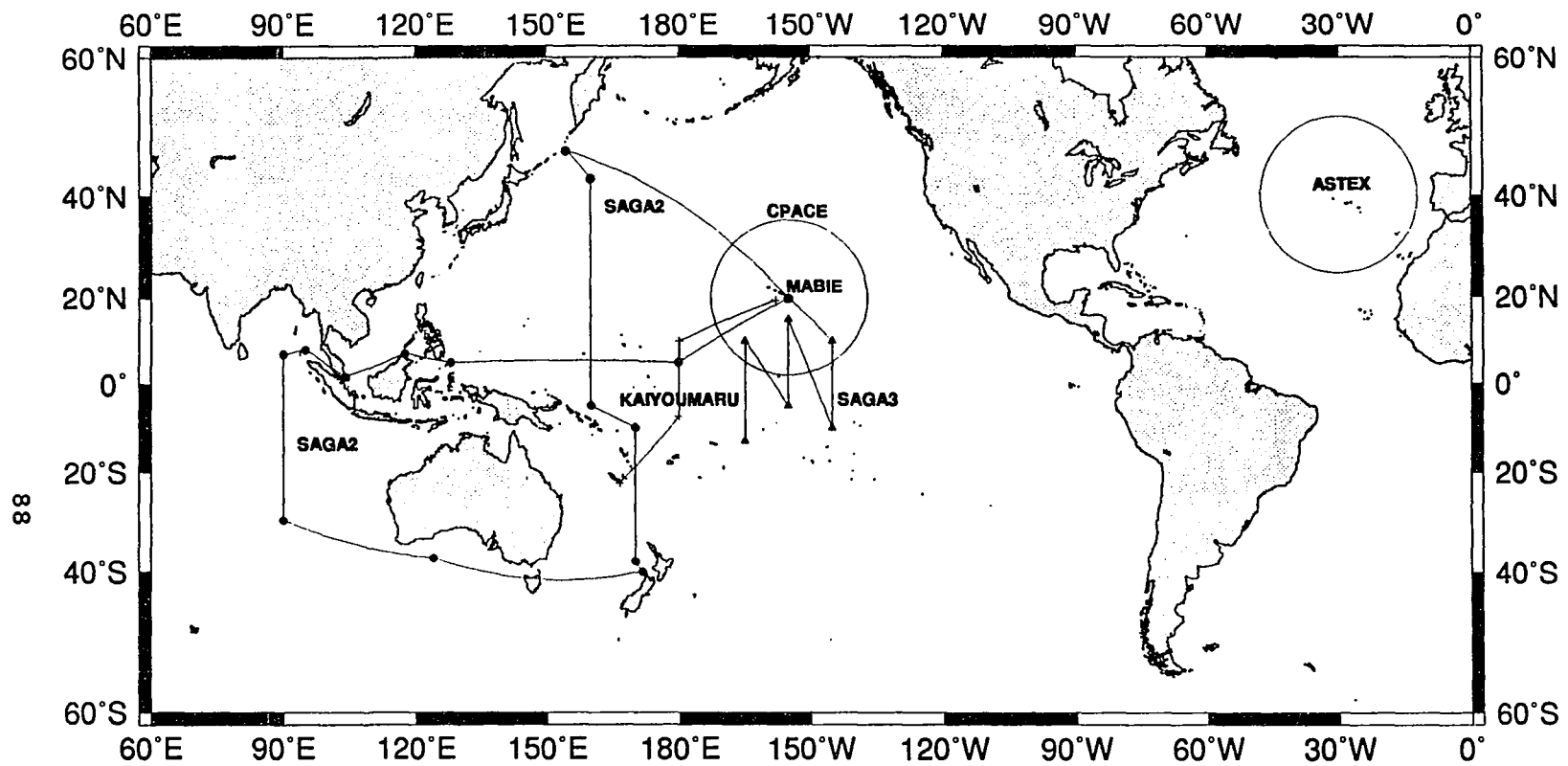


Figure 3.1. Map showing the location of various aerosol measurement experiments. Ship experiments are shown as lines. Aircraft experiments are shown as circles.

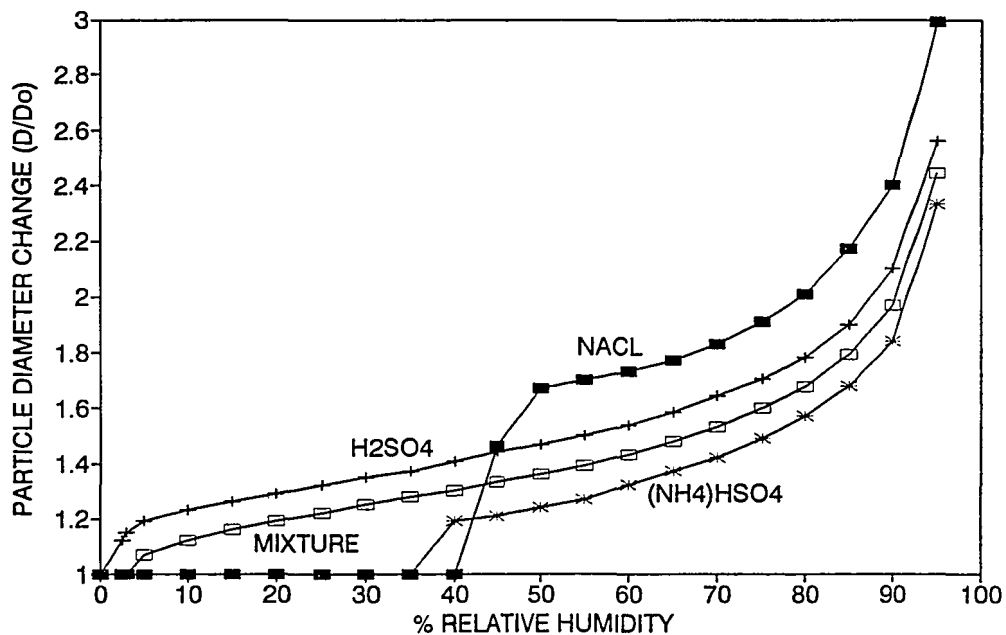


Figure 3.2. Equilibrium aerosol diameters as a function of relative humidity for various aerosol compositions. The values for NaCl, H₂SO₄ and (NH₄)SO₄ are based on the work of Tang et al. The line shown for the mixture is based on laboratory experiments with various molar ratios of (NH₄)/(SO₄) ranging from 0 to 1. Aerosol volatility tests performed during the various experiments suggest remote marine aerosol molar ratios are typically in this range.

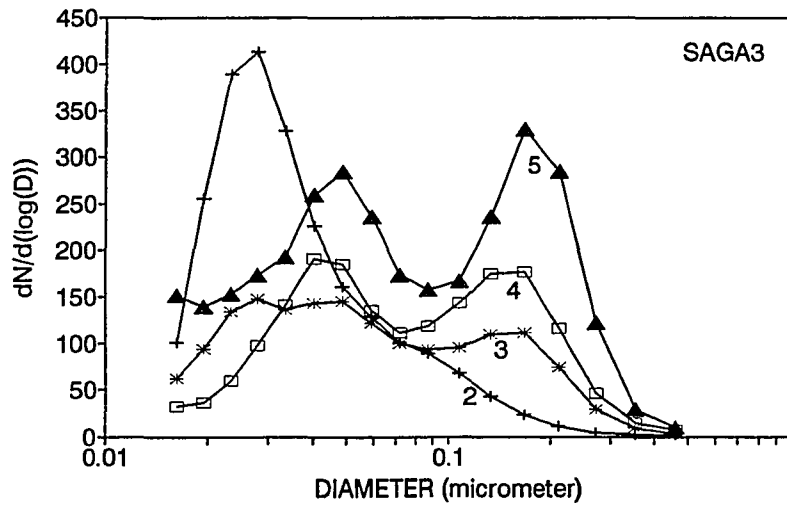


Figure 3.3a. Average dry aerosol size distributions measured with the differential mobility analyzer during the SAGA3 ship experiment. These various cases came from grouping each aerosol distribution according to its dry aerosol volume (ie. mass) and then averaging each group of distributions. The aerosol group is shown next to each distribution.

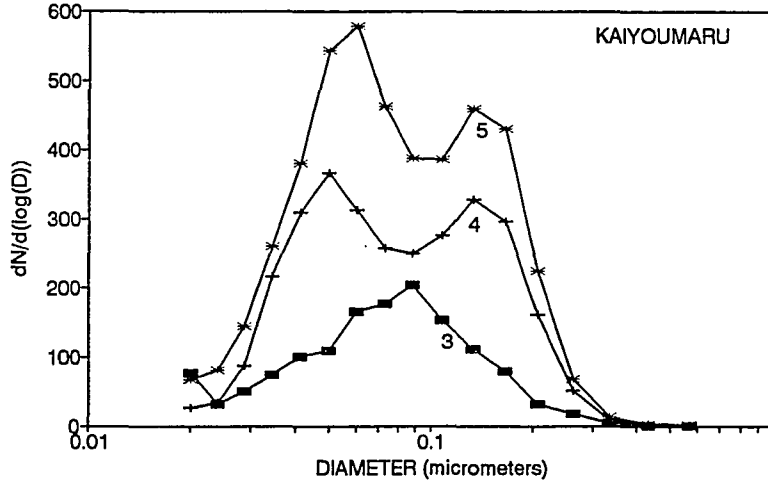


Figure 3.3b. Average dry aerosol size distributions measured during the Kaiyoumaru ship experiment. The method of grouping and averaging each measured aerosol size distribution is similar to figure 3.3a.

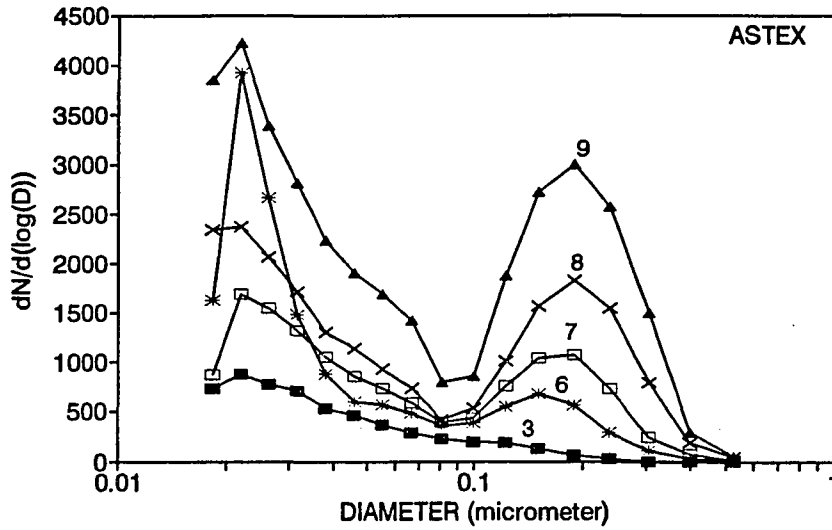


Figure 3.4a. Average dry aerosol size distributions measured during the Astex experiment. The method of grouping and averaging is the same as was used in figures 3.3a and 3.3b.

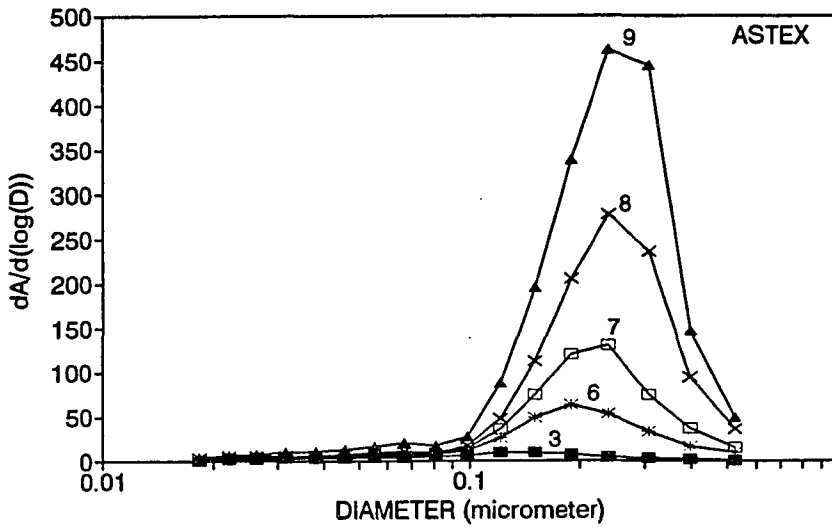


Figure 3.4b. Same dry aerosol averages as shown in figure 3.4a but now shown as the aerosol area distributions.

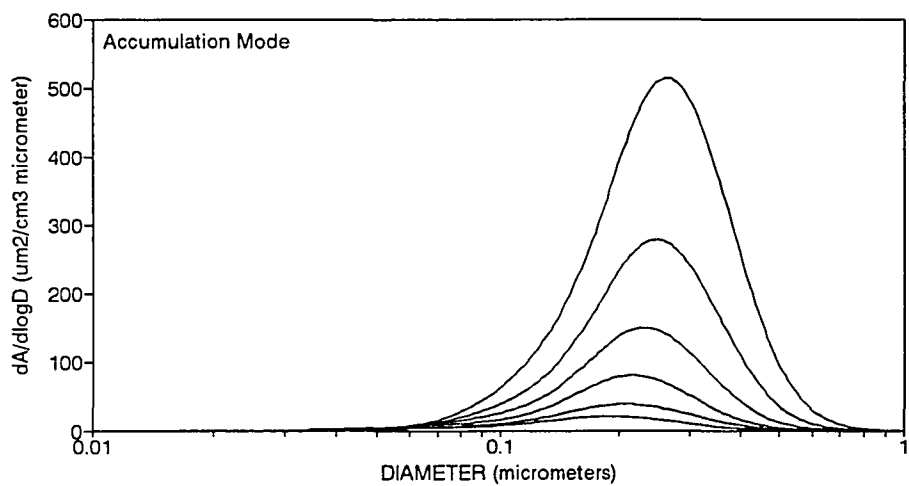
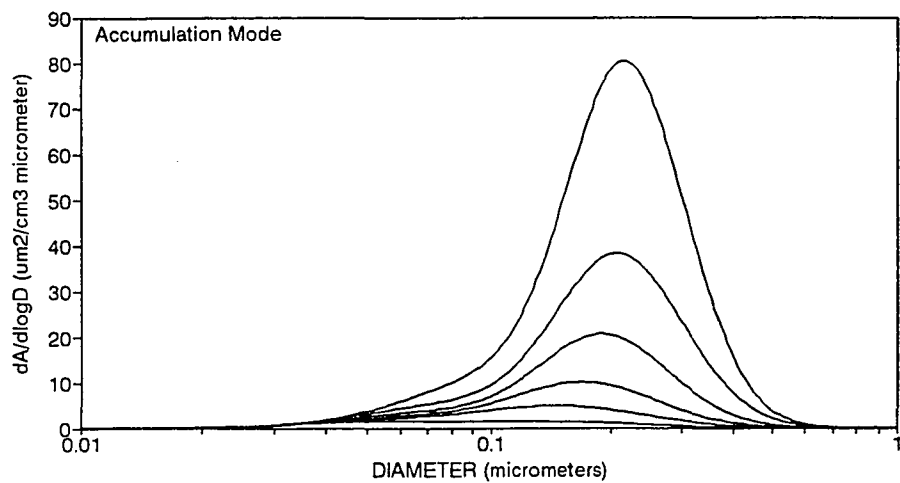


Figure 3.5. The dry sulfate aerosol model developed from insitu aerosol measurements. The top panel displays average 1 through 6. The bottom panel displays average 4 through 9. The lognormal parameters for these curves are given in table 1.

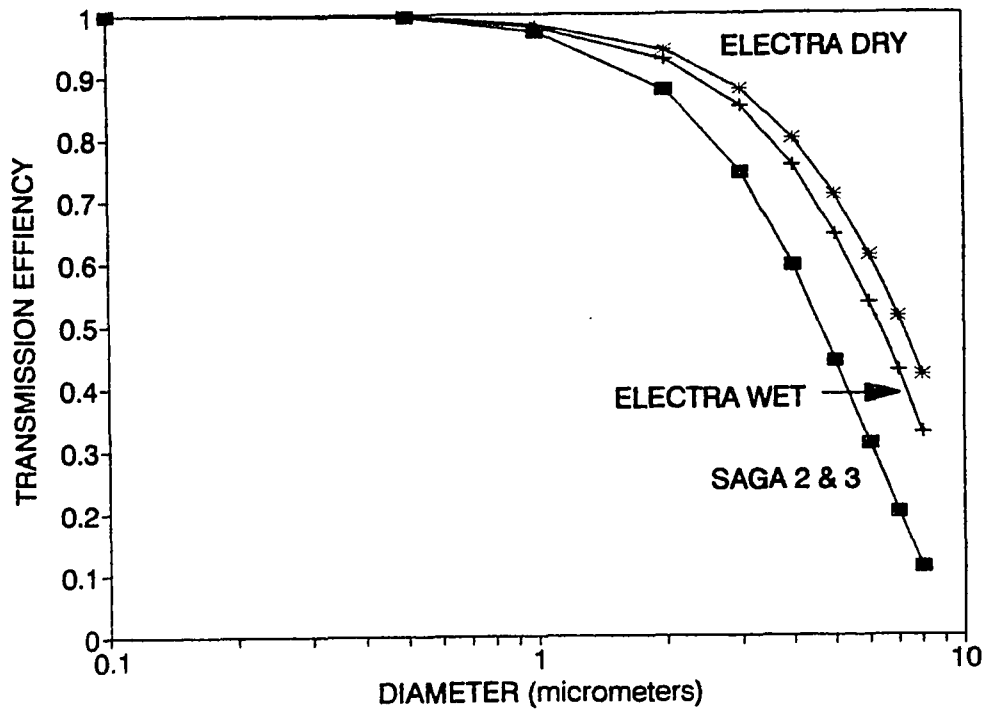


Figure 3.6. The estimated aerosol transmission losses in the sampling system. The aircraft losses (ELECTRA) are shown for low and high relative humidity cases such as is found above and below the trade wind inversion. Also shown are the transmission losses for the SAGA 2&3 ship experiment.

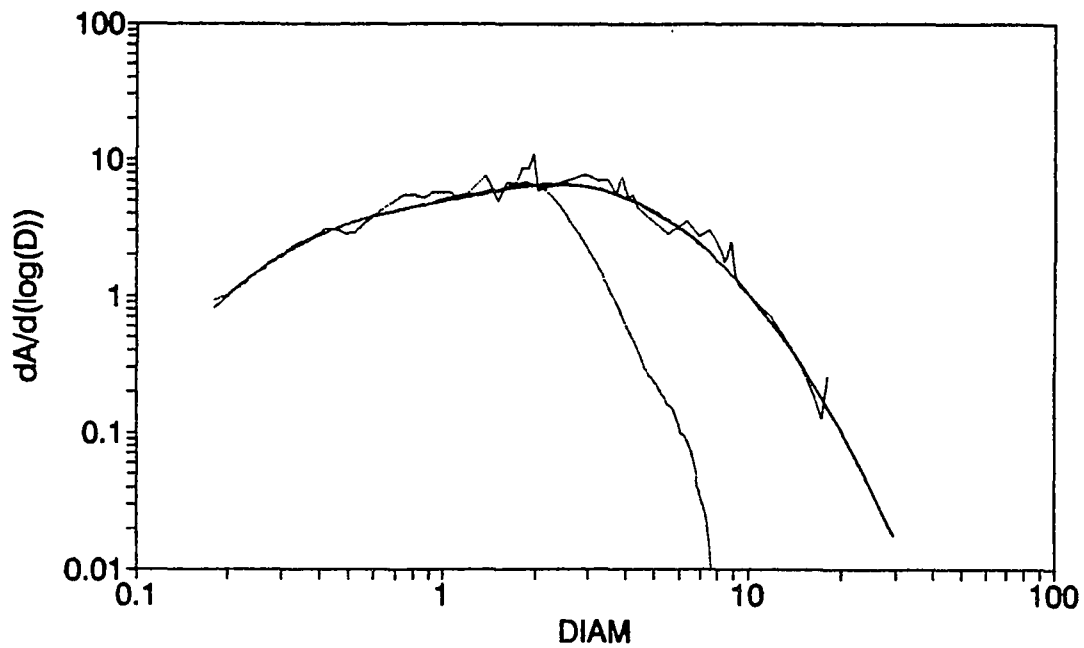


Figure 3.7. Salt aerosol comparison for the optical particle counter and the Woodcock glass slide impactor. The Woodcock measurements range from approximately 0.9 to 20.0 μm while the OPC measurements range from 0.17 to 7.5 μm diameter. Also shown is a curve fit for the OPC distribution at the smaller sizes and the impactor distribution at the larger sizes.

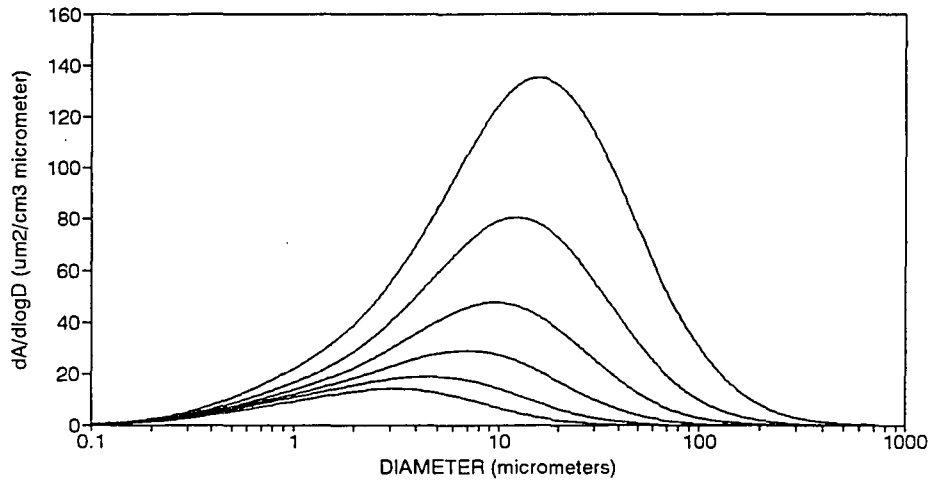
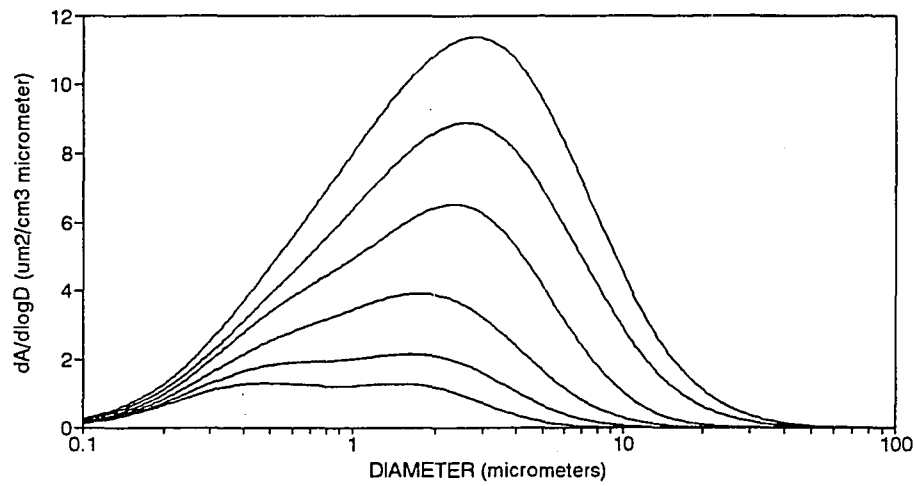


Figure 3.8. The dry salt aerosol model developed from the combination of OPC and Woodcock distributions. The curves in the upper figure correspond to wind beufort scales of 1 to 6 while the bottom figure curves correspond to scales of 7 to 12.

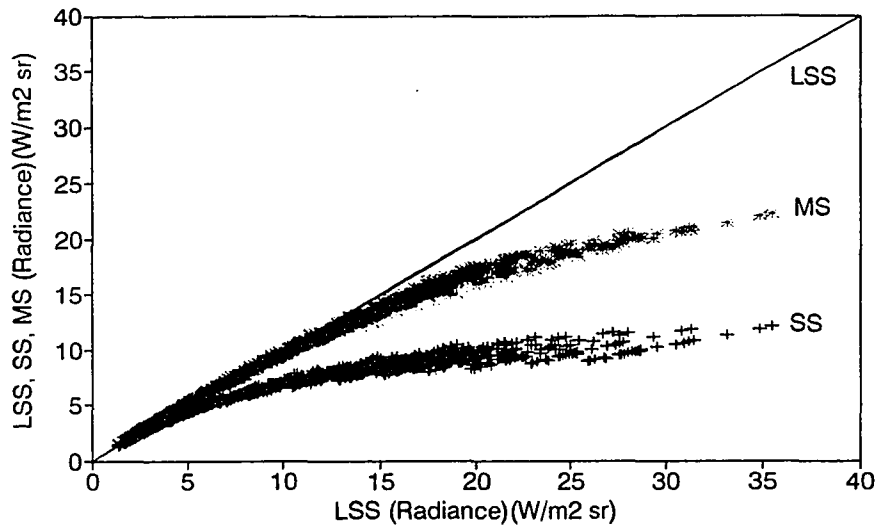


Figure 4.1 A comparison between aerosol single scatter (SS), aerosol linearized single scatter (LSS) and aerosol multiple scatter from a discrete ordinates program (MS) plotted versus the aerosol linearized single scatter (LSS) value. Calculations are for a large range of satellite and sun geometries and aerosol optical depths ranging from 0.03 to 0.8.

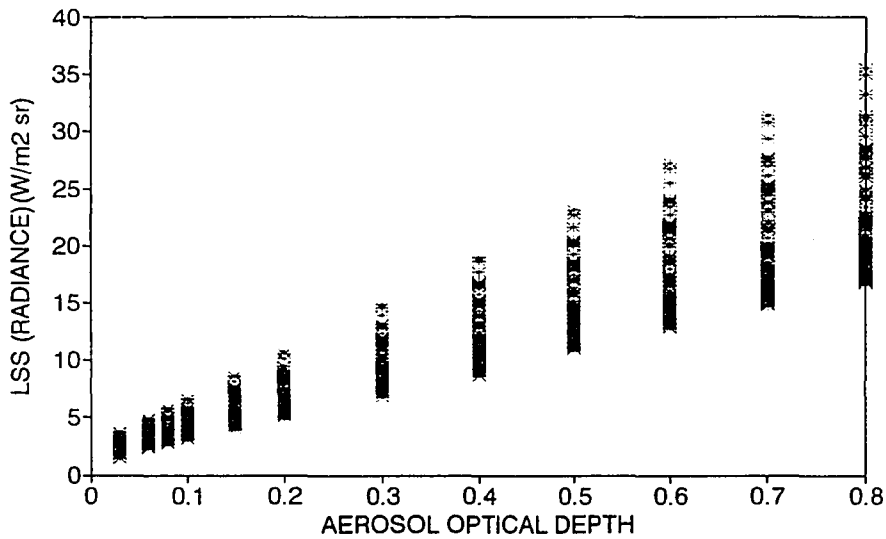


Figure 4.2. The linear single scatter from figure 4.1 plotted versus the aerosol optical depth. This figure allows for the interpretation of figure 4.1 in terms of aerosol optical depth.

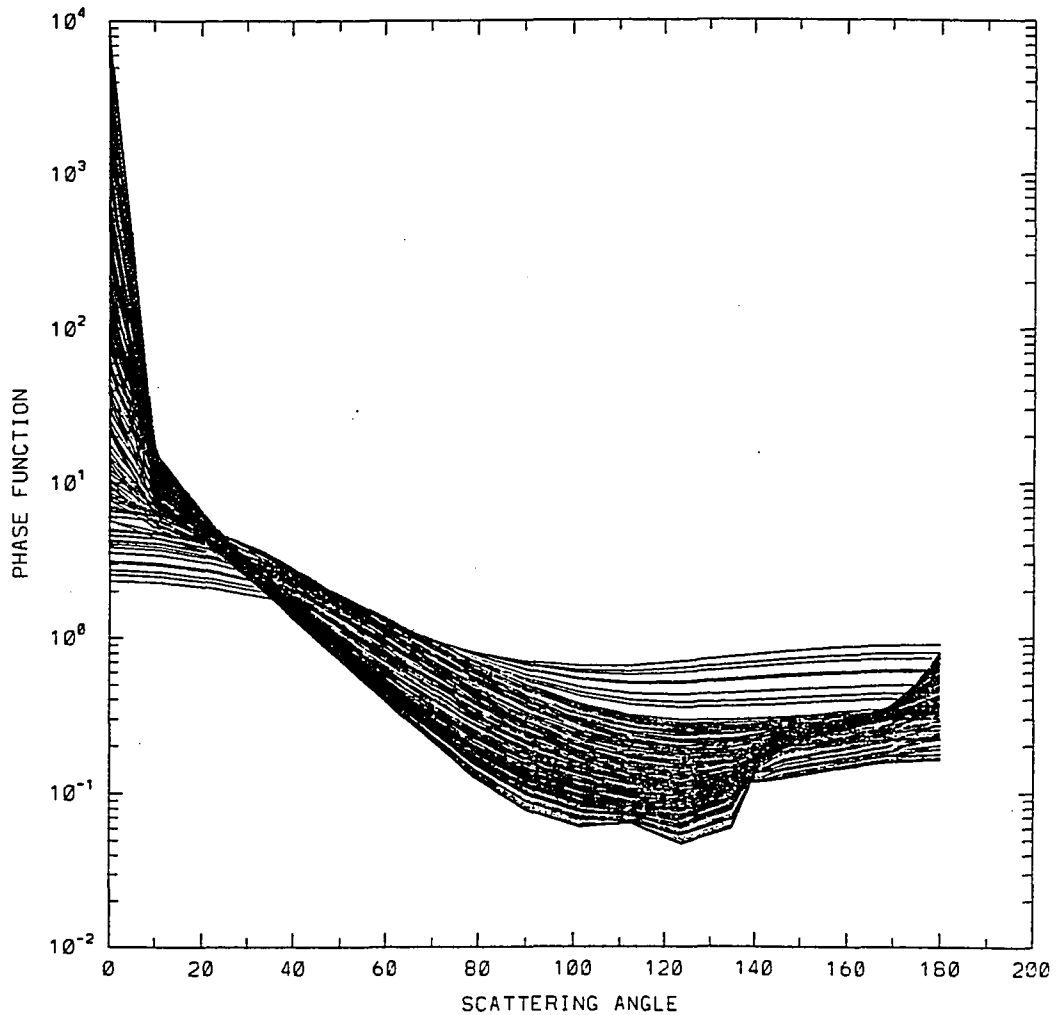


Figure 4.3. The aerosol phase functions calculated for the AVHRR satellite channel 1 from 338 different aerosol distributions. The aerosol cases were developed from various combinations of the accumulation and coarse mode and different relative humidity combinations. The phase functions were weighted for the satellite wavelength response at 5 nm intervals.

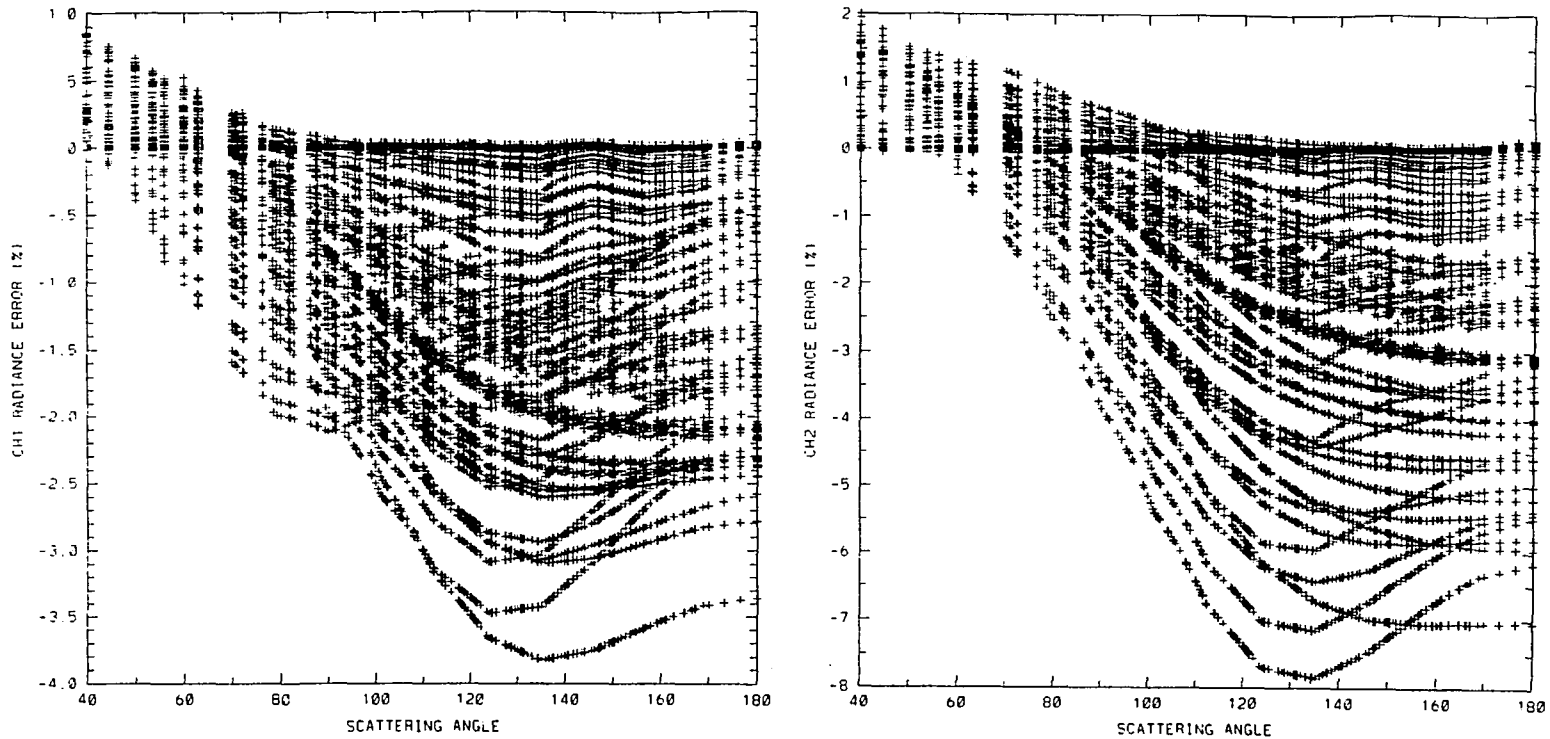


Figure 4.4. The error in equation 24, as compared to equation 23, for the 338 aerosol cases and some 700 different satellite and sun viewing geometries. Shown in the left panel is the error for AVHRR channel 1 and in the right panel is the error for channel 2.

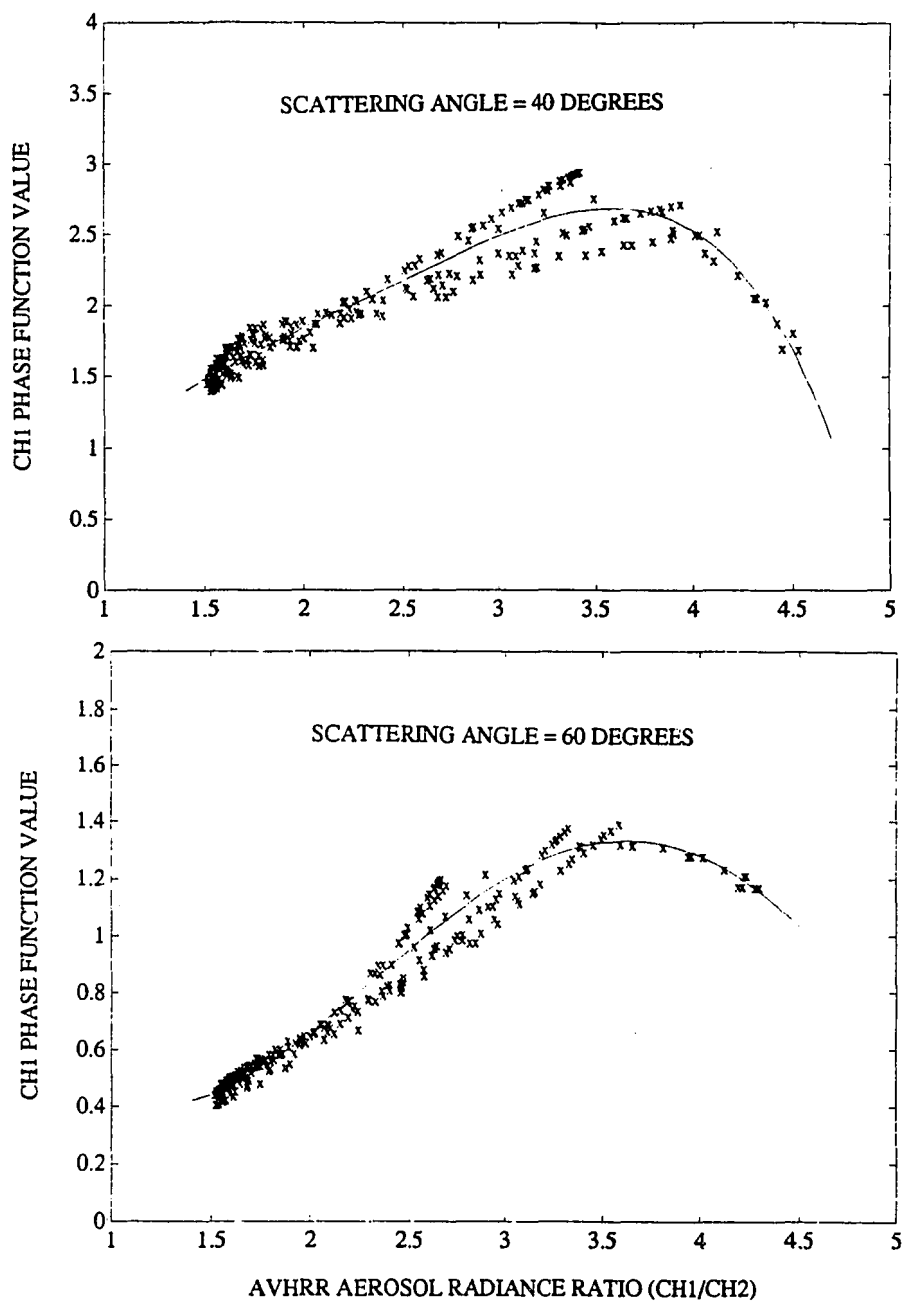


Figure 4.5. Calculated channel ch1/ch2 ratio plotted versus the channel 1 phase function value for scattering angles of 40 and 60 degrees. The various points correspond to 338 different aerosol cases. The line is from a third order fit.

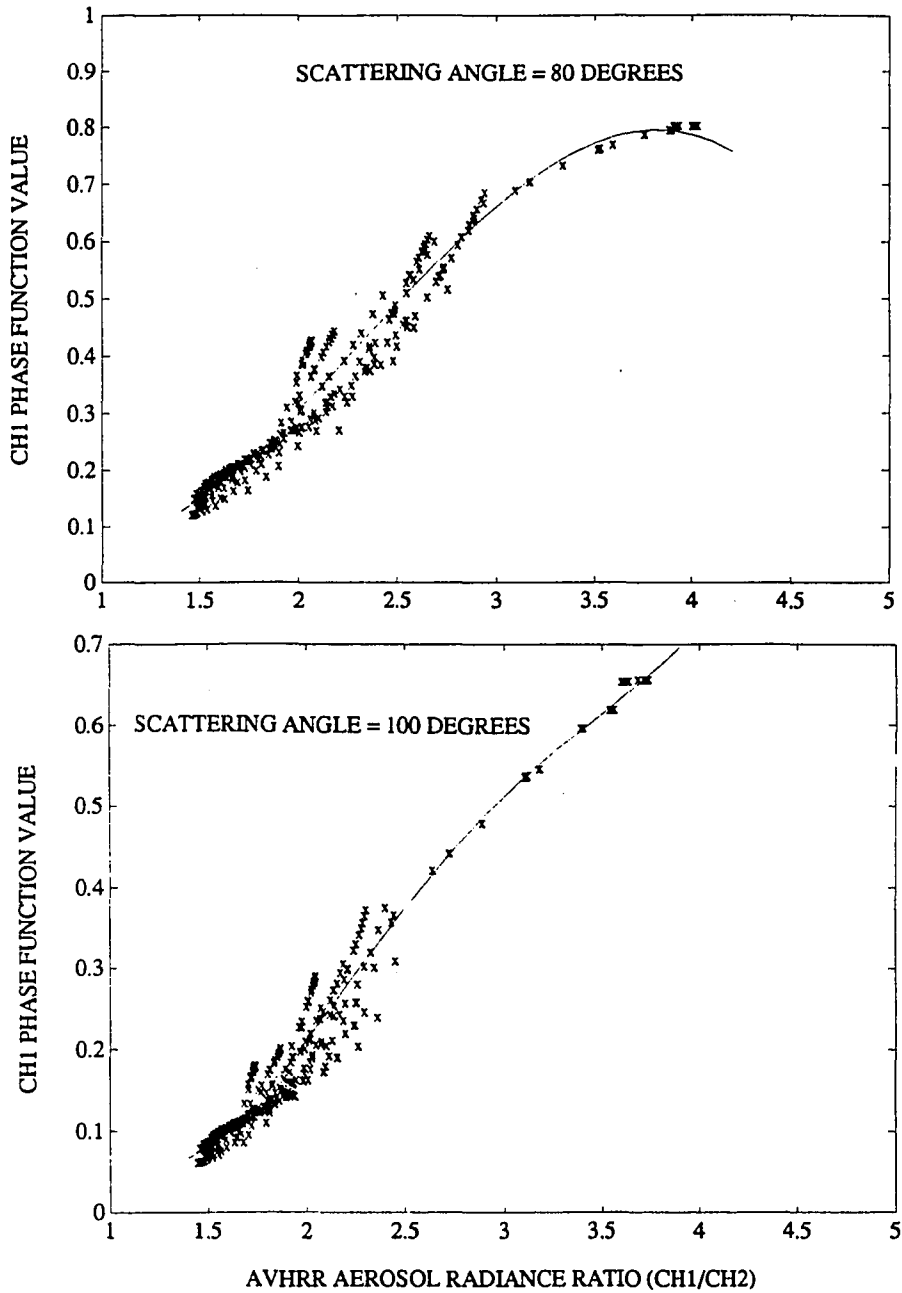


Figure 4.6. Calculated channel ch1/ch2 ratio plotted versus the channel 1 phase function value for scattering angles of 80 and 100 degrees.

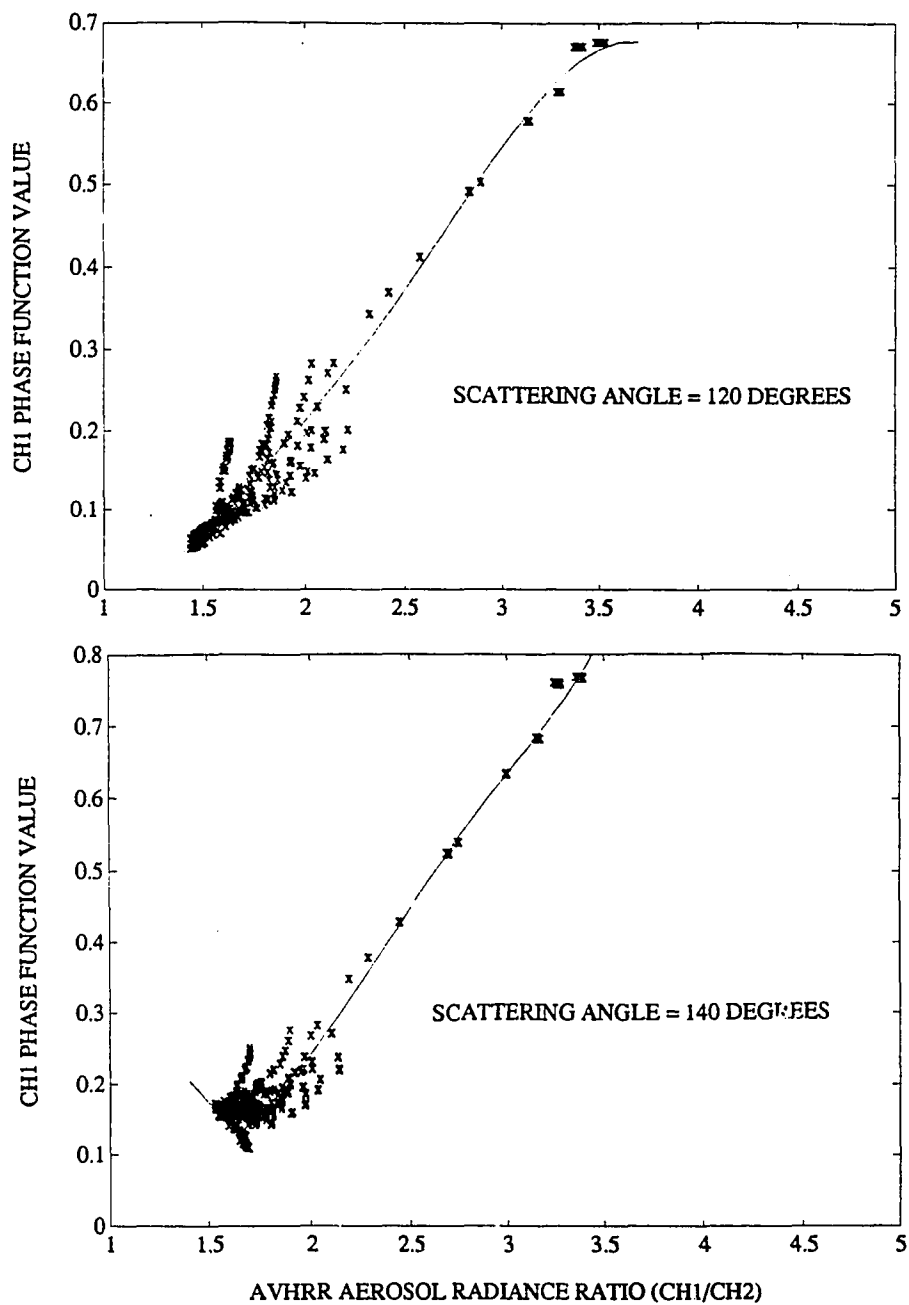


Figure 4.7. Calculated channel ch1/ch2 ratio plotted versus the channel 1 phase function value for scattering angles of 120 and 140 degrees.

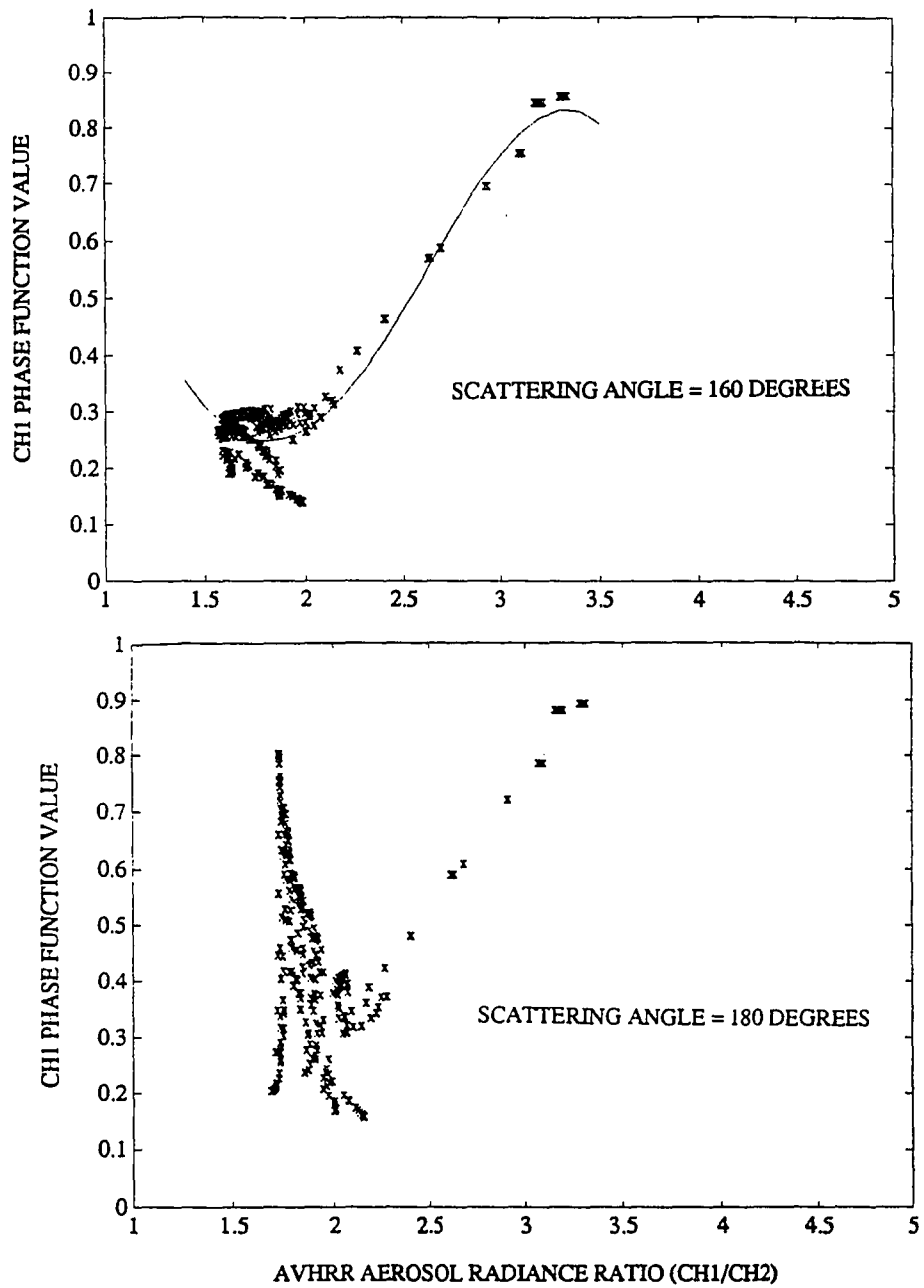


Figure 4.8. Calculated channel ch1/ch2 ratio plotted versus the channel 1 phase function value for scattering angles of 160 and 180 degrees.

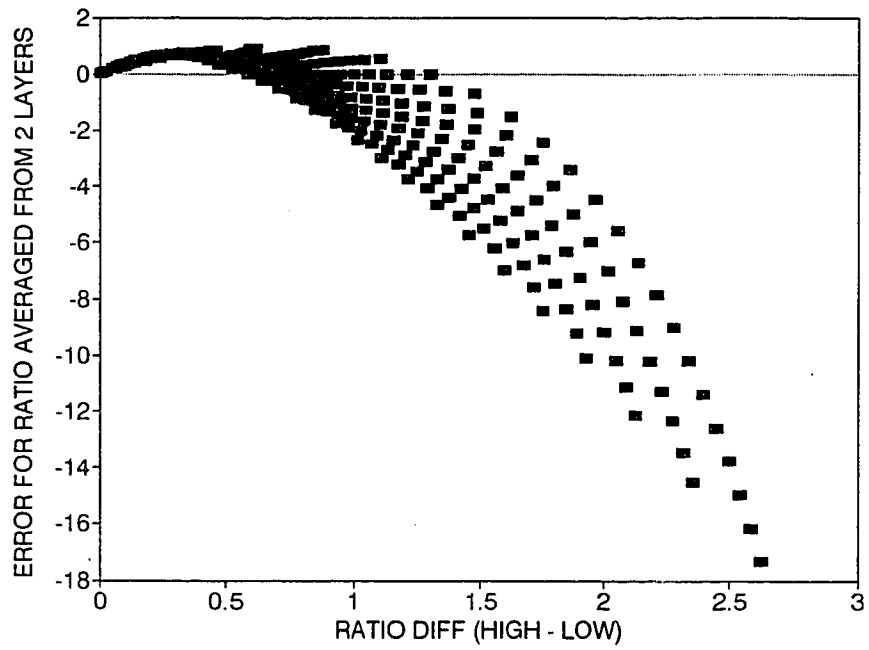


Figure 4.9. The error in the weighted average of two ratios plotted versus the magnitude of the ratio difference.

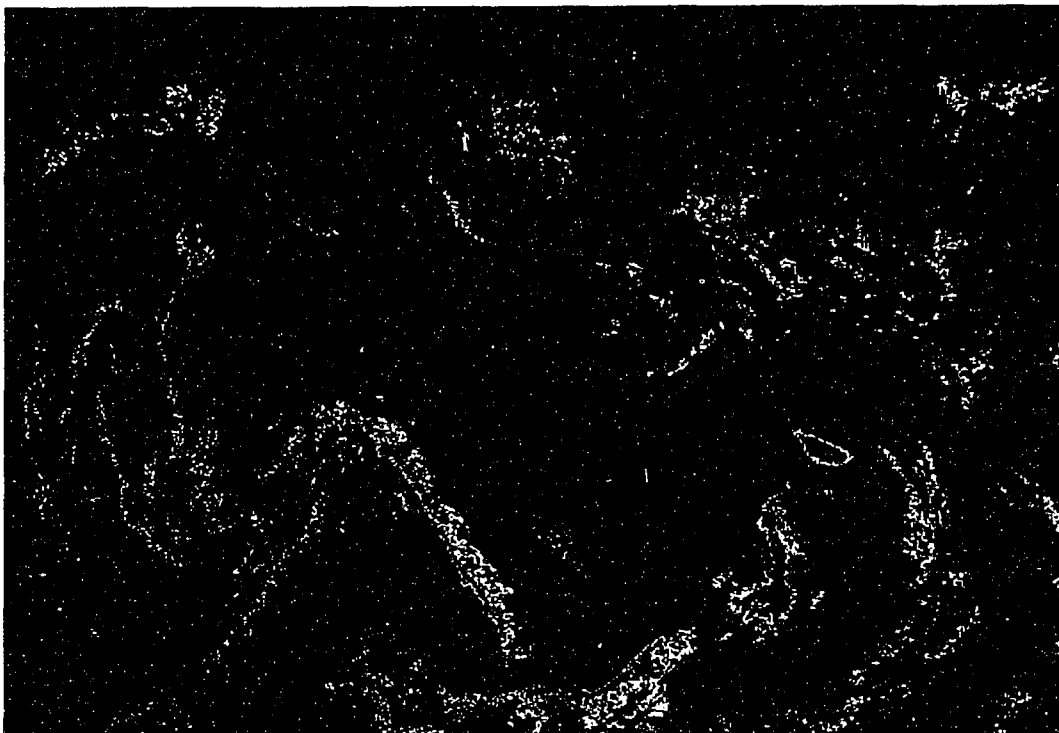


Figure 5.1. An AVHRR image (channel 1, $0.63 \mu\text{m}$) of the Hawaiian islands collected on March 26, 1993. The island of Hawaii appears in the lower right corner while the island of Kauai is in the upper left corner. In this image, the color enhancement has been set so that the brighter clouds are colored and the less bright clouds are white.

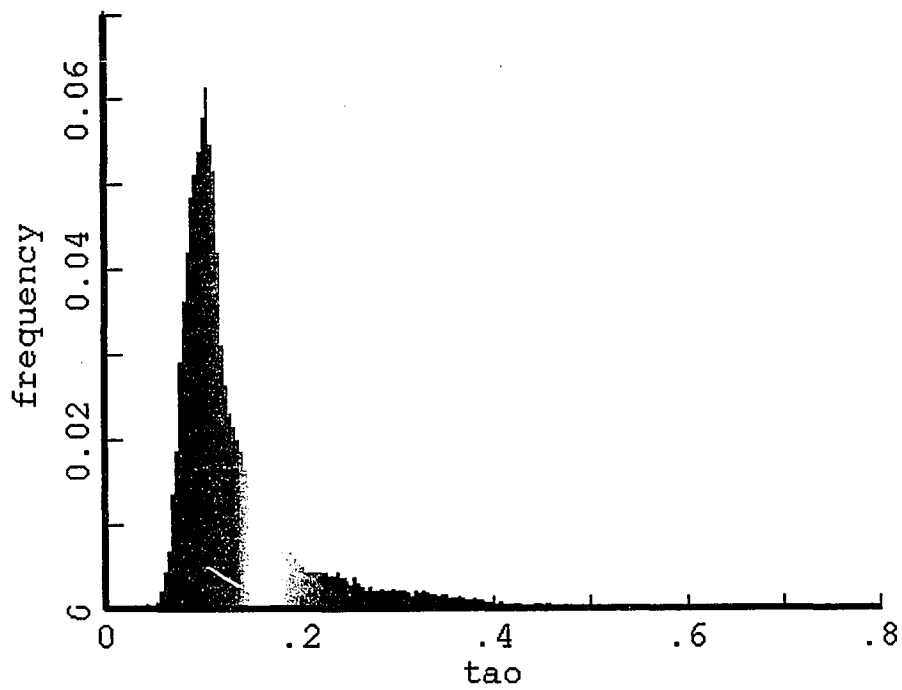
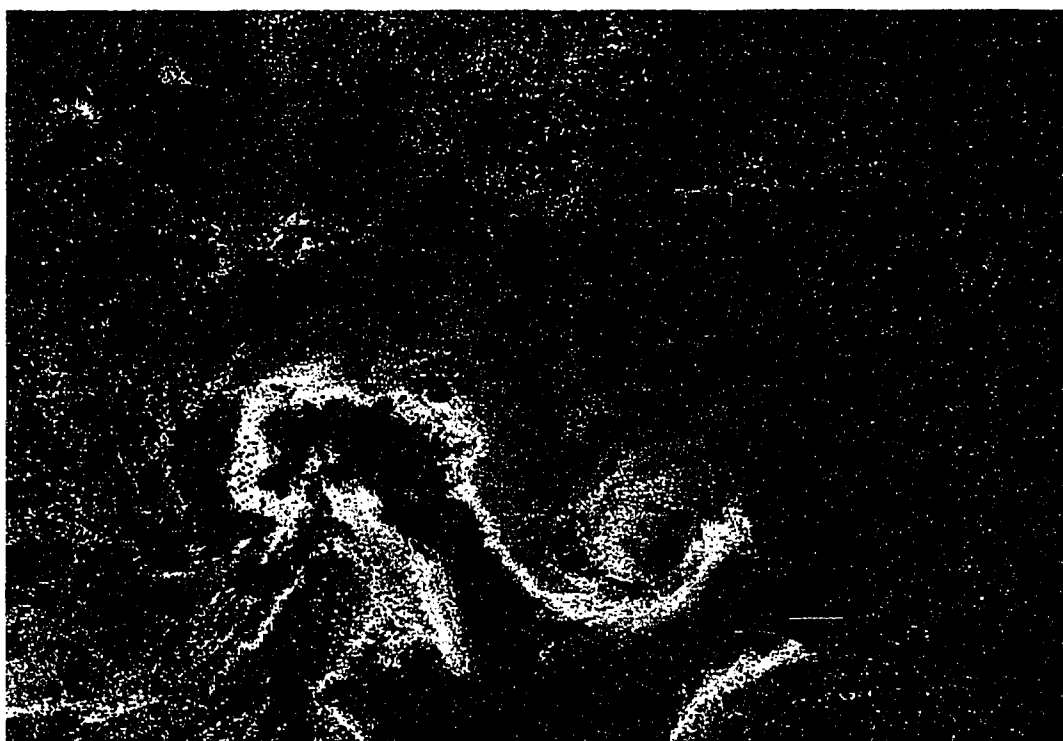


Figure 5.2. The processed aerosol optical depth from the AVHRR image shown in figure 5.1. In addition a color histogram is provided to determine the value of each color.

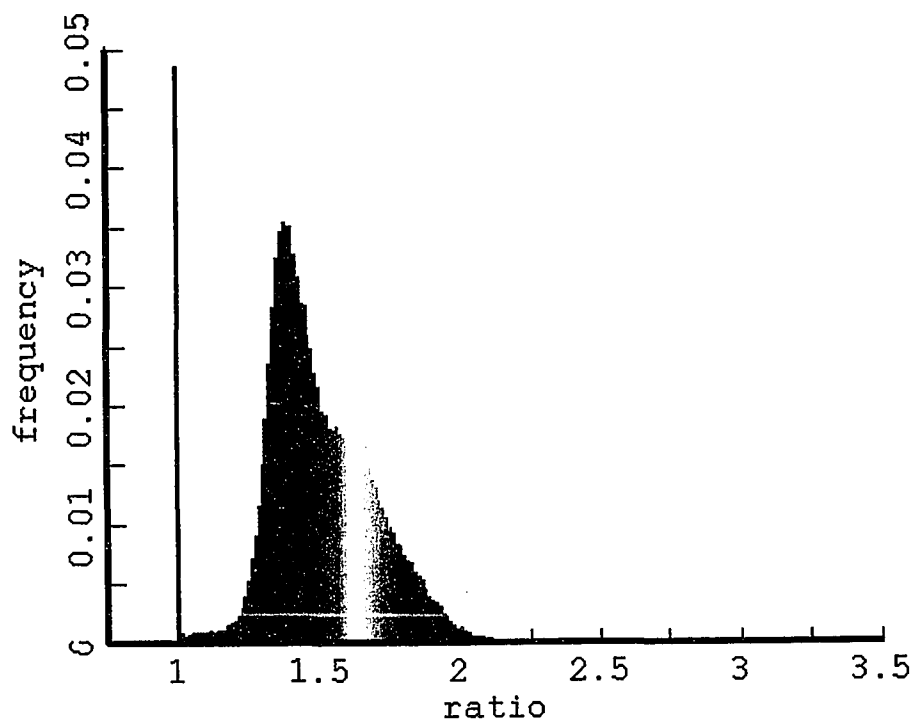
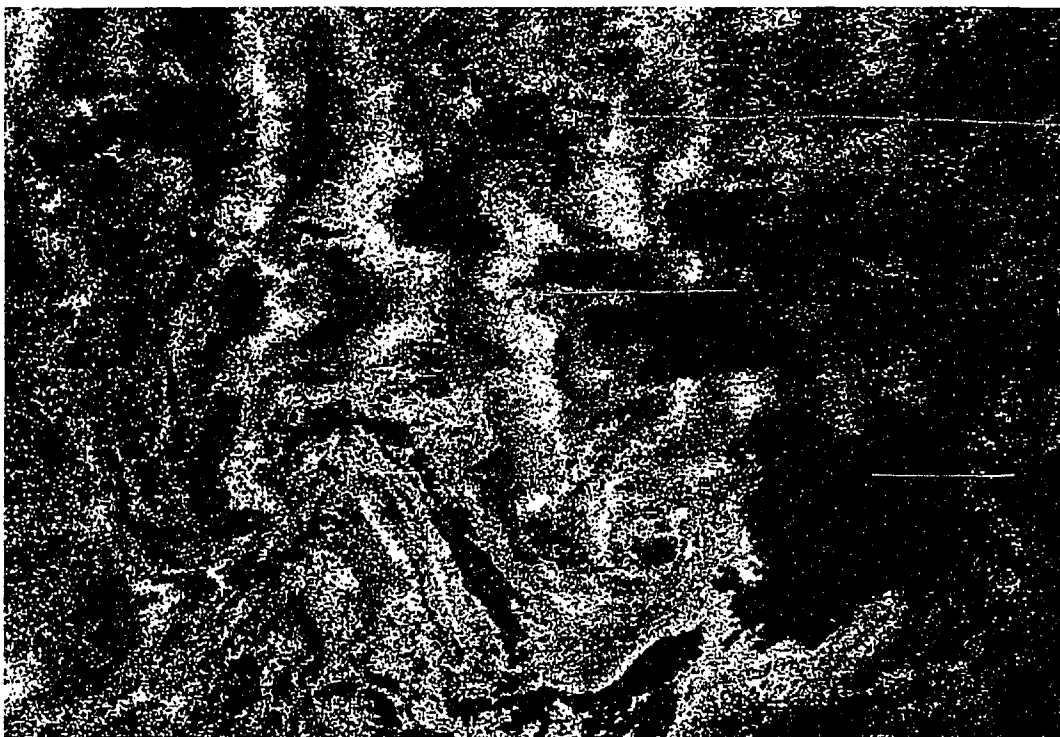


Figure 5.3. The aerosol ratio for figure 5.1 and a histogram to determine the color values.

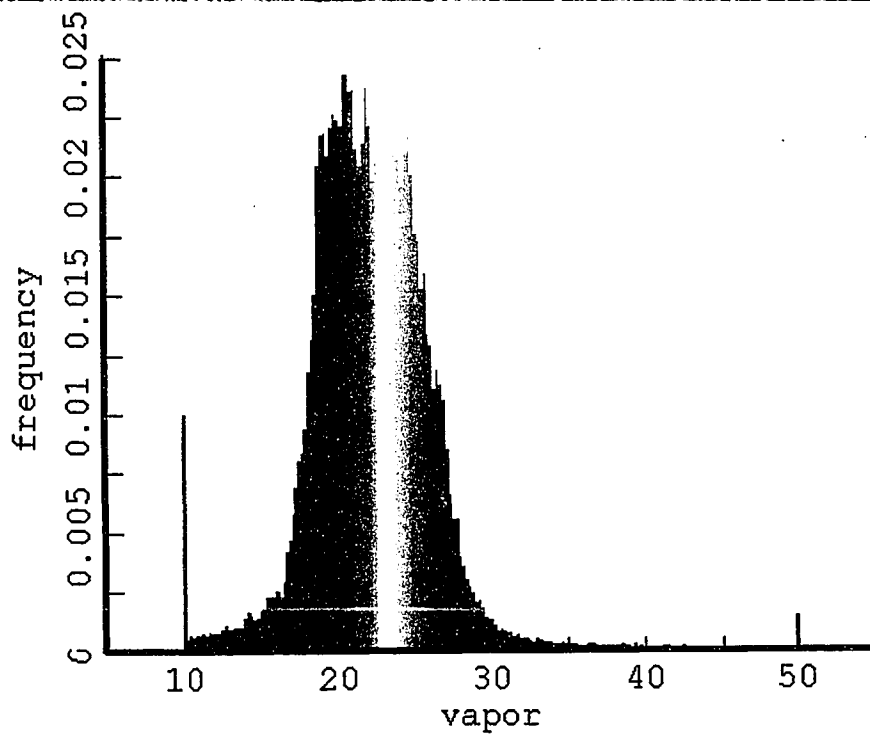
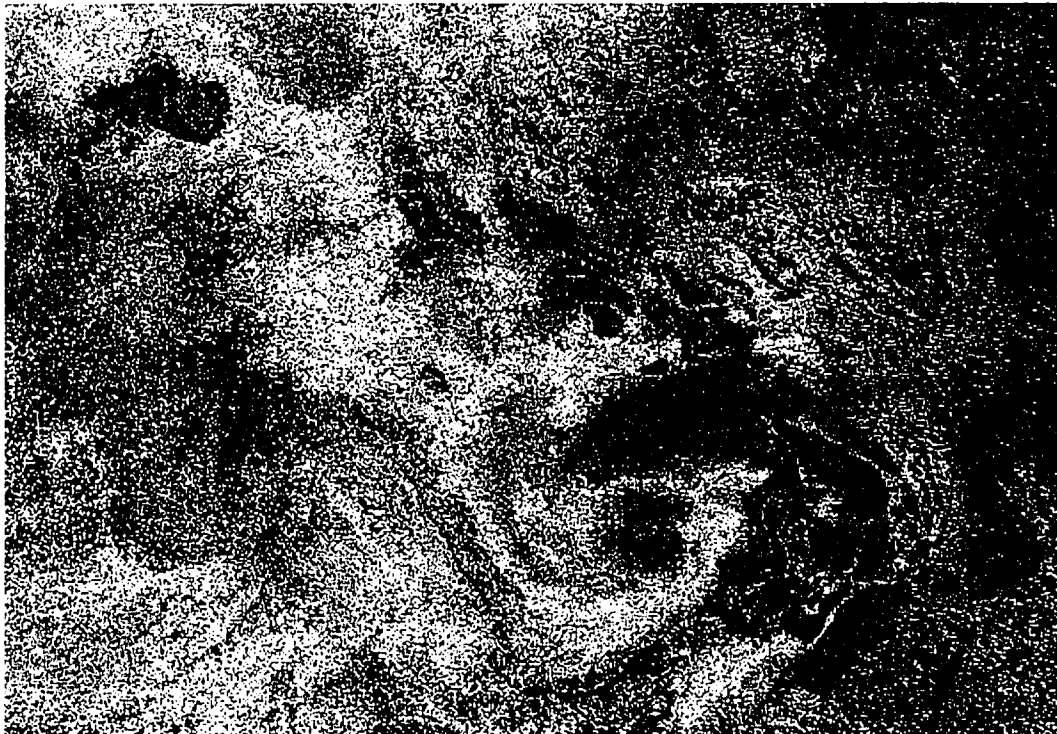


Figure 5.4. The column water vapor (kg/m^2) for figure 5.1 and the color histogram.

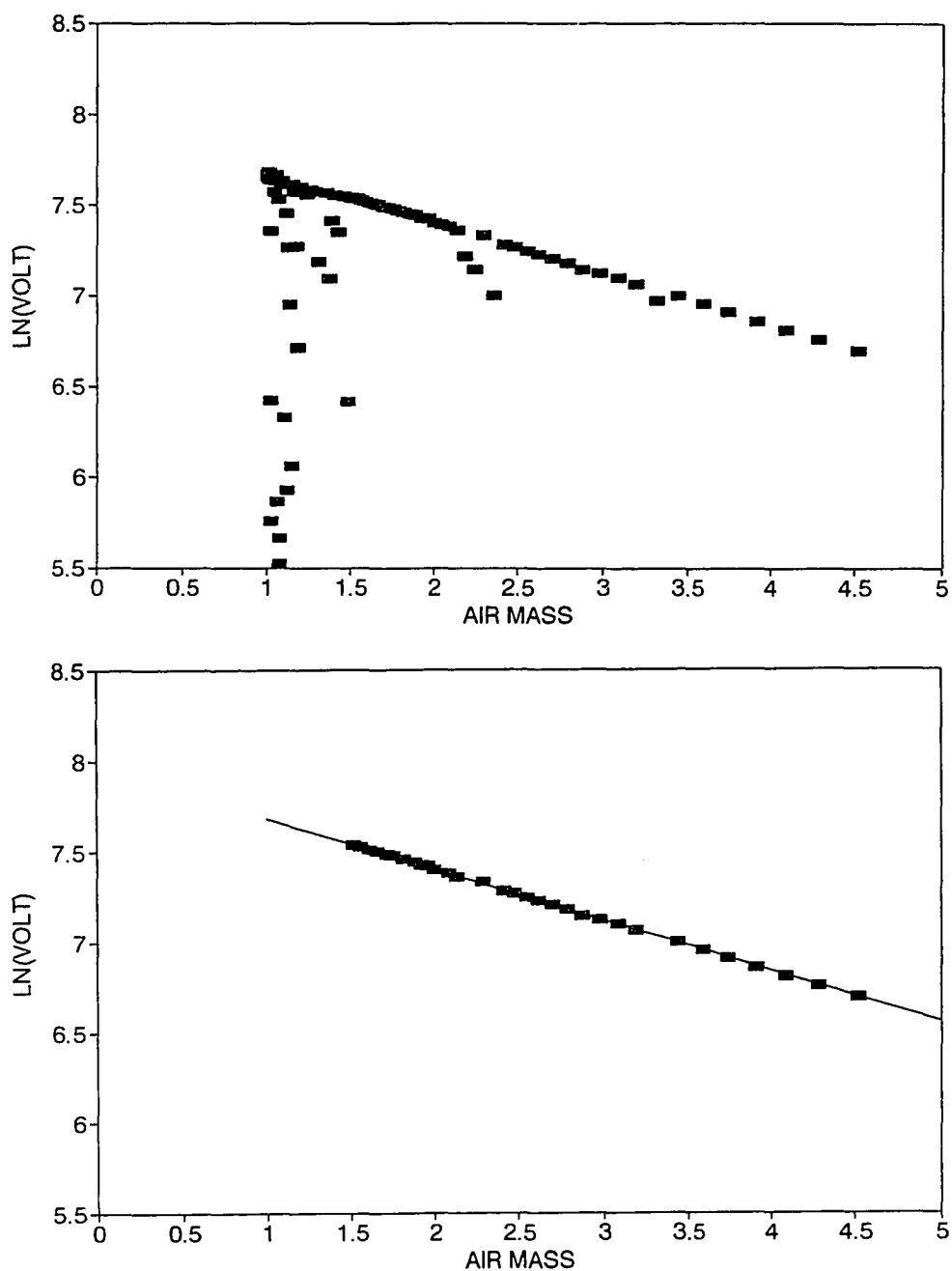


Figure 5.5. Langley plots of optical depth collected at Bellows Beach, Oahu on April 26, 1992 during the morning. The top panel is the original measurements and includes several cloudy periods. The bottom panel is the same data after cloudy periods were removed. The slope of the line is the total optical depth (ie. aerosol and molecular).

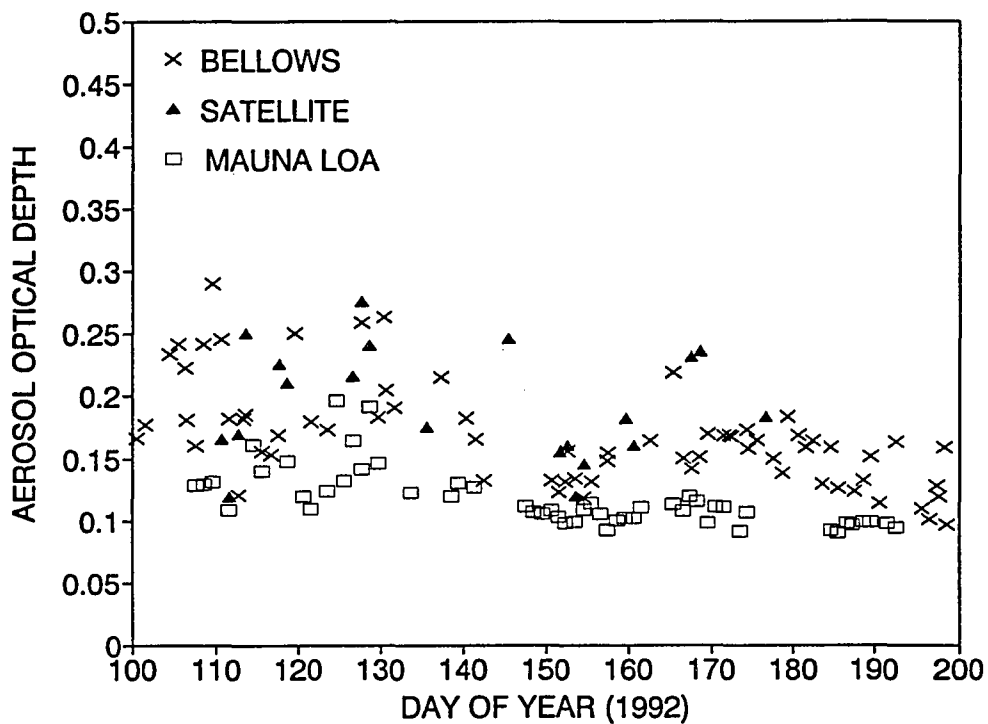


Figure 5.6. Aerosol optical depths derived from: 1) sun photometer measurements at a surface site on the island of Oahu (Bellows beach), 2) sun photometer measurements taken at NOAA Mauna Loa observatory on the island of Hawaii and 3) satellite derived aerosol optical depths. The surface optical depths were obtained by the Langley plot method for daytime am and pm measurements from a shadowband radiometer (550 nm). The satellite optical depths were taken from cloud free pixels found in a 200 by 200 km box around the island of Oahu (630 nm). The Mauna Loa optical depths were provided by Dutton Elsworth and were taken with a sun tracking sun photometer (500 nm).

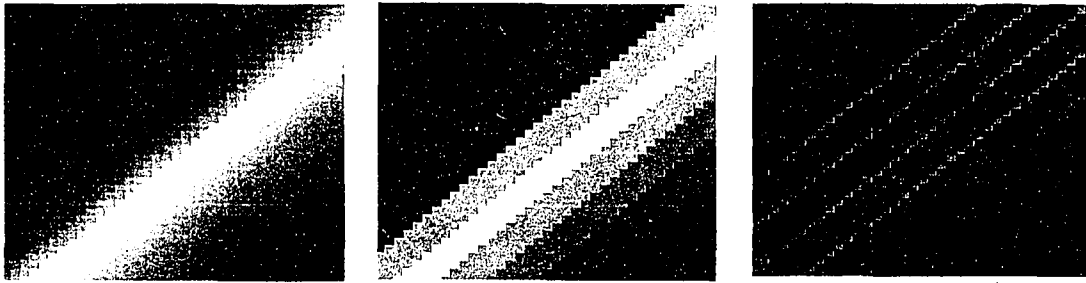


Figure 6.1a. An example to show how subtracting high resolution data (left panel) from coarse resolution data (middle panel) can produce striped results (right panel).

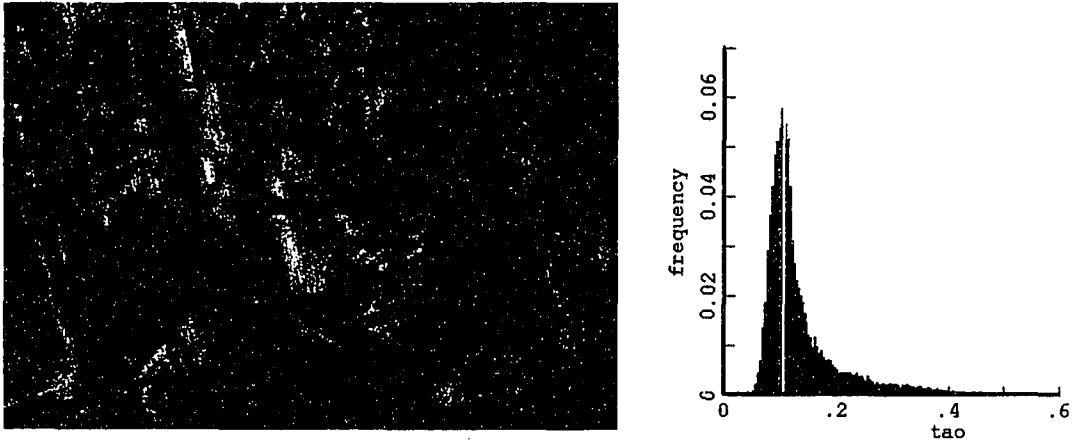


Figure 6.1b. This is the same image of aerosol optical depth as figure 5.6 except a different color enhancement has been used. The striped feature shown in figure 6.1a is evident here.

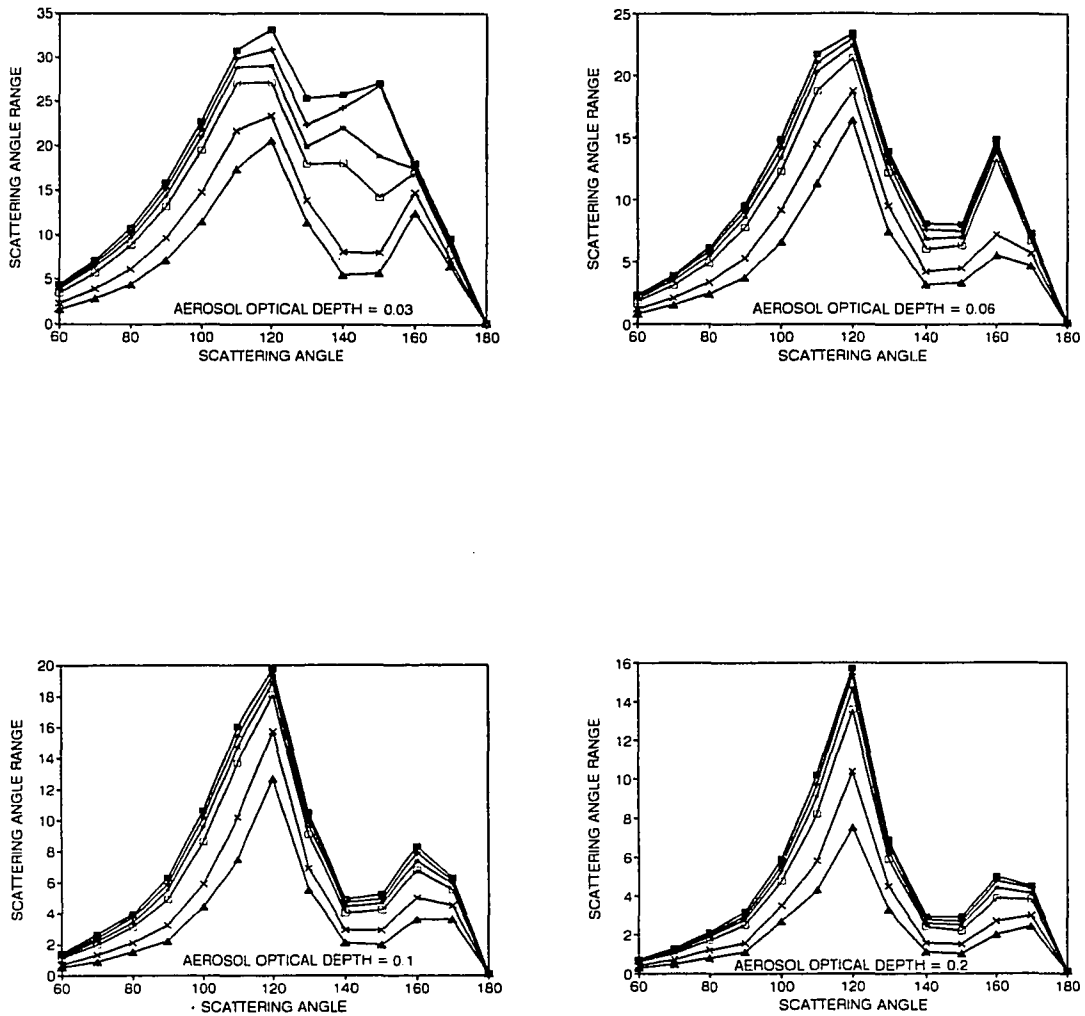


Figure 6.2. The range of scattering angles over which the satellite image must be averaged is shown here for each scattering angle. Averaging the satellite radiance over this range of scattering angles serves to smooth out the digitized nature of the AVHRR image and avoid stripes in the derived aerosol optical depth. Going from left to right and top to bottom each panel corresponds to optical depths of 0.03, 0.06, 0.1 and 0.2. Going from the top curve to the bottom curve, each curve corresponds to the cosine of the satellite zenith angle with values of 1, 0.94, 0.87, 0.77, 0.5 and 0.34.

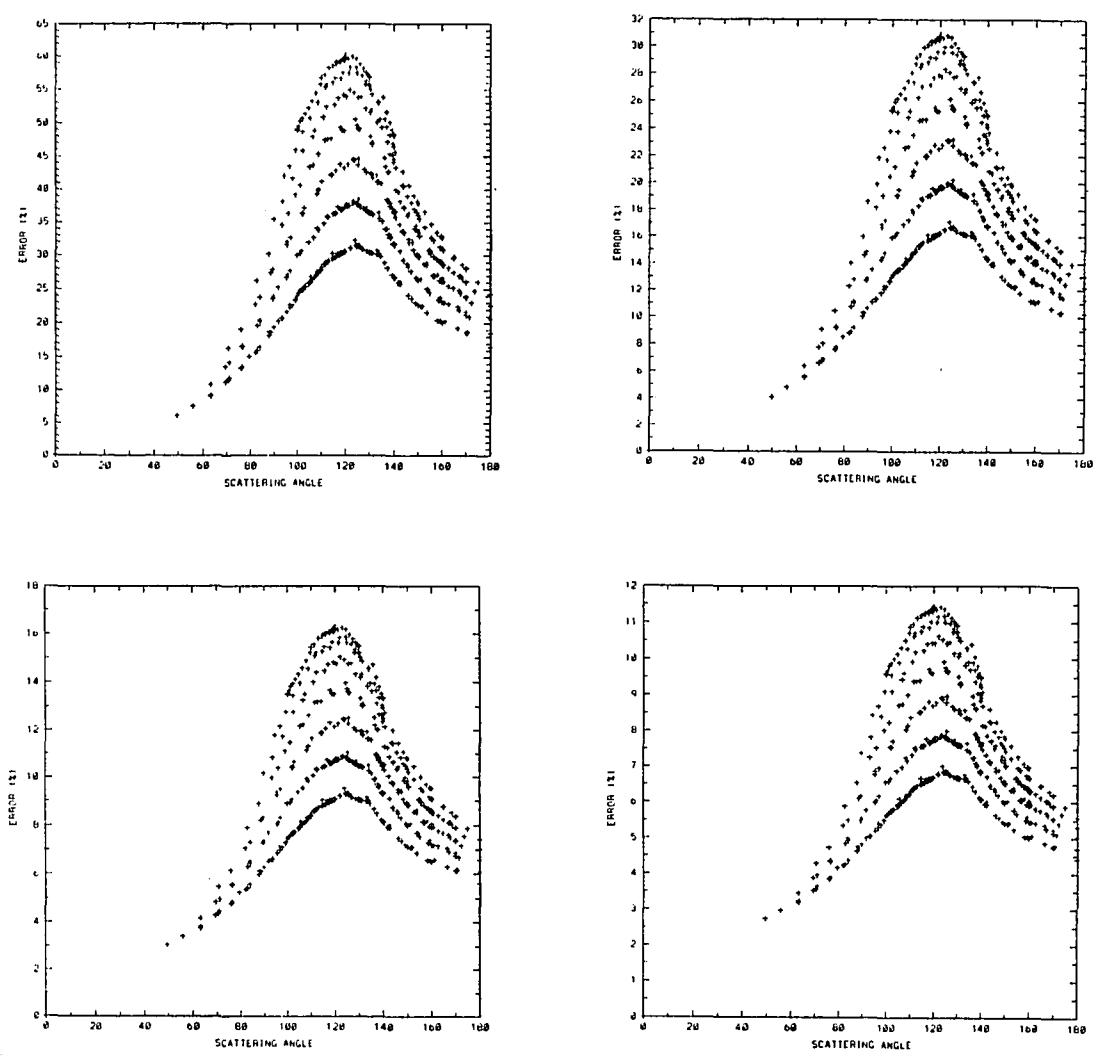


Figure 6.3. Percentage error for AVHRR channel 1 plotted as a function of the aerosol scattering angle. For this figure one standard deviation errors were used for the sensor drift, sensor noise, ozone error, water vapor error, Rayleigh error and sunglint error. Going from left to right and top to bottom, each panel correspond to aerosol optical depths of 0.05, 0.1, 0.2 and 0.3.

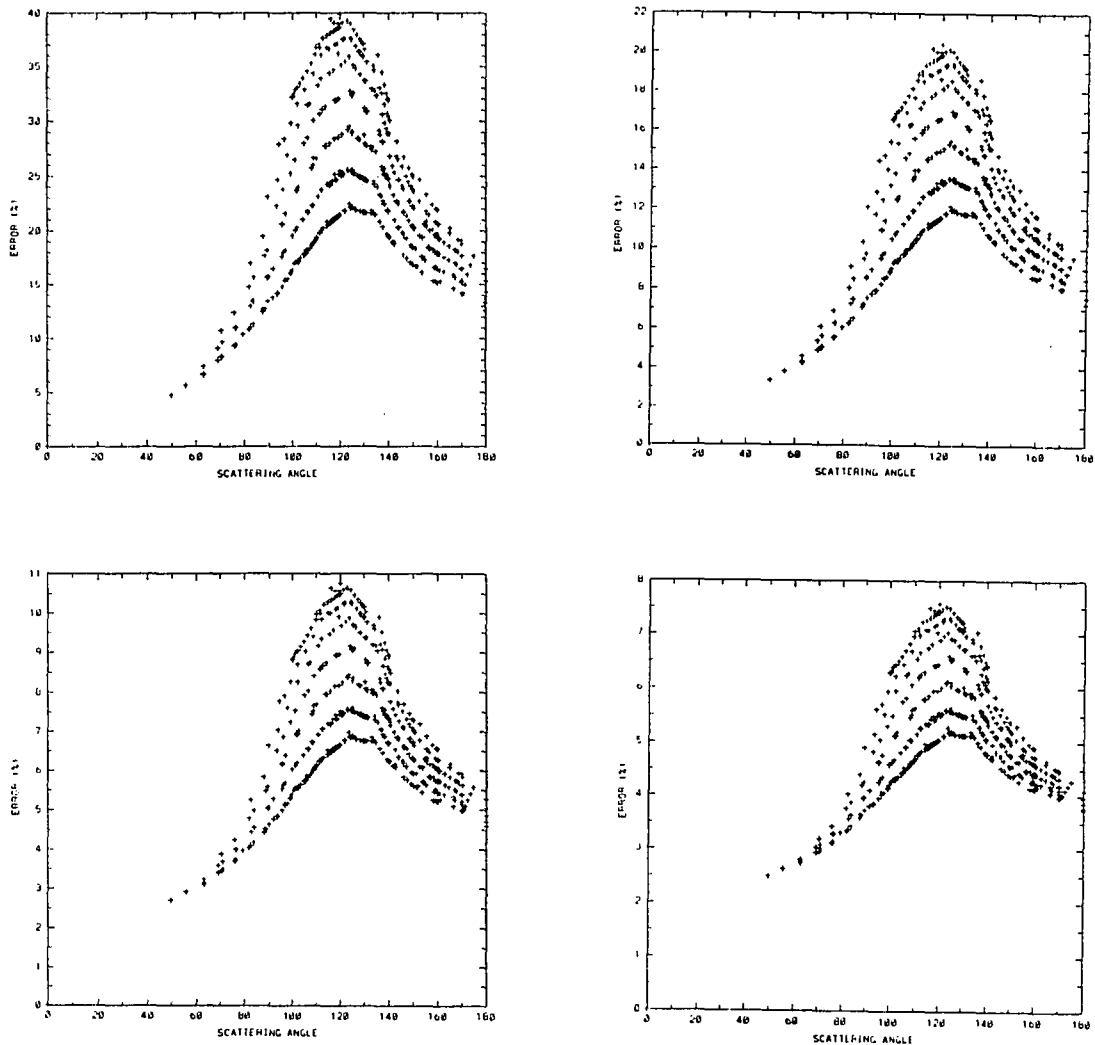


Figure 6.4. Percentage error for AVHRR channel 1 plotted as a function of the aerosol scattering angle. For this figure the sensor noise error was set to zero and one standard deviation errors were used for the sensor drift, ozone error, water vapor error, Rayleigh error and sunglint error. Going from left to right and top to bottom, each panel correspond to aerosol optical depths of 0.05, 0.1, 0.2 and 0.3.

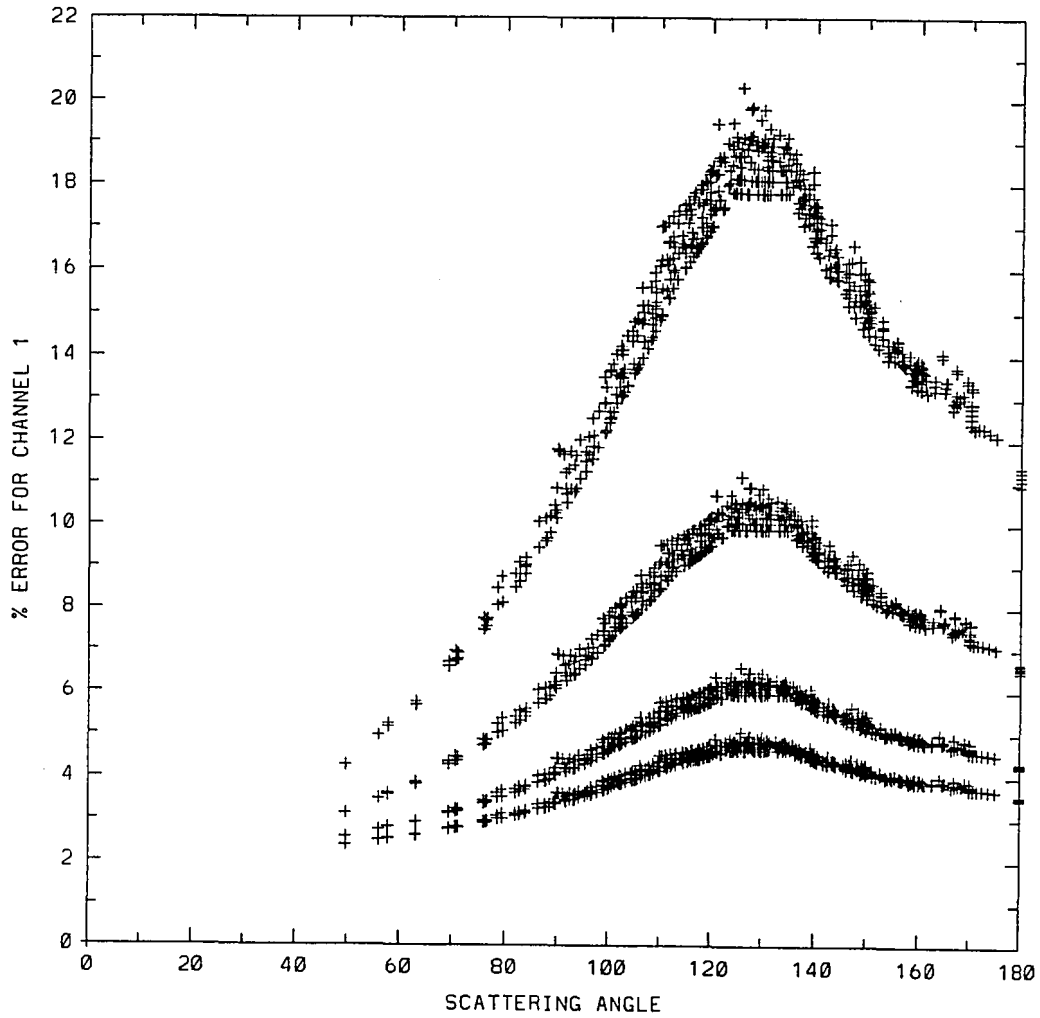


Figure 6.5. Percentage error for AVHRR channel 1 plotted as a function of the aerosol scattering angle. For this figure all errors were set to zero with the exception of the sensor drift error which was set to one standard deviation value. The top through bottom curves correspond to aerosol optical depths of 0.05, 0.1, 0.2 and 0.3.

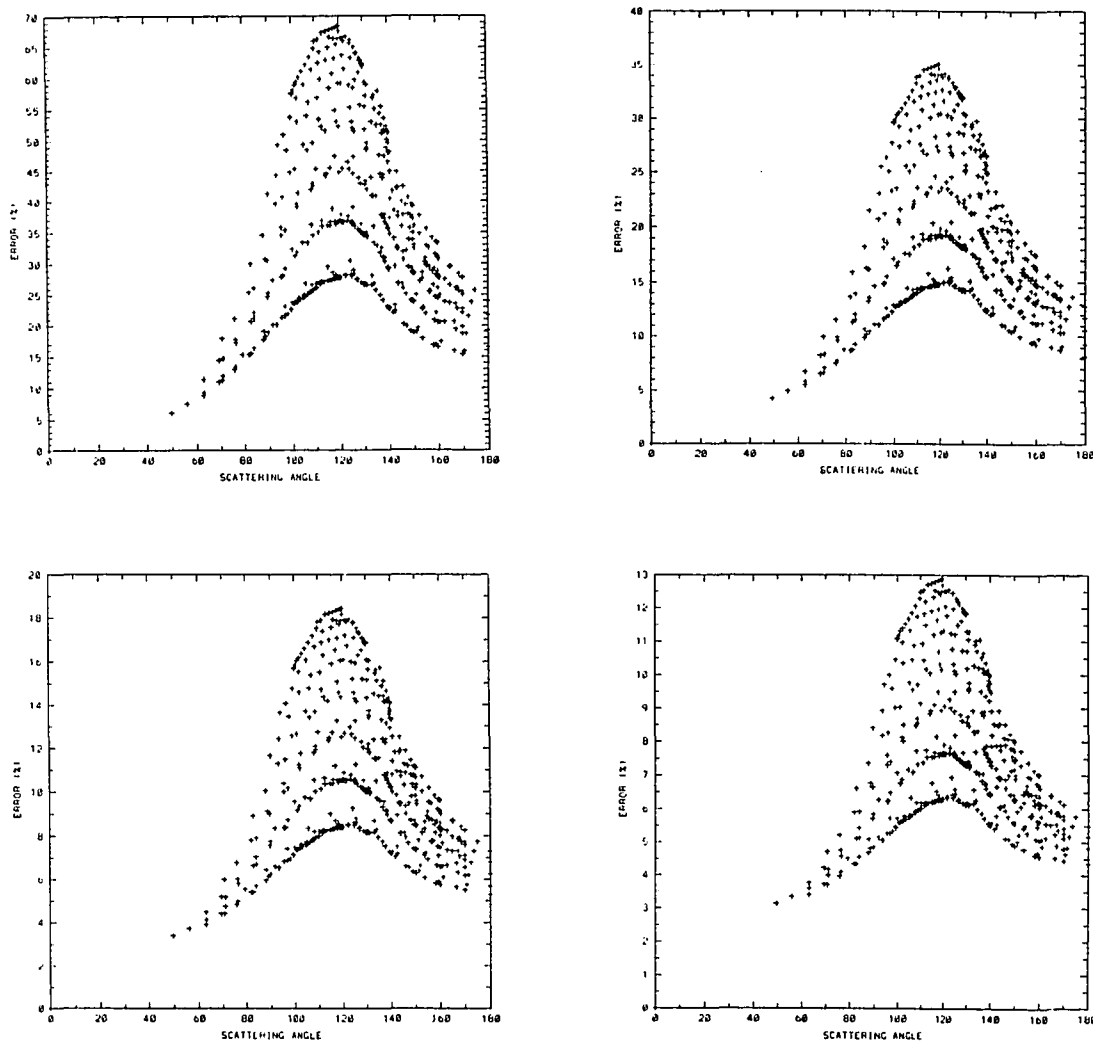


Figure 6.6. Percentage error for AVHRR channel 2 plotted as a function of the aerosol scattering angle. For this figure one standard deviation errors were used for the sensor drift, sensor noise, ozone error, water vapor error, Rayleigh error and sunglint error. Going from left to right and top to bottom, each panel correspond to aerosol optical depths of 0.05, 0.1, 0.2 and 0.3.

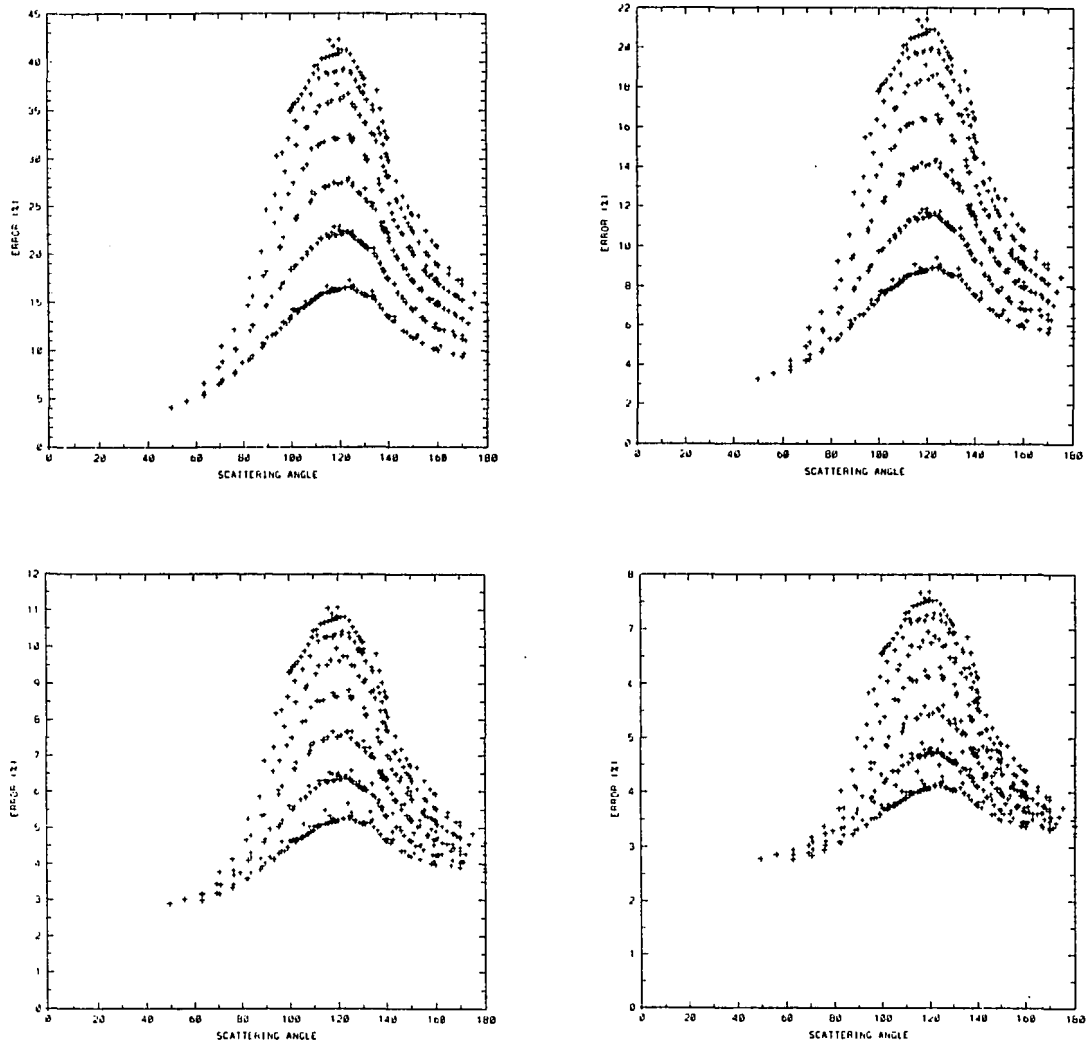


Figure 6.7. Percentage error for AVHRR channel 2 plotted as a function of the aerosol scattering angle. For this figure the sensor noise error was set to zero and one standard deviation errors were used for the sensor drift, ozone error, water vapor error, Rayleigh error and sunglint error. Going from left to right and top to bottom, each panel correspond to aerosol optical depths of 0.05, 0.1, 0.2 and 0.3.

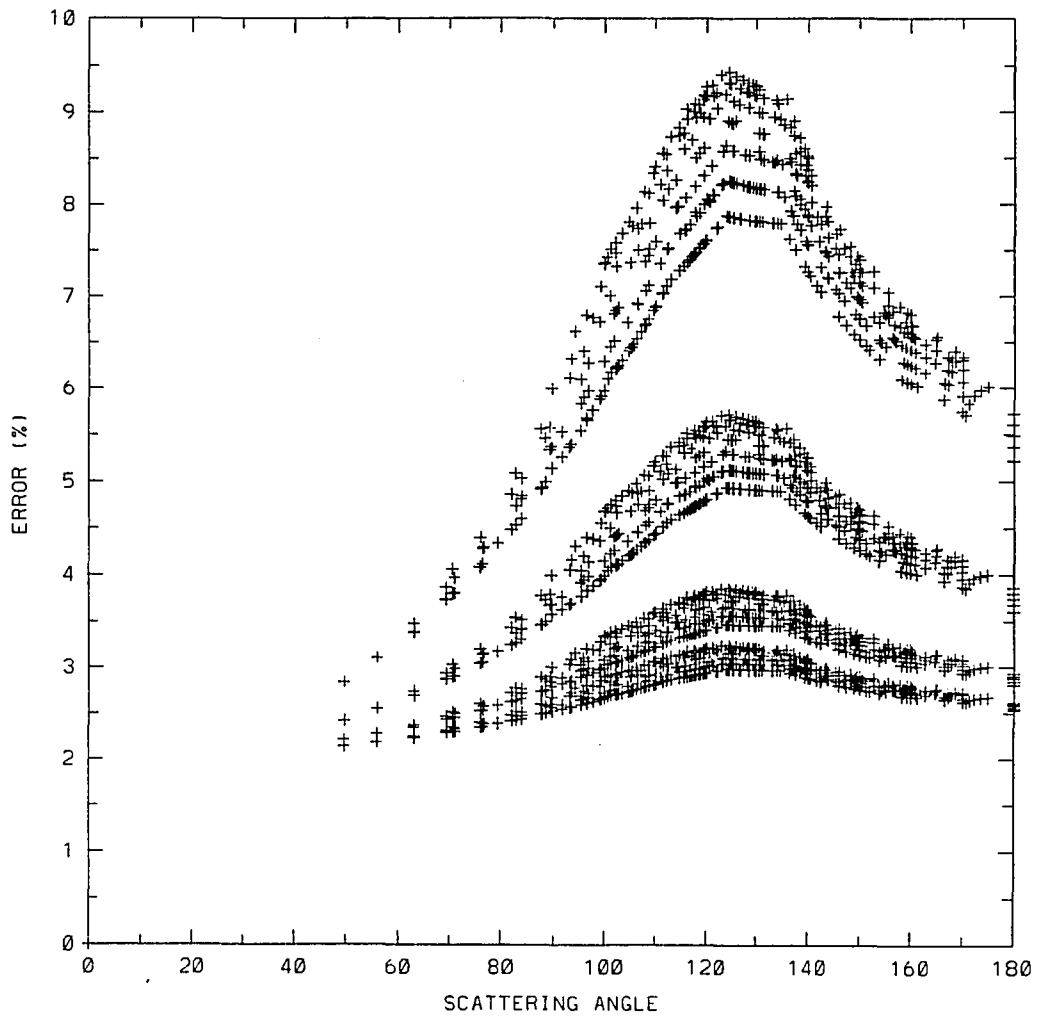


Figure 6.8. Percentage error for AVHRR channel 2 plotted as a function of the aerosol scattering angle. For this figure all errors were set to zero with the exception of the sensor drift error which was set to one standard deviation value. The top through bottom curves correspond to aerosol optical depths of 0.05, 0.1, 0.2 and 0.3.

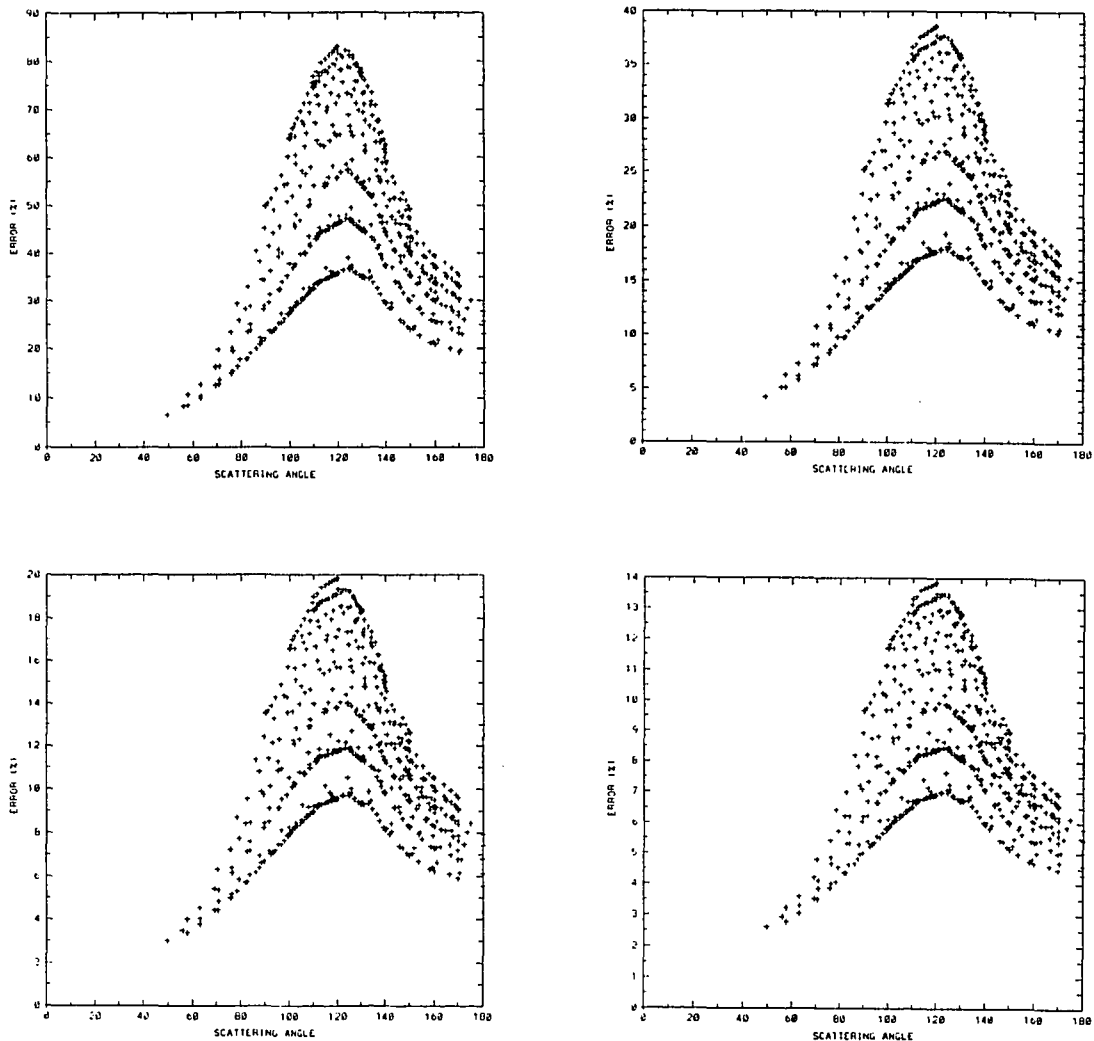


Figure 6.9. Percentage error for AVHRR channel ch1/ch2 ratio plotted as a function of the aerosol scattering angle. For this figure one standard deviation errors were used for the sensor drift, sensor noise, ozone error, water vapor error, Rayleigh error and sunglint error. Going from left to right and top to bottom, each panel correspond to aerosol optical depths of 0.05, 0.1, 0.2 and 0.3.

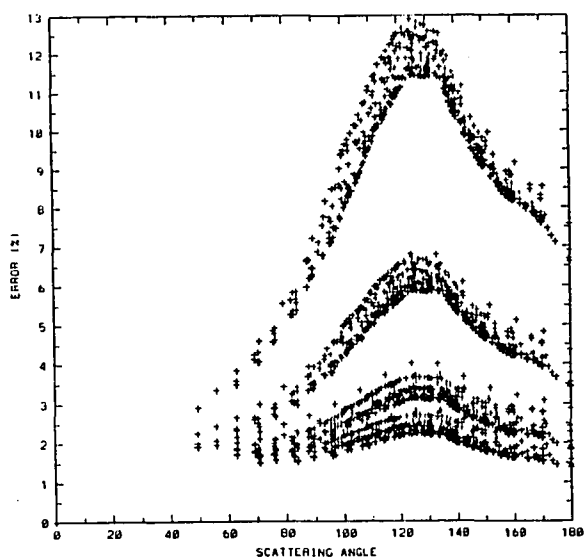


Figure 6.10. Percentage error for AVHRR channel ch1/ch2 ratio plotted as a function of the aerosol scattering angle. For this figure the sensor noise error was set to zero and one standard deviation errors were used for the sensor drift, ozone error, water vapor error, Rayleigh error and sunglint error. The top through bottom curves correspond to aerosol optical depths of 0.05, 0.1, 0.2 and 0.3.

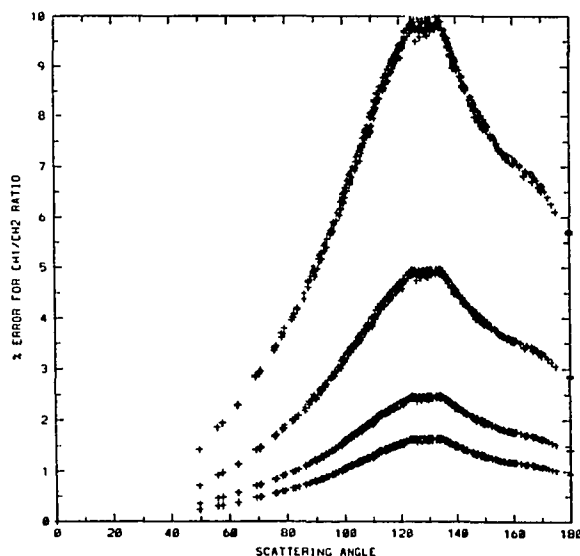


Figure 6.11. Percentage error for AVHRR channel ch1/ch2 ratio plotted as a function of the aerosol scattering angle. For this figure all errors were set to zero with the exception of the sensor drift error which was set to one standard deviation value. The top through bottom curves correspond to aerosol optical depths of 0.05, 0.1, 0.2 and 0.3.

REFERENCES

- Albrecht, B. A., 1989: Aerosol, cloud microphysics and fractional cloudiness. Science, 245, 1227-1230.
- Andre, J. M., Morel, A., 1989: Simulated effects of barometric pressure and ozone content upon the estimate of marine phytoplankton from space. J. Geophys. Res., 94, 1029-1037.
- Bevington, P. R., 1969: Data reduction and error analysis for the physical sciences, McGraw-Hill Book Company.
- Bohren, C. F. and Huffman, D. R., 1983: Absorption and scattering of light by small particles., Wiley -Interscience publication.
- Charlson, R. J., Langener, J., Rhode, H., Leovy, C. B. and Warren, S. G., 1991: Perturbations of the northern hemisphere radiation balance by backscattering from anthropogenic sulfate aerosol., Tellus, 43AB, 152-163.
- Charlson, R. J., Lovelock, J. E., Andreae, M. O. and Warren, S. G., 1987: Oceanic phytoplankton, atmospheric sulphur, cloud Albedo, and climate. Nature, 326, 655-661.
- Clarke, A. D., 1990: A thermo-optic technique for insitu analysis of size resolved aerosol physicochemistry, Atmos. Environ., 25A, 635-644.
- Clarke A. D., 1989: Aerosol light absorption by soot in the remote environments. Aerosol Science and Tech., 110, 161-171.

- Clarke, A. D. and Porter, J. N., 1991a: Aerosol size distributions, composition, and CO₂ backscatter., J. Geophys. Res. 96, 5237-5247.
- Clarke, A. D. and Porter, J. N., 1991b: Volcanic haze-physicochemistry and transport. Vog and Laze Conference, Hilo, Hawaii.
- Cox, C, Munk, W., 1955: Some Problems In Optical Oceanography., J. Mar. Res., 14, 63-78.
- D'Almeida, G. A., Koepke, P., Shettle, E. P., 1991: Atmospheric aerosols: global climatology and radiative characteristics., Deepak Publishing, Hampton, Virginia.
- Dalu, G., 1986: Satellite remote sensing of atmospheric water vapor., Int. J. Remote Sensing, 7, 1089-1097.
- Diermendjian, D., 1969: Electromagnetic scattering on spherical polydispersions., American Elsevier Publishing Company.
- Durkee, P. A., Pfeil, F., Frost, E., Shema, R., 1991: Global analysis of aerosol particle characteristics. Atmos. Environ., 25A, 2457-2471.
- Garthman, S. G., 1984: Navy hygroscopic aerosol model. Hygroscopic Aerosol, Deepak, Hampton, Va.
- Garthman, S. G. 1982: A time dependent oceanic aerosol model. Naval Research Laboratory Tech. Rept. 8536, Washington DC, pp35.

- Griggs, M., 1975: Measurements of atmospheric aerosol optical thickness over water using ERTS-1 Data. Journal of the Air pollution Control Assoc., 25, 622-626.
- Griggs, M., 1983: Satellite measurements of tropospheric aerosols. Adv. Space Res., 2, 5, Pergamon Press, New York, NY, 109-118.
- Griggs, M., 1986: Satellite measurements of aerosols over ocean surfaces. Ocean Whitecaps, D. Reidel Publishing Co., 245.
- Gordon H. R. and Morel, A. Y., 1980: Phytoplankton pigments derived from the Nimbus-7 CZCS; Initial comparisons with surface measurements. Science, 210, 63-75.
- Hansen, J. E. and Lacis, A. A., 1990: Sun and dust versus greenhouse gasses: An assessment of their relative roles in global climate change. Nature, 346, 713-719.
- Holben, B. N., Kaufman, Y. J., 1990: NOAA 11 AVHRR visible and near-IR inflight calibration., Int. J. Remote Sensing, 11, 1151-1159.
- Iqbal, M., 1983: An introduction to solar radiation. Academic Press.
- Irvine, W. M., Pollack, J. B., 1968: Infrared optical properties of water and ice spheres. ICARUS, 8, 324-360.
- Kasten, F., 1965: A new table and approximation formula for the relative optical air mass. Arch. Meteorol. Geophys. Bioklimatol., B14, 206-233.

- Kennish, M. J., 1989: Practical handbook of marine science. CRC Press. Inc., Boca Raton, Florida, pp. 96.
- Kidwell, K. B., 1991: NOAA polar orbiter data users guide (TIROS-N, NOAA-6, NOAA-7, NOAA-8, NOAA-9, NOAA-10, NOAA-11, NOAA-12). National Oceanic and Atmospheric Administration National Environmental Satellite, Data, and Information Service, National Climate Data Center, Satellite Data Services Division.
- Koepke, P., 1985: The reflectance factors of a rough ocean with foam - comment on 'Remote sensing the sea state using 0.8-1.1 μm spectral band' by L. Wald and J. M. Monget. Int. J. Remote Sensing, 6, 787-799.
- Liou, K. N. 1980: An introduction to atmospheric radiation. Academic Press.
- Michalsky, J. J., 1988: The astronomical almanac's algorithm for approximate solar position (1950-2050). Solar Energy, 40, 227-235.
- Mitchell, R. M., O'Brien, D. M., 1992: Calibrations of the NOAA AVHRR shortwave channels using split pass imagery: I. pilot study. Remote Sens. Environ., 40, 57-65.
- Nakajima, T., Tanaka, M., 1983: Effect of wind-generated waves on the transfer of solar radiation in the atmosphere-ocean system. J. Quant. Spectrosc. Radiant. Transfer, 29, 521-537.

- Nakajima, T. and Tanaka, M. 1988: Algorithms for radiative intensity calculations in moderately thick atmospheres using a truncation approximation. J. Quant. Spectros. Radiant. Transfer, 40, 51-69.
- Okasaki, K, and Willeke, K., 1987: Transmission and deposition behavior of aerosols in sampling inlets. Aerosol Science and Technol., 7, 275-283.
- O'Muircheartaigh, I. G., Monahan, E. C., 1986: Statistical aspects of the relationship between oceanic whitecap coverage wind speed and other environmental factors., Oceanic Whitecaps, D. Riedel Publishing Co., 125.
- Piu, D. H., Novas, F. R. and Liu, B. Y. H., 1987: Experimental study of particle deposition in bends of circular cross section. Aerosol Science and Technol., 7, 301-315.
- Palmer, K. F., Williams, D., 1975: Optical constants of sulfuric acid: Application to the clouds of Venus?, Applied Optics, 14, 208-219.
- Porter, J. N., 1988: Marine aerosol: Their measurement and influence on cloud base properties. Masters Thesis, University of Hawaii.
- Porter, J. N., Clarke, A. D., Ferry, G. and Pueschel, R. F., 1992: Aircraft studies of size dependent aerosol sampling through inlets. J. Geophys. Res., 97, 3815-3824.

- Ramanathan, V. Cess, R. D., Harrison, E. F., Minnis, P.,
Barkstrom, B. R., Ahmad, E. and Hartman, D., 1989a:
Cloud radiative forcing and climate; Results from the
earth radiation budget experiment. Science, 243, 1-14.
- Ramanathan, V., Barkstrom, B. R. and Harrison, E. F., 1989b:
Climate and the earth's radiation budget. Phys. Today,
42(5), 22-32.
- Ramsey, R. C., 1968: Study of the remote measurement of ocean
color. Final Report, TRW, NASW-1658.
- Rao C. R., Stowe, L. L., McClain, E. P., 1989: Remote sensing
of aerosols over the oceans using AVHRR data: theory,
practice, applications. Int. J. Remote Sensing, 10,
743-749.
- Sanders, R. W., Edwards, D. P., 1989: Atmospheric
Transmittances for the AVHRR channels. Applied Optics,
28, 4154-4160.
- Shettle, E. P., and R. W. Fenn, 1979: Models for the aerosols
of the lower atmosphere and the effects of humidity
variations on their optical properties. Rep. AFGL TR-79
-0214, AD-A085951, 94 pp., Air Force Geophys. Lab.,
Bedford, Mass., (Available as AD-A197945 from Natl.
Tech. Inf. Serv., Springfield, Va.)
- Stowe, L. L., Carey, R. M. and Pellegrino, P. P., 1992:
Monitoring the Mt. Pinitubo aerosol layer with NOAA/11
AVHRR DATA. Geophys. Res. Letters, 19, 159-162.

- Tang, I. N., Munkelwitz, H. R., J. G. Davis, 1977A: Aerosol growth studies II, preparation and growth measurements of monodisperse salt aerosols. J. Aerosol Sci., 8, 149-159.
- Tang, I. N., Munkelwitz, H. R., 1977B: Aerosol growth studies, III, ammonium bisulfate aerosols in a moist atmosphere, J. Aerosol Sci., 8, 321-330.
- Tang, I. N., 1980: Deliquescence properties and particle size change of hygroscopic aerosols. Generation of Aerosol, Ann Arbor Science Publishers, 153 pp.
- Takahashi, T., 1976: Warm rain, giant nuclei and chemical balance-a numerical study. J. Geophys. Res., 33, 269-286.
- Tiellet, P., M. 1990: Rayleigh optical depth comparisons from various sources. Applied Optics, 29, 1897-1900.
- Tiellet, P. M. and Holben, B. N., 1993: Towards operational radiometric calibration of NOAA AVHRR imagery in the visible and infrared channels. submitted to the Canadian J. of Remote Sensing.
- Twomey, S., 1977: Atmospheric Aerosol, Elsevier Press.
- Van Heuklon, 1979: Estimating atmospheric ozone for solar radiation models, Solar Energy, 22, 63-68.
- Wald, L., Monget, J. M., 1983: Remote sensing of the sea state using the 0.8-1.1 μm spectral band. Int. J. Remote Sensing, 4, 433-446.

Woodcock, A. H., 1953: Salt nuclei in marine air as a function of altitude and wind force. J. of Meteorology, 10, 362-371.